Optimal Energy Management for Battery Energy Storage System-Integrated Microgrids

by
Cunzhi Zhao

A report submitted to the Department of Electrical and Computer Engineering,
Cullen College of Engineering
in partial fulfillment of the requirements for the degree of

Doctor of Philosophy

in Electrical and Computer Engineering

Chair of Committee: Dr. Xingpeng Li

Committee Member: Dr. Kaushik Rajashekara

Committee Member: Dr. Hao Huang

Committee Member: Dr. Zhu Han

Committee Member: Dr. David R. Jackson

University of Houston

December 2023

ACKNOWLEDGMENTS

I would like to express my deepest gratitude and appreciation to Dr. Xingpeng Li who have supported me throughout my Ph.D. studies in the Renewable Power Grid lab and Power Electronics, Microgrids & Subsea Electrical Systems Center at the University of Houston. His expertise, patience, and encouragement have been the cornerstone of this research.

I am also deeply grateful to the members of my dissertation committee, Prof. Kaushik Rajasekhara, Prof. Hao Huang, Prof. Zhu Han, together with Prof. David R. Jackson, for their valuable feedback, constructive criticism, and the time they dedicated to reviewing and valuable insights to improve this dissertation.

I would also like to thank already graduated students, Dr. Arun Venkatesh Ramesh, and Dr. Mingjian Tuo, together with current students Jin Lu, Thuan Pham, Jesus Silva-Rodriguez, who provided me with a strong network of academic and emotional support. Your insights, discussions, and camaraderie have enriched my academic experience.

I would like to thank my parents, Shuwen Zhao and Limei Chen, my partner Alice and my daughter Zoe, for all their love, support, and patience in the last four years of my academic life. They are the people who always encourage me to pursue academic excellence.

ABSTRACT

This dissertation explores optimal energy management strategies for battery energy storage system (BESS)-integrated microgrids, addressing both grid-connected and isolated microgrid scenarios. The research is motivated by the increasing integration of renewable energy sources, such as wind and solar, which introduce uncertainty and challenges in maintaining grid stability. As a result, an increasing number of BESS are being incorporated into the system to facilitate the seamless integration of renewable energy sources. However, degradation remains an inevitable challenge, posing difficulties in accurately modeling and predicting the condition of key BESS components, especially the widely used Lithium-ion batteries.

To address this issue, a data driven method to predict the battery degradation per a given scheduled battery operational profile is investigated. Particularly, a neural network based battery degradation (NNBD) model is proposed to quantify the battery degradation with inputs of major battery degradation factors. When incorporating the proposed NNBD model into microgrid day-ahead scheduling (MDS), it creates the proposed battery degradation based MDS (BDMDS) model that can consider the equivalent battery degradation cost precisely. Since the proposed NNBD model is highly non-linear and non-convex due to the rectified linear unit (ReLU), BDMDS would be very hard to solve. To address this issue, a neural network and optimization decoupled heuristic algorithm is proposed here to effectively solve this neural network embedded optimization problem.

An alternative way to solve the BDMDS model is to linearize the NNBD model by converting the nonlinear activation function at each neuron into linear constraints, which enables BDMDS to become a linearized BDMDS model. In addition, ReLU linearization approximation methods and sparse computation models are implemented to further improve the algorithm efficiency while retaining solution quality.

TABLE OF CONTENTS

LIST OF TABLES

LIST OF FIGURES

NOMENCLATURE

Sets and indices:

S_G	Set of controllable generators.
S_T	Set of time intervals.
S_S	Set of energy storage systems.
S_{WT}	Set of wind turbines.
S_{PV}	Set of PV systems.
$K^+(n)$	Set of lines with bus *n* as receiving bus.
$K^-(n)$	Set of lines with bus *n* as sending bus.
K	Set of lines.
Ω	Set of Scenarios.
I	Set of Inverters.
T	Set of time periods.
N	Set of buses.
ω	Scenario index ω.
g	Generator g.
k	Line k.
t	Time t.
n	Bus n.
s	Battery energy storage system s.

Parameters:

c_g	Linear operation cost for generator g.
c_g^{NL}	No load cost for generator g.
c_g^{SU}	Start-up cost for generator for generator g.
ΔT	Length of a single dispatch interval.
P_g^{min}	Minimum output limit of generator g.
P_g^{max}	Maximum output limit of generator g.
P_s^{min}	Minimum charge/discharge power of BESS *s*.
P_s^{max}	Maximum charge/discharge power of BESS *s*.
P_k^{max}	Long-term thermal line limit for line k.
b_k	Susceptance of line k.
P_L^t	Load demand at time period t.
$E_s^{Initial}$	Initial energy capacity of BESS *s*.
E_s^{Max}	Maximum energy capacity of BESS *s*.
E_s^{Min}	Minimum energy capacity of BESS *s*.
c_t^{Buy}	Wholesale electricity purchase price in time interval *t*.
c_t^{Sell}	Wholesale electricity sell price in time interval *t*.
η_s^{Disc}	Discharge efficiency of BESS *s*.
η_s^{Char}	Charge efficiency of BESS *s*.
R_{Prcnt}	Ratio of the backup power to the total power.
ρ_ω	Probability of scenario ω.

$P_{i,t}^{I}$ Power output from inverter *i* (solar/wind power).

$f_{i,t,\omega}^{I}$ Failure indicator for inverter *i*.

$P_{crit,t}^{L}$ Critical power load.

c_h Penalty term for approximation methods.

W Weights matrix of W.

x_{h}^{i} Pre-activated value of neuron i at hidden layer h

UB Upper bound of pre-activated value.

LB Lower bound of pre-activated value.

Variables:

P_g^t Output of generator *g* in period t.

U_g^t Commitment status of generator in time period *t.*

V_g^t Start-up variable of generator in time period *t.*

P_k^t Flow on line *k* in time period *t*.

P_{Buy}^t Amount of power purchased from main grid power in time interval t.

P_{Sell}^t Amount of power sell to main grid power in time interval t.

$U_{Disc}^{t,i}$ Status of buying power from main grid in time interval *t*.

$U_{Char}^{t,s}$ Charging status of energy storage system *s* in time interval t. It is 1 if charging status; otherwise 0.

$U_{Disc}^{t,s}$ Discharging status of energy storage system *s* in time interval t. It is 1 if discharging status; otherwise 0.

$P_{Char}^{t,s}$ Charging power of energy storage system *s* at time *t*.

$P_{Disc}^{t,s}$ Discharging power of energy storage system *s* at time *t*.

U_{Buy}^{t} Status of buying power from main grid in time interval *t*.

U_{Sell}^{t} Start-up variable of generator g in period t.

$\theta_{n(k)}^{t}$ Phase angle of bus n in period t.

$\theta_{m(k)}^{t}$ Phase angle of bus m in period t.

$v_{i,t,\omega}^{I}$ On/off status indicator for inverter *i*.

$u_{i,t,\omega}^{I}$ Availability indicator for inverter *i*.

$X_{t,\omega}^{T}$ Successful indicator of time interval *t* of scenario ω.

X_{ω} Successful indicator of scenario ω.

$Y_{t,\omega}$ Surplus variable.

$P_{t,\omega}^{NET}$ Aggregated power of scenario ω at time interval *t*.

$w_{i,t,\omega}^{I}$ Confirmed inverter failure indicator for inverter *i*.

a_{h}^{i} Activated value of neuron i at hidden layer h.

δ_{h}^{i} Activation status of neuron i at hidden layer h.

1. INTRODUCTION

1.1 Background

The rise in greenhouse gas emissions is the driving force behind global warming, which has unleashed a cascade of natural disasters that could have been averted. Notably, the power system plays a significant role in this predicament, contributing a substantial share of carbon emissions each year [1]. As we set our sights on a cleaner, more sustainable future, it's essential to reexamine the traditional power system, composed of three main components: generation, transmission, and distribution. The generation phase, reliant on coal, natural gas, and fossil fuels, is where the majority of carbon emissions stem from, as these sources are burned to create the steam that drives turbines, generating power and releasing copious amounts of emissions into the atmosphere.

To address this environmental challenge and reduce carbon emissions, renewable energy sources (RES) have emerged as a transformative force in the power system. Their eco-friendly nature stands in contrast to conventional fossil fuels, providing clean, sustainable, and unlimited electricity. RES plays a pivotal role in curbing greenhouse gas emissions and combating climate change. The primary installation of renewable energy sources (RES) in the contemporary energy landscape predominantly revolves around wind and solar power. Wind energy harnesses the kinetic energy of moving air through the deployment of wind turbines, while solar power captures the sun's radiant energy through photovoltaic cells. These two sources

have become cornerstones of the global effort to transition towards cleaner, more sustainable energy solutions. Their widespread adoption is driven by their remarkable environmental benefits, including a substantial reduction in greenhouse gas emissions and a diminished reliance on fossil fuels. Moreover, wind and solar power hold immense potential in decentralizing energy generation and fostering energy independence. As the world strives to combat climate change and create a greener energy future, wind and solar power play pivotal roles in redefining the energy landscape. In this context, it becomes essential to explore innovative strategies for maximizing the utilization and integration of these renewable resources, aiming to create a more sustainable and resilient energy infrastructure.

However, the increasing use of RES for power generation has introduced challenges related to system stability due to the unpredictable and intermittent nature of these energy sources. In response to this challenge, battery energy storage systems (BESS) are being widely adopted as a practical and effective solution, ensuring a more reliable and sustainable power system for the future. Moreover, the existing centralized power system's reliance on long transmission lines results in significant energy loss due to heat dissipation. A potential solution to this inefficiency lies in decentralizing the power system through the implementation of microgrids. Microgrids represent localized energy assets that independently meet the energy needs of their communities by generating power from local sources.

To meet the clean and sustainable power system, the integration of RES and BESS within microgrids is becoming more important. Microgrids, often operating as

self-contained localized energy networks, must adapt to the challenges of incorporating RES and BESS to enhance their reliability, sustainability, and energy independence [2]. Achieving this goal necessitates an advanced approach of microgrid energy management [3]. This integrated energy management system is the key that enables microgrids to efficiently harness the potential of RES and BESS, optimizing power generation and distribution while ensuring a stable and resilient energy supply. The advanced microgrid energy management, is pivotal in the transition to cleaner, more sustainable energy solutions while ensuring grid reliability and adaptability to meet the evolving energy trends of the future.

1.2 Motivations

In line with the global trend towards decarbonization policies, the power system is undergoing a transformative shift from traditional power systems to modern, sustainable alternatives [4]. The United States government has committed to achieving net-zero carbon emissions by 2050 [5], catalyzing a substantial reduction in the presence of high carbon-emission, traditional power plants within the energy landscape. Simultaneously, renewable energy generation is poised for significant growth as it aligns with this ambitious goal.

In the meanwhile, the electrification of the transportation industry is driving a substantial increase in electricity demand. Projections indicate that electricity demand is expected to keep increasing. This surge poses a significant challenge, as the power system must undergo a dual transformation: transitioning to cleaner energy sources while also accommodating this growing demand. In response to this challenge,

decentralized power systems, characterized by the proliferation of microgrids, are emerging as a solution. Microgrids represent local energy assets capable of autonomously fulfilling the energy demands of their respective communities through locally generated power sources [6]. Microgrids come in two main forms: isolated microgrids and grid-connected microgrids. Isolated microgrids, as the name suggests, are self-contained and not connected to the main grid. They are typically deployed in isolated regions, such as islands or military bases. On the other hand, grid-connected microgrids are interconnected with the main grid through tie-lines, facilitating electricity exchange that enhances grid reliability and resilience. They play a pivotal role in the realization of a cleaner and more resilient energy future.

A typical microgrid comprises key components, including the load sector, distributed energy sources, renewable energy resources (RES), and energy storage systems. Distributed energy sources encompass a variety of options, such as diesel generators, while RES encompass wind, solar, geothermal, hydro, and more. Among these, wind farms and solar farms are the most common. However, the inherent stochastic and intermittent nature of renewable energy, particularly wind and solar power, introduces variability not present in traditional generators. To counteract this variability and ensure a stable power supply, energy storage systems (ESS) play a critical role.

Battery Energy Storage Systems (BESS) is the most installed ESS throughout the power system industry. In the current market of BESS, lithium-ion batteries have emerged as the primary and widely adopted choice [7]. Yet, these batteries, while

offering impressive performance characteristics, are not immune to the inexorable process of degradation over cycles of use, a phenomenon that can significantly impact their efficiency and overall functionality. The degradation of lithium-ion batteries stems from the depletion of Li-ions and electrolyte, coupled with the rise in internal resistance [8]. These cumulative effects result in reduced energy capacity during daily cycling. Thus, accurately quantifying battery degradation is an urging task, particularly when BESS operates in diverse conditions and environments in the power system.

1.3 Summary of contents

The rest of this dissertation is structured as follows. Two microgrid energy management strategies are presented for grid-connected microgrid in Chapter 2. In this chapter, the BESS is integrated to mitigate the fluctuation caused by the renewable energy sources of the microgrid, which enables the microgrid become a grid-friendly microgrid. Then, a seconded strategy is proposed to make microgrid provide flexible grid-microgrid exchange power (trading power) to the grid, which enables the microgrid become a grid-supporting microgrid.

In Chapter 3, the strategies are proposed for the isolated-microgrid. A novel renewable energy sources system is proposed to replace the traditional electricity generation to power the offshore platforms by 100% clean renewable energy with zero CO2 emissions. Three resilience models are designed to enhance the reliability of the proposed OHRES system by imposing extra power capability and energy storage of BESS and/or HESS. Also, this chapter introduces a resilience index, a microgrid

survivability rate (SR) under extreme events, and then proposes a novel Resilient Operational Planning (ROP) algorithm to maximize the proposed resilience index SR.

In Chapter 4, a data driven method is propose to predict the battery degradation per a given scheduled battery operational profile. Particularly, a neural network based battery degradation (NNBD) model is proposed to quantify the battery degradation with inputs of major battery degradation factors. When incorporating the proposed NNBD model into microgrid day-ahead scheduling (MDS), a battery degradation based MDS (BDMDS) model is modeled to consider the equivalent battery degradation cost precisely. Furthermore, a hierarchical deep learning based battery degradation quantification (HDL-BDQ) model is proposed to quantify the battery degradation given scheduled BESS daily operations.

Chapter 5 discusses that BDMDS model may not be solved directly due to high non-linearity of the NNBD model. An iteration method is introduced in Chapter 4, however, it is not a solution for multiple BESS system, especially in the security-constrained unit commitment (SCUC) problem. To address this issue, the NNBD model is linearized by converting the nonlinear activation function at each neuron into linear constraints, which enables BD-SCUC to become a linearized BD-SCUC (L-BD-SCUC) model. Case studies demonstrate the proposed L-BD-SCUC model can be efficiently solved for multiple BESS buses power system day-ahead scheduling problems with the lowest total cost including the equivalent degradation cost and normal operation cost.

Chapter 6 discuss the computation enhancement of the proposed NNBD embedded optimization problem in microgrid day-ahead scheduling. The linearization of rectified linear unit (ReLU) has brought a huge computational burden. Thus, several ReLU linearization method are proposed to reduce the computational complexity and improve the solving efficiency. Also, a sparse neural network structure is proposed to reconstruct the NNBD model to reduce the model's non-linearity.

Finally, Chapter 7 concludes this dissertation and presents potential future work.

2. BESS IN GRID-CONNECTED MICROGRID

2.1 Literature Review

Microgrid is a local asset aggregator that coordinates and manages distributed energy resources (DERs) in an autonomous and decentralized manner. A networked microgrid can operate (i) in a grid-connected mode with the main grid, or (ii) in an isolated mode without the main grid. In the grid-connected mode, microgrid remains connected to the main grid while importing or exporting power from/to the main grid. When there is a disturbance in the main grid that affects microgrid reliability, microgrid can switch to the isolated mode which can supply the power by itself. DERs include energy storage system (ESS) and renewable energy resources (RESs) such as solar photovoltaic (PV) and wind turbines (WT) [9]. Renewable energy resources develop rapidly nowadays. The real-time generation of those variable renewable units depends on weather situations such as solar irradiation and wind speed and can be highly intermittent and stochastic [10]. This leads to uncertainties in addition to the load fluctuation in the microgrid, thereby creating serious challenges for microgrid energy management [11]. With deployment of a large number of networked microgrids with high penetration of distributed RESs, the power grid will encounter unprecedented uncertainty spread over the entire plays a critical role in the stability and operation of power systems.

Microgrid energy management is very important and it has been extensively studied in the literature. A microgrid load management is introduced in [12] to maintain the balance between generation and load; loads are classified based on

whether the loads can be shed or not. However, only the near real-time case has been discussed in [12]. A chance constrained approach is proposed to systematically incorporate the energy management problem with uncertainties caused by RESs in the grid-connected microgrid [13]. Deep recurrent neural network leaning is introduced in [14] to minimize the microgrid cost without using information of long-term forecasting. A rolling horizon strategy that only covers a single interval is proposed here in [15] for RES based microgrid. The cost of microgrid is decreased by updating the optimized set points for DERs. Though [12]−[15] propose several effective microgrid energy management strategies, they only cover a single time interval in their real-time economic dispatch optimization. Single interval dispatch strategies fail to consider the variabilities and uncertainties associated with the very next few intervals which may affect the cost and reliability. In addition, those strategies ignore real-time sub-minute net-load fluctuation and assume the main grid can absorb the fluctuation at no cost. However, this could lead to substantial power grid uncertainty and may negatively affect system reliability significantly.

Microgrid ancillary services provided to the utility grid are discussed in [16], a microgrid model is designed to provide the ancillary service (frequency control, spinning reserve, and non-spinning reserve) to the grid. In [17], a microgrid model is built to provide optimal scheduling to flatten the duck curve. Other technologies such as battery energy storage system (BESS) plays an importance role to mitigate the net-load fluctuation in microgrid as discussed in [18], [19]. A model predictive control (MPC) also called rolling horizon method is applied to solve the mixed-integer linear

programming (MILP) in [20], [21]. Although several microgrid energy management strategies are proposed in [16]−[21], they either focus on providing spinning reserve ancillary services to the grid or mitigating the internal fluctuation of microgrid. In addition, the proposed strategy in those papers cannot provide grid-supporting services that can assist main grid real-time load fluctuation or loss of generation especially with rapid growth of RESs. This could weaken the system reliability and lead to a substantial blackout. One effective solution to this challenge is to develop a novel microgrid energy management strategy to harness the internal net-load fluctuation within the microgrid.

2.2 Grid-Friendly Microgrid

Grid-connect microgrid is able to become a grid-friendly microgrid by utilizing the proposed strategies that consists of a real-time dispatch (RTD) phase and a real-time control (RTS) phase. In the RTD phase, instead of covering a single time interval, a rolling horizon based model predictive control (MPC) method that covers multiple intervals is applied to reduce the risk of dispatch failure and increase the reliability. In the RTC phase, the fast-acting battery energy storage system plays an important role of mitigating the net-load fluctuation and maintaining constant exchange power flow on the tie-line. As a result, the main grid will not be affected by the uncertainties within microgrids.

2.2.1 Two-Phase Real-Time Energy Management Strategy

In the RTD phase, all controllable units follow the on/off status obtained from day-ahead scheduling. Model predictive control is applied in this phase to determine the optimal dispatch points. In the RTC phase, the fast-acting battery energy storage system is adjusted to mitigate the sub-minute fluctuation of net-load and to maintain a constant tie-line exchange power between the main grid and microgrid. The proposed two-phase real-time energy management strategy consists of the following steps:

Step 1 is designed to update the forecasting data of load, wind and solar power before the next dispatch run.

Step 2 will formulate an economic dispatch problem to update the dispatch points for each controllable DER unit and energy storage system in the RTD phase. On-off status of controllable units will follow the day-ahead unit commitment solution and not be changed in this step. The RTD phase covers 4 time intervals. The advantage of using MPC in the RTD phase is that it can reduce the negative impact of uncertainties of the forecasting data on the system reliability by looking ahead 4 intervals for each dispatch run. Thus, potential dispatch failure may be avoided. Note that only the solution of first interval will be implemented. MPC is based on moving 'window'. In this step, the 'window' includes 4 time intervals and each time interval is set to 15 minutes. The moving 'window' has a time length of 1 hour. For example, if a 'window' includes time intervals 1, 2, 3, 4, then an economic dispatch problem is formulated for the 'window' and the optimized dispatch points are solved for intervals 1, 2, 3, 4 while only the dispatch point for interval 1 is implemented. Subsequently,

the ‘window’ will move to the next 4 time intervals (2, 3, 4, 5) after the solution of interval 1 is implemented.

Step 3: The real-time charging/discharging power of ESS in the RTC phase is adjusted every 4 seconds to mitigate real-time net-load fluctuation based on the updated real-time data of load, wind and solar energy. As shown in Fig. 1, in the RTC phase, each control interval is set to 4 seconds. The value of ‘count’ in Fig. 2.1 represents the number of 4-second time intervals that the BESS is not able to fully mitigate the net-load fluctuation In order to maintain constant tie-line exchange power flow during an RTD dispatch interval, the BESS adjusts its charging/discharging rate to alleviate the fluctuation of microgrid net-load. When reaching the end of an RTD dispatch interval, the proposed procedure continues by going back to Step 1.

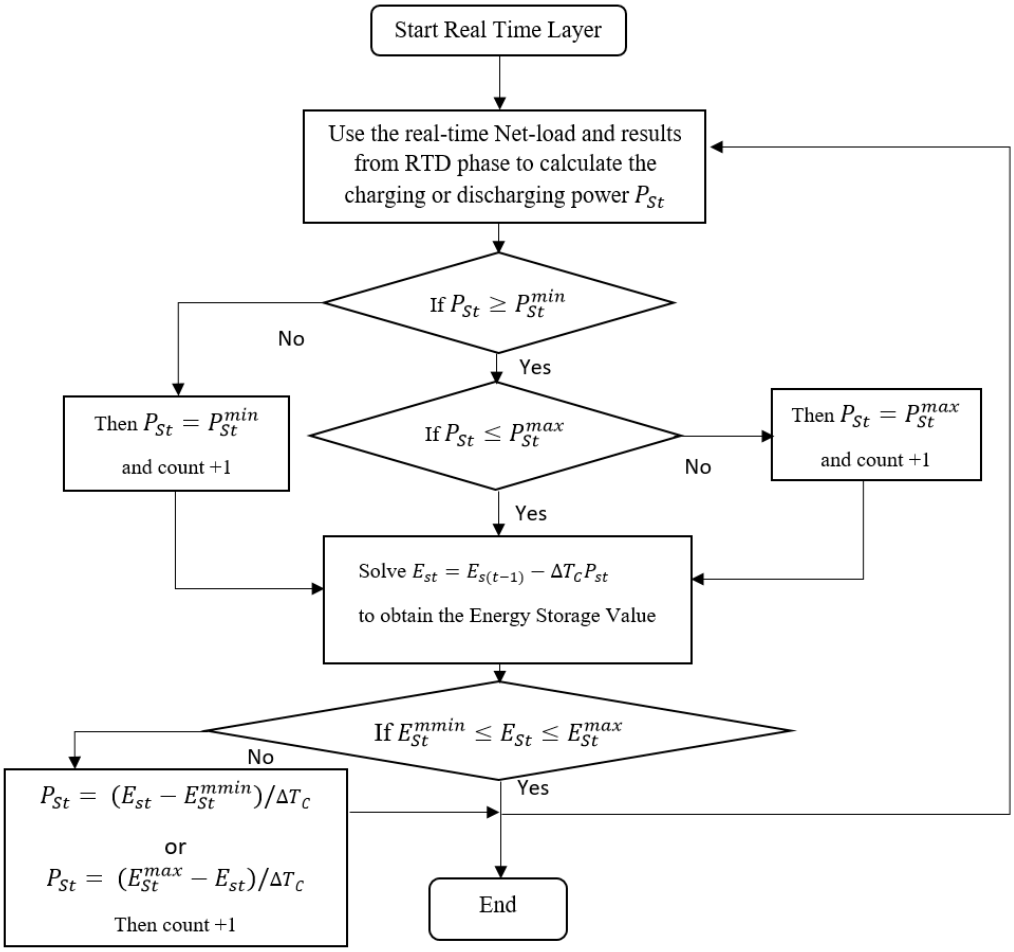

Fig. 2.1 Algorithm flow chart of the RTC phase.

2.2.2 Real Time Dispatch

The RTD phase is to solve a multi-interval microgrid economic dispatch problem. Each time interval ΔT is 15 minutes. Its objective is to minimize the operation cost over the very next multiple dispatch intervals, which is shown below,

$$f(\text{cost}) = f_G + f_{grid}, \tag{2.1}$$

where f_G denotes the cost of controllable DER units and f_{grid} denotes the grid electricity cost. f_g includes variable operation costs as,

$$f_G = \sum_{t \in S_T, g \in S_G} c_g P_{gt} \,. \tag{2.2}$$

The cost of electricity trading with grid is calculated as below,

$$f_{grid} = \sum_{t \in S_T} (c^t_{grid+} P^t_{grid+} - c^t_{grid-} P^t_{grid-}), \tag{2.3}$$

which involves activities of buying power from the grid and selling power back to the grid. The purchasing and selling power prices are different. If the cost f_{grid} is negative for any time period, it means the microgrid sells power to the grid and makes profit in that period.

Microgrid power balance equation is included in (2.4). Equation (2.5) calculates the ESS energy level. Constraint (2.6) ensures the microgrid to have sufficient backup power capacity for emergency. The maximum and minimum limits of controllable DERs are considered in (2.7). Also, the ramping limits of DERs are imposed in (2.8). The constraints of ESS charging or discharging rate limits are given in (2.9)–(2.10). Constraint (2.11) ensures that the energy storage system would not charge and discharge power at the same time. Constraint (2.12) ensures the energy stored in ESS is within maximum and minimum energy limits. As shown in (2.9)–(2.10) and (2.12), some capacity of ESS charging/discharging power and energy stored in ESS are withheld in the RTD phase for potential net-load fluctuation mitigation in the RTC phase. These reserved capacity would be deployed in the RTC phase. Tie-line exchange power limits are enforced in (2.13)–(2.14); constraint (2.15) ensures that the microgrid would not purchase and sell power at the same time. The constraints are list as:

$$P_{gridt+} + \sum_{g \in S_G} P_{gt} + \sum_{i \in S_I} P_{Ii}^t + \sum_{s \in S_S} P_{st-} = P_{gridt-} + \sum_{i \in S_L} P_{Li}^t + \sum_{s \in S_S} P_{st+}, \quad (2.4)$$

$$E_{st} = E_{s(t-1)} - \Delta T(P_{st-} - P_{st+}), (s \in S_S, t \in S_T), \quad (2.5)$$

$$P_{grid}^{max} - P_{grid+}^t + P_{grid-}^t + \sum_{g \in S_G} \left(P_{gt}^{max} - P_{gt}\right) \geq R_{percent} \left(\sum_{i \in S_L} P_{Li}^t \right) \quad (2.6)$$

$$(t \in S_T),$$

$$P_{gt}^{min} \leq P_{gt} \leq P_{gt}^{max} \quad (g \in S_G, t \in S_T), \quad (2.7)$$

$$\Delta T \cdot P_g^{Ramp} \leq P_{g(t+1)} - P_{gt} \leq \Delta T \cdot P_g^{Ramp} \ (g \in S_G, t \in S_T), \quad (2.8)$$

$$U_{s+}^t \left(P_S^{min} + \Delta P_g\right) \leq P_{st+} \leq U_{s+}^t \left(P_S^{max} - \Delta P_g\right) (s \in S_S, t \in S_T), \quad (2.9)$$

$$U_{s-}^t \left(P_S^{min} + \Delta P_g\right) \leq P_{st-} \leq U_{s-}^t \left(P_S^{max} - \Delta P_g\right) (s \in S_S, t \in S_T), \quad (2.10)$$

$$U_{s+}^t + U_{s-}^t = 1 \quad (s \in S_S, t \in S_T), \quad (2.11)$$

$$\left(E_s^{min} + \Delta E_s\right) \leq E_{st} \leq \left(E_s^{max} - \Delta E_s\right) (s \in S_S, t \in S_T), \quad (2.12)$$

$$0 \leq P_{grid+}^t \leq U_{grid+}^t P_{grid}^{max} \quad (t \in S_T), \quad (2.13)$$

$$0 \leq P_{grid-}^t \leq U_{grid-}^t P_{grid}^{max} \quad (t \in S_T), \quad (2.14)$$

$$U_{grid+}^t + U_{grid-}^t \leq 1 \quad (t \in S_T). \quad (2.15)$$

2.2.3 Real Time Control

In the RTC phase, the forecasting errors of the dispatch phase and the net-load fluctuation are addressed by quickly adjusting the BESS. All controllable units' on/off status and outputs remain the same as determined in the RTD phase. In the RTC phase, the power balance equation (2.4) is solved with actual load and DER generation to determine the battery's charging or discharging rate so that the exchange power

with the grid can remain the same as is determined in the RTD phase unless one or multiple constrains of (2.16) – (2.18) are violated which are listed below:

$$P_{St+}^{min} \leq P_{st+} \leq P_{St+}^{max}, \tag{2.16}$$

$$P_{St-}^{min} \leq P_{st-} \leq P_{St-}^{max}, \tag{2.17}$$

$$E_s^{min} \leq E_i^t \leq E_s^{max}, \tag{2.18}$$

$$E_{st} = E_{s(t-1)} - \Delta T_C(P_{st-} - P_{st+}). \tag{2.19}$$

The capacity of BESS that is withheld in the RTD phase is now released for net-load fluctuation mitigation in the RTC phase. The resulted ESS charging/discharging power after solving (2.4) should be within the limits defined in (2.16) – (2.17). Similarly, the energy stored in energy storage system that is obtained by solving (2.19) should also be within the limits as well (2.18). If all constraints (2.16) – (2.18) are satisfied, then the battery energy storage system can fully mitigate the fluctuation of net-load by itself in the real-time control phase. If any of those three constrains are not satisfied, then the grid will have to take over the responsibility to alleviate the fluctuation.

2.2.4 Results Analysis

A typical microgrid system is simulated to evaluate the proposed two phase strategy. The controllable DER units include a micro-turbine (MT), a fuel cell (FC), and a diesel engine (DE). The load in this simulated microgrid represents 1,000 residential houses. The residential load data are obtained from the Pecan Street Dataport [22]. Non-controllable DER units include solar panels installed in 200 houses (with a capacity of 5kW per house) and four 200kW wind turbine (WT) units. The

microgrid also contains an energy storage system with a 500kWh battery set, and its maximum charge/discharge power is 150kW.

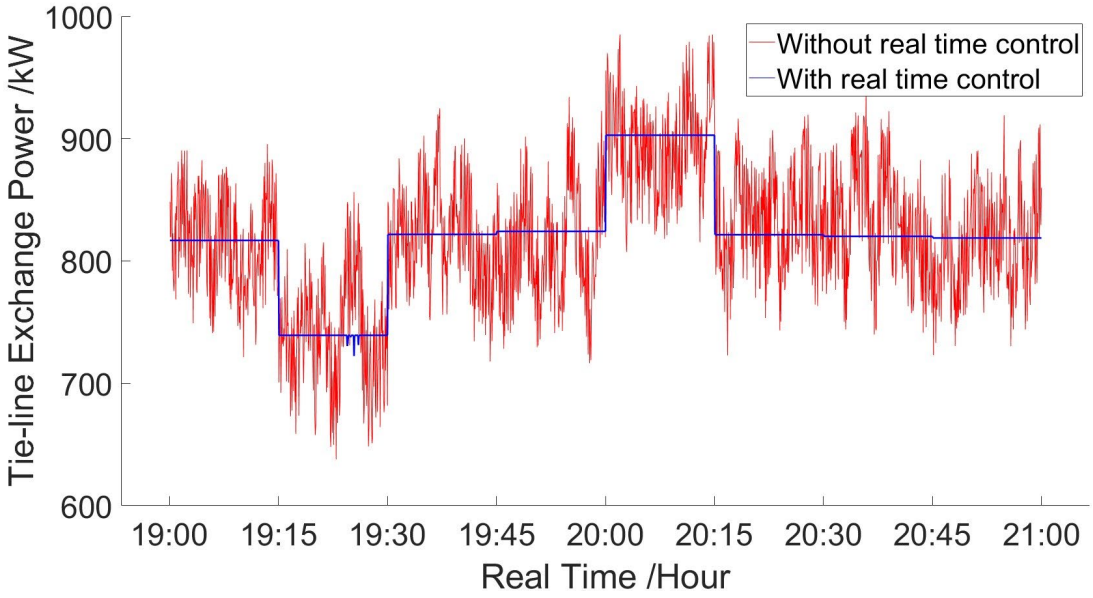

Fig. 2.1 Tie-line exchange power.

The tie-line exchange power between the main grid and microgrid is shown in Figure 2.1. The red curve denotes tie-line exchange power without the RTC while the blue curve denotes the tie-line exchange power with the RTC. After implementing the two-phase energy management strategy, the tie-line exchange power remains constant for each dispatch time interval which is 15 minutes in this work. The real-time net-load fluctuation with a 5% forecasting error are fully mitigated by the battery energy storage system.

With a 5% net-load forecasting error, the proposed strategy can mitigate the net-load fluctuation. It is observed that the tie-line exchange power is not always constant in the second dispatch interval. This is because the magnitude of the net-load fluctuation is very high and requires a power/energy compensation beyond the

battery's available capacity. Though this may be addressed by withholding extra power/energy capacity in RTD as shown in (2.9)−(2.11), it would affect microgrid operational efficiency as large forecasting error is very rare for a short-term dispatch. Without the ESS mitigation in the RTC phase, the grid would automatically respond to the microgrid internal net-load fluctuation to maintain microgrid power balance by adjusting the tie-line exchange power, which introduces additional uncertainties into the bulk power grid.

A novel metric, Fluctuation Mitigation Rate (FMR), is proposed in this section to quantify the effectiveness of the proposed two-phase grid-friendly energy management strategy as compared to a regular energy management strategy that consists of a single economic dispatch layer without consideration of real-time net-load fluctuation mitigation. As defined in (2.20), the proposed metric FMR is a percentage number that represents how much time the microgrid net-load fluctuation is 100% mitigated internally,

$$\text{FMR} = \frac{T_1}{T_2} \times 100\%, \tag{2.20}$$

where T_1 represents the cumulative time duration when tie-line exchange power keeps at the same level as dispatched in an RTD phase and T_2 represents the total time duration of an RTD phase.

For the proposed two-phase energy management strategy, the variance of tie-line exchange power, $v^{P_{Grid}}$ as defined in (2.21), is much smaller than the traditional single-phase RTD optimization. $v^{P_{Grid}}$ can be used as another metric to quantify the effectiveness of the proposed strategy as,

$$v^{P_{Grid}} = \frac{\sum \sigma^2(P_{grid}^c)}{n_D}, \tag{2.21}$$

where P_{grid}^c represents the tie-line exchange power in each 4-second RTC interval c. n_D denotes the number of 15-minute dispatch intervals in an RTD phase. $\sigma^2(x)$ denotes the variance of variable x.

Table 2.1 shows the grid exchange power statistics over results associated with 10 different net-load scenarios. When the forecasting error is between 0 to 5%, the variance of tie-line exchange power is 0 and the FMR is 100% for the proposed two-layer approach while the counterpart variance for a traditional approach without the real-time net-load fluctuation mitigation control phase goes up to over 1,000. As the forecasting error increases, the variance of tie-line exchange power deviation for the proposed method also increases. This leads to the decrease of the FMR which means the tie-line exchange power needs to be changed to balance the microgrid. Note that very large forecasting error is not common for short-term operations.

Table 2.1 Statistics of real-time tie-line exchange power for 10 different scenarios corresponding to 10 different forecasting errors

Error	without RTC		with RTC	
	$v^{P_{Grid}}$	*FMR*	$v^{P_{Grid}}$	*FMR*
0.5%	11.46	0%	0	100%
1%	45.29	0%	0	100%
2%	183.86	0%	0	100%
3%	407	0%	0	100%
4%	741	0%	0	100%
5%	1191	0%	0	100%
8%	2492	0%	0.0023	99.89%
10%	4599	0%	1.4491	99.11%
15%	10722	0%	1757	95.11%
20%	19269	0%	9485	82.72%

Table II shows tie-line exchange power statistics for a net-load scenario under a forecasting error of 10%. If the minimum and maximum values of tie-line power flow in a dispatch interval are the same, then the ESS can fully mitigate the real-time net-load fluctuation. This holds for all intervals except for the second interval. For the second time interval (19:15−19:30), $v^{P_{Grid}}$ with RTC is not zero, which indicates that the second interval does not keep a constant tie-line exchange power. The $v^{P_{Grid}}$ without RTC is much higher, which indicates that the microgrid net-load fluctuation if not addressed internally can create significant uncertainty to the bulk grid.

Table 2.2 Statistics of real-time tie-line exchange power for a net-load scenario under a forecasting error of 10%

Time	without RTC	with RTC			
	$v^{P_{Grid}}$	$v^{P_{Grid}}$	Tie-line flow (kW)		*FMR*
			Min	Max	
19:00 -19:15	4619	0	817	817	100%
19:15-19:30	4505	11.6	713	739	92.89%
19:30-19:45	4356	0	822	822	100%
19:45-20:00	4218	0	824	824	100%
20:00-20:15	5015	0	903	903	100%
20:15-20:30	4428	0	822	822	100%
20:30-20:45	4877	0	820	820	100%
20:45-21:00	4733	0	819	819	100%

2.3 Grid-Supporting Microgrid

The proposed strategy can provide flexible grid connected microgrid exchange power (trading power) to the grid. The proposed strategy consists of two steps: a routine economic dispatch (ED) optimization step along with an acceptable range of trading power determination (ARTPD) step. In the ED step, MPC method is employed to determine the targeted solutions which includes the outputs of adjustable energy

resources (AERs) and the target trading power. In the ARTPD step, the exchange power maximization and minimization problems are formed with additional AERs' constraints based on targeted solutions obtained in the first step. Then, the upper bound and lower bound of the acceptable trading power range are determined by solving those maximization and minimization problems. As a result, the grid operator will receive a data package, from the grid-supporting MG, including a target trading power and a range of acceptable trading power with the associated cost deviating from the target trading power, which provides additional flexibility to grid operations.

2.3.1 Adjustable Energy Resource (AER)

Presently, DG are widely implemented as a backup energy resource in MG. DG is a traditional DER which is portable and provide fast response. DG has the capability to turn on automatically when the battery and RESs fail to maintain the load demand. DG is modelled with minimum and maximum physical limits in (2.22), ramp-up capability in (2.23) and ramp-down capability in (2.24). C_G^t is the cost of DG represented in (2.25). These AER constraints are listed as:

$$P_{Gi}^{Min} \le P_{Gi}^{t} \le P_{Gi}^{Max} \ \left(i \in \ S_G,\ t \in S_T\right), \tag{2.22}$$

$$P_{Gi}^{t+1} - P_{Gi}^{t} \le \Delta T \cdot P_{Gi}^{Ramp} \left(i \in \ S_G,\ t \in S_T\right), \tag{2.23}$$

$$P_{Gi}^{t} - P_{Gi}^{t+1} \le \Delta T \cdot P_{Gi}^{Ramp} \ \left(i \in \ S_G,\ t \in S_T\right), \tag{2.24}$$

$$C_G^t = P_{Gi}^{t} c_{Gi} + U_{Gi} c_{Gi}^{NL} + \ V_{Gi} c_{Gi}^{SU} \ \ \left(i \in \ S_G,\ t \in S_T\right). \tag{2.25}$$

Wind turbine develops rapidly due to government incentives and development of wind farm energy management. WT is the device that can convert the mechanical power of wind to electric power. The output power of wind turbine P_{WTi}^{t} is defined as,

$$P_{WTi}^{t} = \frac{1}{2}\rho A V^{3} C_{p}, \tag{2.26}$$

where C_p is determined by the upstream velocity V and downstream velocity V_0. When $\frac{V_0}{V} = \frac{1}{3}$, C_p will have a maximum value of 0.59 [23]. Blades of wind turbine can be adjusted to a proper angle to achieve the maximum power output at different wind speed. However, at a given wind speed, the output power can be flexible by adjusting the blades' angle, which enables WT to become an AER.

2.3.2 Non-Adjustable Energy Resource (Non-AER)

Solar energy is mainly referring to the radiant light and heat from sunshine. The PV system converts the energy from sunshine to the DC current. This is followed by a DC-AC inverter which feed the grid or the energy storage system. Normally, the PV solar farm is considered as an AER since the power output can be controlled by the inverter. However, it is considered as Non-AER in this section since the PV model is roof-top solar panels of residential houses which are not controllable by MG operator. The output power of PV system depends on several factors shown as,

$$P_{pvi}^{t} = I P_f A_s \eta_{pv}, \tag{2.27}$$

which is mainly depends on solar irradiance I. P_f is the shade ratio to the sunshine. A_s represents the area of PV panel. η_{pv} represents the efficiency of PV system.

2.3.3 Load Modeling

Load model includes resident load and commercial load. Residential load represents the electricity that residents consume at any time. Commercial load represents the electricity that been used commercially, such as restaurant, mall & industry. In this MG model, only residential load is modeled as a 24-hour forecasting load with one-hour timespan.

2.3.4 Flexible Tie-Line Exchange Power

Step A is to obtain the targeted solutions in the economic dispatch time period. MPC method is applied to optimize and solve a multi–interval MG economic dispatch MILP. The objective of the problem is to minimize the operation cost of the multi-interval but only the first interval's optimal solution would be implemented.

Step B1 is to determine the upper bound of the trading power that MG can address. The objective in equation (25) is to maximize the acceptable trading power as shown below,

$$Max\ P_{Buyfgrid}^{t} - P_{Selltgrid}^{t}, \tag{2.28}$$

which can be also called as the upper bound of the trading power. The constraints of AERs are listed below:

$$P_{Gi}^{t} - P_{GiTari}^{t} \le \alpha_{Gi} \cdot P_{Gi}^{Max} \ \left(i \in S_G,\ t \in S_T\right), \tag{2.29}$$

$$P_{GiTari}^{t} - P_{Gi}^{t} \le \alpha_{Gi} \cdot P_{Gi}^{Max} \ \left(i \in S_G,\ t \in S_T\right), \tag{2.30}$$

$$(P_{Chari}^{t} - P_{SiTari}^{t})t \le \alpha_{si} \cdot E_{Si}^{Max} \left(i \in S_S,\ t \in S_T\right), \tag{2.31}$$

$$(P_{SiTari}^{t} - P_{Chari}^{t})t \le \alpha_{si} \cdot E_{Si}^{Max} \left(i \in S_S,\ t \in S_T\right), \tag{2.32}$$

$$(P_{Disci}^{t} - P_{SiTari}^{t})t \leq \alpha_{si} \cdot E_{Si}^{Max} \quad \left(i \in S_S,\ t \in S_T\right), \tag{2.33}$$

$$(P_{SiTari}^{t} - P_{Disci}^{t})t \leq \alpha_{si} \cdot E_{Si}^{Max} \quad \left(i \in S_S,\ t \in S_T\right), \tag{2.34}$$

$$P_{WTiTari}^{t} - P_{WTi}^{Max} \cdot \alpha_{wTi} \leq P_{WTi}^{t} \leq P_{WTiOpti}^{t} \left(i \in S_W,\ t \in S_T\right), \tag{2.35}$$

where α_n is the preset parameter for each AER such as DE, BESS and WT. The targeted solutions of these AERs are solved in ED optimization. Equation (2.29)−(2.30) are the release constraints of DG. Therefore, DG can operate in an acceptable power range upon adjustable parameter α_{Gi} and target output of DG. Similar to DG, BESS can operate in an acceptable power range that determined by α_{si} and target BESS output (2.31)−(2.34). In equation (2.35), the acceptable power range of wind turbine is determined by α_{wTi} and target output of WT. $P_{WTiOpti}^{t}$ is the scheduled output power of WT. Note that all the constrains in previous ED optimization model are included in this step. The solution includes maximum value of tie-line trading power and the associated cost.

Step B2 is designed to form up a minimize optimization problem to get the acceptable lower bound of trading power. The constraints and targeted outputs in step B2 are the same with Step B1. The objective function is shown below,

$$Max \ P_{Buyfgrid}^{t} - P_{Selltgrid}^{t}, \tag{2.36}$$

which is to minimize the trading power. The solution of this problem includes the minimum value of tie-line trading power and the associated cost deviating from the target trading power.

Data Package: target trading power and an acceptable range of trading power with their associated cost are packed as a data array and sent to the grid. The grid

operators will make the decision upon the dispatch point they need based on the provided data package. When the grid is suffering emergency load curtailment or loss of generation, it is a backup plan for grid operators to have an optional dispatch points.

2.3.5 Results Analysis

The target tie-line trading power for 15:15-15:30 is selling electricity to grid at a rate of 242.33 kW. BESS is on charging status with a power of 75 kW. Numerical tests are conducted on ten different combinations of adjusting parameter α_n. Table 2.3 shows the test results for scenario A. The results associate with $\alpha_{Gi}\alpha_{Si}\alpha_{WTi} = 0$ serve as a benchmark. The power range represents the interval between lower bound and upper bound of the acceptable range of trading power (kW) while cost range ($/15min) represents the interval between their associated costs. It can be observed that as α_{Gi} , α_{Si}, α_{WTi} increase, the power range expands as well as the cost range. After comparing the result of test #1 and test #2, we can tell that after increasing the BESS adjusting parameter, the upper bound of the power range keeps the same while the lower bound of the power range decreases. Since the output solved by ED optimization is 75kW which is the maximum output of BESS, the charging rate is not able to gain higher even α_{Si} is increased. Similarly, after comparing the results of test #3 and test #4, we can tell that the lower bound of the power range keeps the same while the higher bound increases. The reason is that the targeted output of DG in this scenario reaches its maximum generation. However, DG can decrease the generation in order to expand the acceptable power range.

Table 2.3 Results of 10 combinations of adjustable parameters for Scenario A

No.	α_g	α_s	α_{wT}	Power Range	Cost Range
0	0	0	0	-242.33	-1.82
1	0.05	0.01	0.05	(-247.33, -193.33)	(-1.98 ,-0.79)
2	0.05	0.02	0.05	(-252.33, -193.33)	(-2.135 , -0.79)
3	0.05	0.02	0.08	(-252.33, -169.33)	(-2.135, -0.17)
4	0.08	0.02	0.08	(-252.33, -163.93)	(-2.135 ,-0.164)
5	0.08	0.05	0.1	(-267.33, -147.93)	(-2.60 , 0.245)
6	0.1	0.05	0.1	(-267.33, -144.33)	(-2.60, 0.251)
7	0.1	0.08	0.1	(-282.33, -144.33)	(-3.06 , 0.251)
8	0.12	0.08	0.1	(-282.33, -140.73)	(-3.06 , 0.254)
9	0.15	0.08	0.1	(-282.33, -135.33)	(-3.06 , 0.258)
10	0.15	0.1	0.1	(-292.33, -135.33)	(-3.367 , 0.258)

The target tie-line trading power for 19:45−20:00 is purchasing electricity from grid at a rate of 814.33 kW. BESS is on discharging status with a power of 20 kW. Table 2.4 Shows the test results of scenario B. Similar to scenario A, while the adjusting parameter α_{Gi} , α_{Si}, α_{WTi} increasing, both power range and cost range expands. From test #1 and test #2 we can tell that the upper bound of the power range does not change, this is due to the minimum discharge power limit of BESS. We can observe the similar result when comparing test #3 and test #4 because the DG is in maximum generation. It can be concluded that the targeted solutions of AERs has a significant effect on the performance of the proposed model. If any output of AERs is on its maximum or minimum, then the acceptable power range can only expand in one direction.

Table 2.4 Results of 10 combinations of adjustable parameters for Scenario B

No.	α_g	α_s	α_{wT}	Power Range	Cost Range
0	0	0	0	814.33	28.58
1	0.05	0.01	0.05	(809.33 , 863.33)	(28.45 ,29.82)
2	0.05	0.02	0.05	(804.33 , 863.33)	(28.33 , 29.82)
3	0.05	0.02	0.08	(804.33 , 887.33)	(28.33, 30.54)
4	0.08	0.02	0.08	(804.33 , 892.73)	(28.33 , 30.57)
5	0.08	0.05	0.1	(789.33 , 908.73)	(27.95 , 31.05)
6	0.1	0.05	0.1	(789.33 , 912.33)	(27.95, 31.07)
7	0.1	0.08	0.1	(774.33 , 912.33)	(27.58 , 31.07)
8	0.12	0.08	0.1	(774.33 , 915.93)	(27.58 , 31.09)
9	0.15	0.08	0.1	(774.33 , 921.33)	(27.58 , 31.11)
10	0.15	0.1	0.1	(764.33 , 921.33)	(27.33 , 31.11)

2.4 Summary

The transition to the clean energy is challenging due to the stochastic and intermittent nature of renewable energy. Thus, it is important to develop the energy management strategies while more and more RES are integrated to the system. The existing strategies, as outlined in various papers [12]−[21], neglect the consideration of real-time sub-minute net-load fluctuations. Furthermore, these approaches operate under the assumption that the main grid can seamlessly absorb such fluctuations without incurring any costs. Unfortunately, the strategies proposed in these papers fall short in delivering grid-supporting services capable of aiding the main grid in managing real-time load fluctuations or addressing issues like the rapid growth of RESs leading to potential blackout. Thus, a novel two-phase real-time energy management strategy for grid connected microgrids is proposed for the grid-friendly microgrid in section 2.1. It consists of an RTD phase and an RTC phase. In the RTD phase, MPC is applied to determine the microgrid dispatch points. In the RTC phase, the energy storage system is used to mitigate the fluctuation in order to maintain a

constant tie-line exchange power between the main grid and microgrid for each dispatch interval. The simulation results based on a microgrid test bed show the proposed two-phase real-time energy management strategy can effectively decrease the variance of grid exchange power for a microgrid dispatch interval and mitigate the real-time sub-minute net-load fluctuation in a microgrid. In other words, the proposed strategy can harness the microgrid internal fluctuation internally and thus, relieve the negative impact of the uncertainties of microgrid net-load and contribute to enhancing the reliability of the bulk power grid.

A novel real-time GSEM strategy for grid-supporting MG is proposed in section 2.2. The main contribution of this section is that a novel energy management strategy is proposed to provide and quantify the grid-supporting service for the main grid. It consists of an ED optimization step and an acceptable range of trading power determination step. In ED optimization, targeted outputs of DERs and trading power are solved. In the acceptable range of trading power determination step, the upper bound and lower bound of acceptable power range are determined. Discussions about the relationship between acceptable power range and cost are covered as well. Numerical tests on AERs' parameters ensure that GSEM strategy can provide an acceptable range of trading power to the grid. Thus, the reliability of the grid can be enhanced by this grid service provided by MG. In summary, the proposed GSEM strategy further reinforces the grid's ability to handle the disturbance and enable the MG to be grid-supporting.

3. BESS IN ISOLATED-MICROGRIDS

3.1 Literature Review

One of most applications of the isolated-microgrid is the offshore rig platform. Gulf of Mexico (GOM) is an important region for energy resource production. Roughly 15% of total U.S. crude oil production and 5% of total U.S. dry natural gas production come from the GOM region [24]. Gas and oil made up 55% of the world's CO2 emissions from fuel in 2019, and a significant proportion came from offshore oil and natural gas (O&G) platforms [25]. Offshore O&G rigs consume 16 terawatt-hours (TWh) energy to power their operations for a year [26].

The potential of US offshore wind power is vast and estimated to be more than 2,000 gigawatts (GW) [27]. Offshore wind turbines are typically much larger than onshore wind turbines. Offshore winds are stronger and more stable than onshore winds, which leads to higher capacity factors for offshore wind farms [28]−[31]. The US has set a national offshore wind goal of 30 GW by 2030 [32]. It is also worth noting that floating wind farms that can be placed in deep and ultra-deep water regions are developing very fast.

Previous studies [33]−[37] have developed some models for the wind power integrated offshore platforms. It has been proved that the integration of wind power and on site synchronous generators can keep the stability of system's voltage and frequency in a desired level in [33]−[35]. However, the wind power accounts for a small proportion of total power supply and the traditional generators are still dominating and producing large amount of CO2 emissions. The offshore platform that

powered by the offshore wind farm and onshore grid with HVDC cable is proved as a reliable model in [13]. Therefore, the offshore platform increases the demand for onshore grid. Also, the model proposed in [36] is not self-sufficient even through there is no CO2 emissions. An independent offshore platform microgrid model is developed and simulated in [37], but traditional generators are still considered in the model, which may not help achieve the reduction of CO2 emissions in the future. For the aforementioned wind power integrated offshore platforms, they either contain traditional generators as the main source and integrated with a small portion of wind power or are lack of energy storage systems to be self-sufficient and mitigate the fluctuation caused by the wind power. Also, none of them is powered by 100% renewable energy. To bridge the aforementioned gaps, additional energy storage system is needed such as battery energy storage system (BESS) and hydrogen storage system (HESS). They are both very flexible and can mitigate the variation and intermittency of offshore renewable generation and improve the overall system reliability and resilience.

The deployment of utility-scale BESS has been increasing substantially in recent years. There was 1.5 GW operating battery power capacity in the US by 2020. Considering the planned battery storage projects, that number will rise to 16 GW by 2024. Batteries can achieve very high roundtrip energy conversion efficiencies of 90% or higher. Lithium-ion battery is the most widely used battery technology and it accounts for over 80% of U.S. large-scale battery storage due to its high energy density and low self-discharge rate [38].

HESS is also gaining popularity in recent years. One major driving force is the fast deployment of variable renewable generation while current power grids are unable to completely use up all those excess free and clean power. An effective solution selected by many nations to resolve this issue is to develop electrolyzers (El) that consume the excess power to produce hydrogen that can be stored in a high pressure tank with no self-discharge issue. Then, the hydrogen can be converted back into electricity either locally with co-located fuel cells (FC) or remotely with standalone FC where hydrogen is delivered to through pipelines. There are already many planned projects. For instance, the European Union has released their hydrogen strategy for a climate-neutral Europe that targets 40 GW of electrolyzers installed by 2030 [39]. Thus, the BESS and HESS and the offshore wind farms are able to integrated together to power the offshore platforms.

3.2 A 100% Renewable Energy Model for Offshore Microgrid Systems

The total electricity consumption from offshore oil/gas platforms is around 16 TWh worldwide in 2019. The majority offshore platforms are powered by the diesel generators while the rest mainly uses gas turbines, which emits large amounts of CO2 per year. The fast development of offshore wind turbines (WT) can potentially replace traditional fossil fuel based resources to power offshore loads. The fast development of renewable energy and storage systems have now paved the way for achieving a net-zero carbon emission offshore rig platform [27] – [39]. Nevertheless, the papers reviewed are lack of a comprehensive analysis of the potential offshore clean energy system. Thus, a feasibility test and economic analysis are investigated in this section

to evaluate the performance of the offshore hybrid renewable energy sources (OHRES) model. Battery energy storage system (BESS) and hydrogen energy storage system (HESS) are considered to mitigate the fluctuation of wind power in the OHRES model. Resilience models are designed to enhance the resilience of the OHRES model with extra energy stored in BESS and/or HESS.

3.2.1 Offshore Hybrid Renewable Energy Sources Model

The basic OHRES model consists of (3.1)-(3.18) as described below, which ensures power supply for the offshore platforms. The resilience is not considered in the basic model. The objective of the basic OHRES model is to minimize the lifetime total cost to maintain the power of the offshore platforms that presented as,

$$F(\text{cost}) = f(\text{WT}) + f(\text{BESS}) + f(\text{HESS}), \tag{3.1}$$

which includes the cost of three subsystems: wind turbine, battery energy storage system, and hydrogen energy storage system. The total cost of HESS is shown as,

$$f(\text{HESS}) = f(\text{El}) + f(FC) + f(\text{Comp}) + f(\text{Cav}), \tag{3.2}$$

which includes the cost of electrolyzer, fuel cell, compressor, and salt cavern. The hydrogen pipeline cost is not considered in this model since the OHRES model is local for an offshore platform.

Each subsystem's total cost is modeled with the capital cost, operation and maintenance cost and expected lifetime are listed as:

$$f(\text{WT}) = V_{WT}\left(c_{WT}^{Capital} + c_{WT}^{O\&M}T^{E}\right), \tag{3.3}$$

$$f(\text{BESS}) = V_{BESS}\left(c_{BESS}^{Capital} + c_{BESS}^{O\&M}T^{E}\right), \tag{3.4}$$

$$f(\mathrm{El}) = V_{El}\left(c_{El}^{Capital} + c_{El}^{O\&M}T^{E}\right), \tag{3.5}$$

$$f(\mathrm{FC}) = V_{FC}\left(c_{FC}^{Capital} + c_{FC}^{O\&M}T^{E}\right), \tag{3.6}$$

$$f(\mathrm{Comp}) = V_{El}\left(c_{Comp}^{Capital} + c_{Comp}^{O\&M}T^{E}\right), \tag{3.7}$$

$$f(\mathrm{Cav}) = V_{Cav}\left(c_{Cav}^{Capital} + c_{Cav}^{O\&M}T^{E}\right). \tag{3.8}$$

Note that the power of the compressor is equal to the electrolyzer respectively. The power balance equation involving renewable energy sources, BESS, HESS and load demand is shown as,

$$P_t^{Disc} + V_{WT}P_t^{WT} + P_t^{FC} - P_t^{Load} - P_t^{Char} - P_t^{El} - P_t^{Curt} = 0, \forall t. \tag{3.9}$$

Constraint (3.10) calculates the stored energy of BESS for each time interval. Equations (3.11)−(3.12) enforces the BESS initial energy level and the ending energy level. Constraint (3.13) forces the BESS energy level to be under the maximum limit of the BESS. Constraint (3.14) restricts the BESS in three modes: charging; discharging; or stay idle. Constraints (3.15) − (3.16) ensures the charging and discharging power are under the limits of BESS. The BESS is modeled by (3.10)−(3.16) that are listed as:

$$E_{BESS}^{t} - E_{BESS}^{t-1} = P_t^{Char}\eta_{BESS}^{Char} - P_t^{Disc}/\eta_{BESS}^{Disc}, \forall t, \tag{3.10}$$

$$E_{BESS}^{Initial} = 50\%V_{BESS}, \forall t, \tag{3.11}$$

$$E_{BESS}^{Initial} = E_{BESS}^{24}, \forall t, \tag{3.12}$$

$$0 \le E_{BESS}^{t} \le V_{BESS}, \forall t, \tag{3.13}$$

$$U_t^{Char} + U_t^{Disc} \le 1, \forall t, \tag{3.14}$$

$$0 \le P_t^{Disc} \le U_t^{Disc}P_{Max}^{Disc}, \forall t, \tag{3.15}$$

$$0 \leq P_t^{Char} \leq U_t^{Char} P_{Max}^{Char}, \forall t. \quad (3.16)$$

The structure of HESS is modeled similar to BESS. However, the "charging" and "discharging" modes are achieved by electrolyzer and fuel cell respectively; and the energy is stored in the form of compressed hydrogen in the salt cavern. Constraint (3.17) calculates the stored energy of salt cavern at each time interval. Equations (3.18)−(3.19) enforces the initial energy level in the salt cavern and the ending energy level respectively. Constraint (3.20) forces the salt cavern energy level is under the limits of the HESS. Constraints (3.21)−(3.22) ensure the power outs of electrolyzer and fuel cell are under limits respectively. Equation (3.23) ensures the electrolyzer can refill the hydrogen in the salt cavern to full capacity in 24 hours. The HESS is modeled by (3.17)−(3.23) that are listed as:

$$E_{Cav}^t - E_{Cav}^{t-1} = P_t^{El} \eta_{El} - P_t^{FC} / \eta_{FC}, \forall t, \quad (3.17)$$

$$E_{Cav}^{Initial} = 50\% V_{Cav}, \forall t, \quad (3.18)$$

$$E_{Cav}^{Initial} = E_{Cav}^{24}, \forall t, \quad (3.19)$$

$$0 \leq E_{Cav}^t \leq V_{Cav} \varepsilon_h, \forall t, \quad (3.20)$$

$$0 \leq P_t^{El} \leq V_{El}, \forall t, \quad (3.21)$$

$$0 \leq P_t^{FC} \leq V_{FC}, \forall t, \quad (3.22)$$

$$V_{El} * 24 \geq V_{Cav} \varepsilon_h, \forall t. \quad (3.23)$$

3.2.2 Resilience Models of OHRES Systems

The basic OHRES model presented in the above section can ensure the model to maintain the power supply for the offshore platforms in a typical day. However, the stochastic and intermittent characteristic of offshore wind lead to different wind

profiles in different days that may not maintain the power for offshore platforms with the basic model and may weaken the stability of the OHRES model. Therefore, a resilience model is developed to ensure that, in the worst scenario when the wind power is completely cut off, the OHRES model can continuously power the offshore platforms at least for a pre-specified time period. This time period is defined as the resilience duration T^R. Three resilience models are proposed to test and compare the performance of HESS, BESS and heterogeneous energy storage with BESS and HESS.

A. HESS Resilience Model

HESS resilience model is designed to maintain the demand only through HESS for T^R during the worst scenario. Two constraints are formulated to archive the goal of supplying the load of the rig only through HESS as shown below,

$$V_{FC} \geq P_{Max}^{Load}, \tag{3.24}$$

$$V_{BESS}\eta_{BESS} \geq P_{Rated}^{Rig}T^R, \tag{3.25}$$

where constraint (3.24) ensures the output power of the fuel cell is greater than the peak load while (3.25) ensures the hydrogen energy stored in the salt cavern is enough to cover rated load during the resilience duration.

B. HESS Resilience Model

In BESS resilience model, HESS will not be considered as a backup storage, instead, BESS will take over the responsibility of supplying the power to the offshore platforms when the wind power is not available. Similar to (3.24) and (3.25), (3.26) and (3.27) describe the power limit and energy limit respectively for BESS shown as,

$$P_{Max}^{Disc} \geq P_{Max}^{Load}, \tag{3.26}$$

$$V_{BESS}\eta_{BESS}^{Disc} \geq P_{Rated}^{Rig}T^{R}. \tag{3.27}$$

C. Joint Resilience Model

In the joint resilience model, BESS and HESS are designed to power the offshore load together during the worst scenario. Table 3.1 summarizes the proposed three resilience models. Constraints are formulated in (3.28) and (3.29) which are represented by the sum of the previous two models as below,

$$P_{Max}^{Disc} + V_{FC} \geq P_{Max}^{Load}, \tag{3.28}$$

$$V_{BESS}\eta_{BESS}^{Disc} + V_{Cav}\eta_{FC} \geq P_{Rated}^{Rig}T^{R}. \tag{3.29}$$

Table 3.1 Formulations of Resilience Models

Resilience Models	Constraints
A. HESS Resilience Model	(3.1)-(3.23), (3.24)-(3.25)
B. BESS Resilience Model	(3.1)-(3.23), (3.26)-(3.27)
C. Joint Resilience Model	(3.1)-(3.23), (3.28)-(3.29)

3.2.3 Results Analysis

A typical 50 MW offshore platform is applied as a test bed to evaluate the proposed OHRES model. The traditional model that uses diesel generators to power the offshore platform is set as a benchmark model. The load profile of the test bed offshore platform is shown in Fig. 3.1. The load profile of the offshore platform does not fluctuate like the residential load since it operates 24 hours and 80% of the load is from mining and oil processing [40].

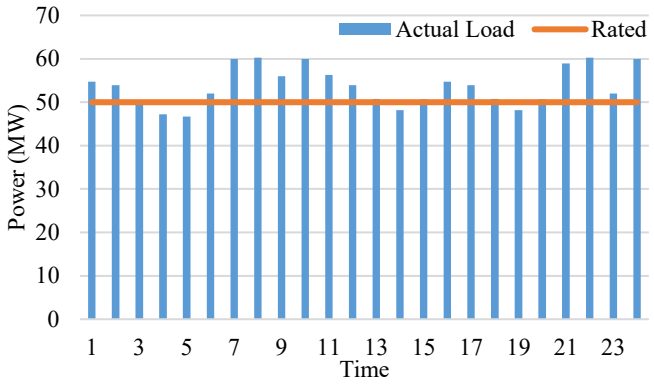

Fig. 3.1 Load profile of offshore platform.

The offshore WTs rated at 3 MW each are modeled in these case studies. Different from the onshore WTs, the offshore WTs cost much higher on the construction part. The wind power is scaled by the data from [41] for a typical day at GOM. The wind profile in Fig. 3.2 represents the available wind power for each WT. Also, the initial tests are based on the pre-set parameters shown in Table 3.2 including the costs for WTs, BESS, electrolyzer, fuel cell, compressor and salt cavern. The charging and discharging efficiency for BESS are set to 90% while it is 70% for electrolyzer and 60% for fuel cell respectively.

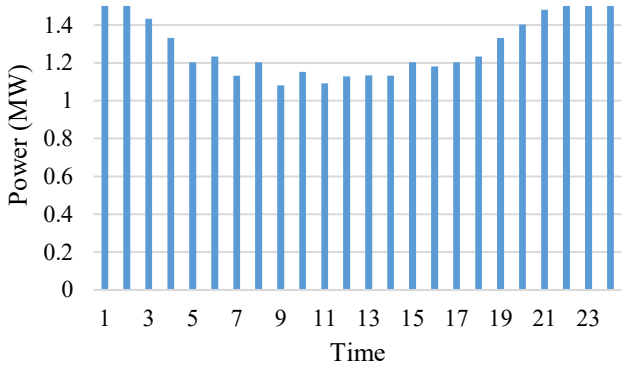

Fig. 3.2 Wind power profile for a 3 MW unit.

Table 3.2 Cost parameters

System	WT (3MW)	BESS (MWh)	El (MW)	FC (MW)	Comp (MW)	Cavern (Ton)
Cost \ million $	20	0.35	1.2	1	0.04	0.035

Tables 3.3-3.6 represent the results of the optimal 20-year planning cost for the OHRES basic and resilience models based on different length of T^R. The average cost is calculated based on the total electricity consumption for a typical 50MW offshore platform that would consume 8,760,000 MWh in 20 years. From the results, we can observe that with the increase of T^R, the average electricity cost increases for all models A, B and C. However, the costs for the basic model remain the same because the resilience is not considered there. Comparing with model A and model B, we can find that the costs for model A is higher than model B when T^R equals to 6 hours. If the T^R is greater than 6 hours, the costs for model A is lower than model B. This indicates that HESS has advantages when large amount of energy capacity is planned. For the joint model, model C has the best performance with least costs among all three resilience models. Fig. 3.2 presents the individual costs for the main components of model C in Table III. The OHRES results shown in Table VII is the results of model C from Table III. From the results, the capital cost accounts for a majority portion of the total cost in the OHRES model, while the operation cost (mainly fuel cost) is the dominating cost for traditional systems. The CO2 emissions can be reduced from 526,000 tons to zero if the traditional system is replaced by the proposed OHRES model on a 50 MW offshore platform.

Table 3.3 Results with T^R of 6 hours

Models	**Basic**	**A**	**B**	**C**
WT	42	43	42	42
BESS (MWh)	77.39	34.19	315.79	74.18
El (MW)	0.16	29.76	0	22.77
FC (MW)	0.18	60.25	0	41.71
Cavern (kg)	33.64	15151.5	0	11592.3
Capital ($ in Million)	867.51	986.62	950.53	949.29
Operation ($ in Million)	51.78	73.80	99.33	72.79
Total ($ in Million)	919.28	1060.42	1049.86	1022.08
Average ($/MWh)	104.94	121.05	119.85	116.68

Table 3.4 Results with T^R of 12 hours

Models	**Basic**	**A**	**B**	**C**
WT	42	43	42	42
BESS (MWh)	77.39	34.19	631.58	74.18
El (MW)	0.16	59.52	0	52.53
FC (MW)	0.18	60.25	0	41.71
Cavern (kg)	33.64	30303.0	0	26743.8
Capital ($ in Million)	867.51	1041.03	1061.05	1003.7
Operation ($ in Million)	51.78	88.09	162.49	87.07
Total ($ in Million)	919.28	1129.12	1223.54	1090.77
Average ($/MWh)	104.94	128.89	139.67	124.52

Table 3.5 Results with T^R of 18 hours

Models	**Basic**	**A**	**B**	**C**
WT	42	43	42	42
BESS (MWh)	77.39	34.19	947.37	74.18
El (MW)	0.16	89.29	0	82.29
FC (MW)	0.18	60.25	0	41.71
Cavern (kg)	33.64	45454.5	0	41895.3
Capital ($ in Million)	867.51	1095.43	1171.58	1058..1
Operation ($ in Million)	51.78	102.38	225.65	101.36
Total ($ in Million)	919.28	1197.81	1397.23	1159.46
Average ($/MWh)	104.94	136.74	159.50	132.36

Table 3.6 Results with T^R of 24 hours

Models	**Basic**	**A**	**B**	**C**
WT	42	43	42	42
BESS (MWh)	77.39	34.19	1263.16	74.18
El (MW)	0.16	119.05	0	112.06
FC (MW)	0.18	60.25	0	41.71
Cavern (kg)	33.64	60606.1	0	57046.8
Capital ($ in Million)	867.51	1149.84	1282.11	1112.51
Operation ($ in Million)	51.78	116.66	288.81	115.64
Total ($ in Million)	919.28	1266.50	1570.91	1228.15
Average ($/MWh)	104.94	144.58	179.33	140.20

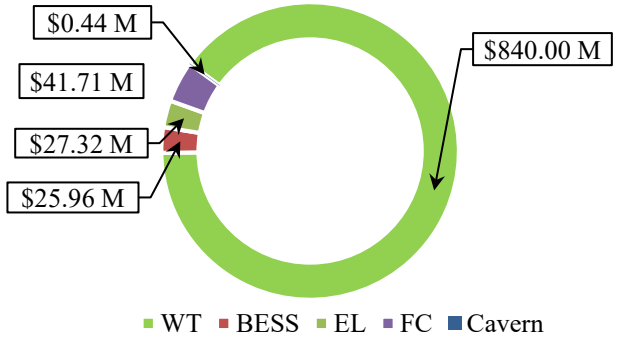

Fig. 3.3 Cost distribution for Model C in Table 3.3.

Table 3.7 Comparisons between OHRES and traditional model

Model	Capital (Million)	Operation (Million)	Total (Million)	Average ($/MWh)	Emission (tons)
Traditional	12.5	788.4	800.9	91.42	526,500
OHRES	949.29	72.79	1022.08	116.68	0

3.3 Resilient Operational Planning for Microgrid

There has been an increase in extreme events in the last few years that negatively and substantially impact our power system infrastructures, affecting

generation, transmission, and distribution of electric power, leading to disruptions of the power services to consumers. Consequently, it is important that future power system models consider methods for resilience enhancement.

Microgrid is a low-voltage local power system consisting of controllable distributed energy resources (DERs) and renewable DERs over a small territory [42]-[44]. Therefore, a microgrid on its own is inherently a resilience enhancement resource for the main power grid thanks to its ability to isolate and meet its local demand independently when an extreme event affects the transmission network or other important infrastructure of the main power systems [45]. However, microgrids are also vulnerable to these extreme events and can present issues internally that need to be addressed by appropriate resilience enhancement methods. Inverter failure rates are considered constant during continued normal operation, as any failure would be due to random event [46]. In the short-term, this would result in random failures occurring to any inverter at random as well. Under extreme weather scenarios, this inverter failure probability is increased and can largely affect the microgrid resilience. Therefore, it is important to consider and design operational models that include inverter failure probabilities to accurately determine the total generation that will be available during an extreme event.

A state-of-the-art overview showed that standard power system reliability assessments exclude the wear-out failure of power electronics and concluded that for reliability-oriented design and planning for microgrids involving a large installed capacity of power electronics-interfaced DERs, it is crucial to consider their

probability of failure [47]. Still, even though there is substantial research in the area of microgrid system resilience and strategies to ensure microgrids can continue to serve their most critical loads during extreme events, most of the research focuses on strategies related to prior scheduling of resources, system reconfigurations, component-based outage management, and forecasting methods to predict severity and level of disruption during these events [45]. Very limited research efforts investigate microgrid management considering the failure of inverter-based DERs and how to implement these to achieve a more resilient operational planning.

Holistic approaches for assessing threats and vulnerabilities in a microgrid as well as defining resilience metrics are proposed in [48] and [49]. The resilience metrics are defined based on a quantification of microgrid properties associated to the impact of an extreme event, and are defined as threats, vulnerability, and vulnerability impacts, each dependent on the other. These quantified properties are used to determine a risk parameter that can be applied to determine a resilience metric. However, both [48] and [49] do not consider probabilities of inverter failures or other components associated to the power generation of the microgrid. A statistical framework to quantify the resilience of a microgrid and ensure critical demand is met during islanding scenarios is developed in [50], where the system-level resilience metric uses asset-level reliability data and develops a dispatch routine for islanded operation to improve microgrid resilience. However, [50] focuses on optimization of available assets and implements dispatching strategies subject to failure rates in real-time once the disruption event is in progress. There is no consideration of inverter

failure-induced loss of DER, nor does it prepare the microgrid for possible scenarios beforehand.

A resilience-constrained operation strategy is proposed in [51] which uses a battery energy storage system (BESS) as a resilience resource by defining resiliency cuts for the state of charge of the BESS units. Although these resiliency cuts ensure the survivability of critical load by setting charge level limits in the BESS, this approach does not consider the probability of failure of the BESS themselves or the inverters associated with those units. A holistic operation failure rate model of power electronics systems based on overall reliability assessment is performed in [52], which features a component reliability model that involves empirical and physical models to determine operation failure rate of devices, which are then used as reliability metrics applied to a short-term outage model. Although [52] does consider failure of the power electronics of the DER, it mainly focuses on the system reliability, and it does not consider system resilience for extreme events outside a short-term low-impact outage.

Since inverter failure can lead to the loss of interconnected energy sources and hence affect a microgrid's reliability and power supply capability, this section proposes a Resilient Operational Planning (ROP) algorithm that optimizes a resilience metric for microgrid survivability rate (SR). The ROP algorithm incorporates predicted values of inverter failure probability at different stages of an extreme event to minimize the loss of power supply to critical loads and maximize the microgrid's resilience.

3.3.1 ROP Optimization Model Formulation

The ROP algorithm presented here supports decision-making for three stages of an extreme event: pre-contingency, during-contingency, and post-contingency phases. A defined time period *T* of the extreme event is divided into three sub-sets for the duration of these three stages, and inverters are assigned different probabilities of failure for each stage, with the during-contingency phase having the highest probability of failure. Based on these failure probabilities at each time interval *t*, a large number of scenarios is generated consisting of instances at which, if the particular scenario occurs, the inverter will fail at the end of that time interval if used.

The objective of the ROP optimization model is to maximize the resilience metric SR that is defined as the sum of the expected values of the successful scenarios where the power supplied by the microgrid never drops below a predefined percentage of critical load throughout the time period T. This is mathematically described by (3.30) as shown below,

$$maximize\ SR = \sum_{\omega \in \Omega} X_{\omega} \rho_{\omega}. \tag{3.30}$$

Correlations may exist between inverters, however that will depend on the type of RES and inverters used, as well as the layout of the renewable generators. Here, the inverter failure probabilities are assumed to be independent from each other given that the extreme events considered are short term, and random inverter failure rates are generally constant.

As a result of the consideration of an extreme event such as a high category hurricane or a severe winter storm, the microgrid will be considered to be in islanded

operation, assuming the main grid failed as a result of the disaster. The microgrid will only rely on controllable DERs, such as diesel generators (DG), micro-turbines (MT), and fuel cells (FC), and a set of inverters associated to renewable DERs to meet its demand. The inverters are subject to fail and the output of the optimization model will determine the decision of which distributed generators to dispatch to cover all possible scenarios, as well as which inverters to keep online during the time intervals of the disruptive event to ensure a high reliability in as many scenarios as possible and explore how the acceptable percentage threshold α of critical load affects the number of possible successful scenarios.

The microgrid will feature controllable generators for additional output in case renewable generation is not enough, constraints (3.31)−(3.32) represent the output and ramping limits of each generator, respectively. Constraints (3.33)−(3.38) model the availability, failure, and decision of utilizing the inverters at each time interval for every scenario. When the inverter is destined to fail and it is used, (3.35)−(3.38) ensure that the inverter becomes unavailable for the next time interval and remains unavailable for the rest of the time period, and if it is not used, it will remain available. Equation (3.39) defines the total available power in the microgrid to supply the critical load. (3.40)−(3.42) determine whether the critical load was successfully met at that particular time interval t for that scenario ω, and the successful indicator will be 1 when the critical load is met or 0 when it is not by implementing the "Big-M" strategy on constraints (3.40)−(3.42). Finally, (3.43)−(3.44) define whether a scenario can be considered successful: if it does not present any

unsuccessful time interval when the available power drops below the user-prespecified acceptable threshold of critical load. The constraints for ROP are listed as:

$$P^G_{min,g} u^G_{g,t} \le P^G_{g,t,\omega} \le P^G_{max,g} u^G_{g,t} \ , \forall g \in G, t \in T, \omega \in \Omega, \tag{3.31}$$

$$-R^G_g \le P^G_{g,t,\omega} - P^G_{g,t-1,\omega} \le R^G_g \ , \forall g \in G, t \in T, \omega \in \Omega, \tag{3.32}$$

$$v^I_{i,t,\omega} \le u^I_{i,t,\omega} \ , \forall i \in I, t \in T, \omega \in \Omega, \tag{3.33}$$

$$u^I_{i,t,\omega} \le u^I_{i,t-1,\omega}, \forall i \in I, t \in T, \omega \in \Omega, \tag{3.34}$$

$$w^I_{i,t,\omega} \ge v^I_{i,t,\omega} + f^I_{i,t,\omega} - 1, \forall i \in I, t \in T, \omega \in \Omega, \tag{3.35}$$

$$w^I_{i,t,\omega} \le v^I_{i,t,\omega}, \forall i \in I, t \in T, \omega \in \Omega, \tag{3.36}$$

$$w^I_{i,t,\omega} \le f^I_{i,t,\omega}, \forall i \in I, t \in T, \omega \in \Omega, \tag{3.37}$$

$$u^I_{i,t+1,\omega} \le 1 - w^I_{i,t,\omega}, \forall i \in I, t \in T, \omega \in \Omega, \tag{3.38}$$

$$\textstyle\sum_{g \in G} P^G_{g,t,\omega} + \sum_{i \in I} P^I_{i,t} v^I_{i,t,\omega} = P^{NET}_{t,\omega} \ , \forall t \in T, \omega \in \Omega, \tag{3.39}$$

$$Y_{t,\omega} \le P^{NET}_{t,\omega} - \alpha P^L_{crit,t} + M \cdot \left(1 - X^T_{t,\omega}\right), \forall t \in T, \omega \in \Omega, \tag{3.40}$$

$$Y_{t,\omega} \ge P^{NET}_{t,\omega} - \alpha P^L_{crit,t} \ , \forall t \in T, \omega \in \Omega, \tag{3.41}$$

$$0 \le Y_{t,\omega} \le M X^T_{t,\omega} \ , \forall t \in T, \omega \in \Omega, \tag{3.42}$$

$$X_\omega \le X^T_{t,\omega} \ , \forall t \in T, \omega \in \Omega, \tag{3.43}$$

$$\sum_{t \in T} X^T_{t,\omega} - (T-1) \le X_\omega \ , \forall \omega \in \Omega. \tag{3.44}$$

Since there are probabilities and scenarios involved, this model becomes a stochastic optimization problem, with the probability of each scenario determined based on the combination of the individual failure probabilities at each time interval for each inverter. To set a case for comparison, the loss of critical load of the ROP will

be compared with the critical load loss resulting from the implementation of a regular MEM [53]−[54].

3.3.2 ROP Algorithm

There are two main steps of the proposed ROP algorithm, resilient operational planning optimization and SR enhancement. The ROP algorithm flowchart is presented in Fig 3.4. In the ROP optimization step, the scenarios are generated based on the given inverter failure probabilities following a scenario generation algorithm that is illustrated in Algorithm 1. The inverter failure probabilities are assumed to be previously obtained and are used to generate the scenarios that serve as input to the ROP optimization model. This approach is taken because accurate estimation of inverter failure would require significant field data to achieve confidence, and this information is merely used as an input to the algorithm in the scope of this section. In the optimization model, binary variable X_ω would be 1 only when the aggregated power is enough to supply the critical load for all time intervals in scenario ω. The ROP optimization of section 2 will maximize the expectation of X_ω for all the input scenarios. The resilience metric SR refers to the expectation value of X_ω, which represents the possibility that the MG can supply the critical load under the given inverter failure probabilities.

Algorithm 1: Scenario generation of ROP algorithm.

1. Set the total time period T and number of inverters I.
2. Obtain the failure probability for each inverter.
3. Set the desired scenario number Ω and initialize $\omega = 1$.
4. **If** $\omega \leq \Omega$, create a matrix of (T,I).
5. **Else** Stop Algorithm.
6. **For** $t \ in \ T$
7. | **For** $i \ in \ I$
8. | | Set $X = random(0,1)$
9. | | **If** $X \leq inverter \ failure \ probability$, set ($t$,$i$) = 1.
10. | | **Else** Set (t,i) = 0.
11. | **end For**
12. **end For**
13. $\omega = \omega + 1$, and go to step 4.

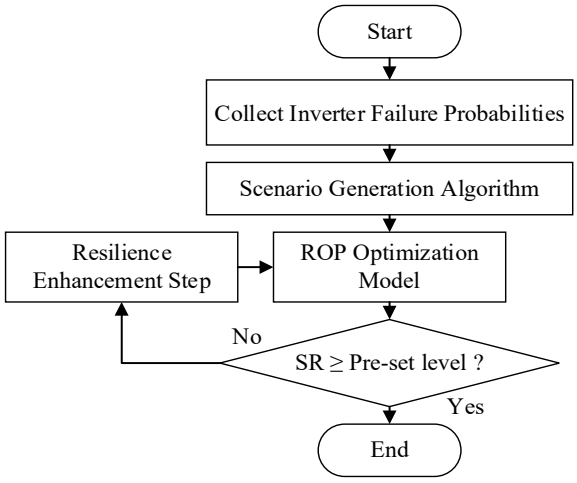

Fig. 3.4 ROP algorithm flowchart.

3.3.3 Results Analysis

To validate the effectiveness of the proposed ROP algorithm, a typical islanded MG system is modeled in this section. The testbed MG system includes three controllable DER units which are MT, FC, and DG. The parameters of the controllable DERs are shown in Table 3.8. Ten inverter-based renewable DER units including wind turbine and solar photovoltaics are modeled in the MG system. Only the

inverter-based renewable DERs are assumed to be subject to fail in this case study. The load data which represents a community microgrid with 1000 residential houses is collected by Pecan Street Dataport [22]. The critical load is set to 20% of the total load. The failure percentage of inverter is assumed to be provided by a third party. The scenarios of inverter failure are generated using the provided failure probabilities.

Table 3.8 Comparisons between OHRES and traditional model

DER	$P^G_{min,g}$	$P^G_{max,g}$	R^G_g	Op-Cost	NL Cost	SU Cost
MT	18 kW	180 kW	240 kW/h	0.08 $/kWh	$3.4	$5
FC	12.7 kW	75 kW	280 kW/h	0.18 $/kWh	$1.74	$3.5
DG	14 kW	80 kW	170 kW/h	0.16 $/kWh	$2	$5

Figure 3.5 presents a distribution of the total number of inverter failures under certain failure probability. A total of 10,000 scenarios is generated, and all the inverter failure probabilities are assumed to be 1% in this example. From Figure 3.5, it can be observed that most generated scenarios have zero inverter failures. Also, there is no scenario that contains 5 or more inverter failures at the same time. All the sensitivity tests and results shown in the rest of the section are conducted with generated scenarios like those shown in Figure 3.5. The scenarios for each test differ by the inverter failure probabilities and time intervals.

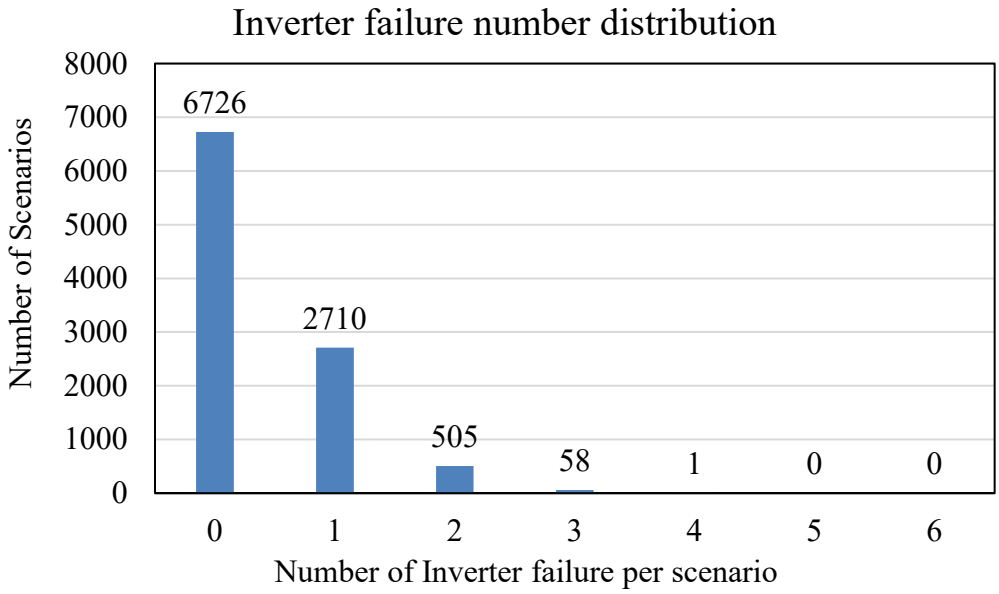

Fig. 3.5 Sample of inverter failure number distribution.

Table 3.9 presents 6 cases of inverter failures. From C1 to C6, the inverter failure probabilities increase gradually. Each case's probabilities are applied to generate a group of scenarios to evaluate the performance of the proposed algorithm. The length of the time interval is four hours. Besides the ROP algorithm, a benchmark MEM model is also set, whose objective is to minimize the total operating cost. The term SR is used to refer to the expectation value of the probability that the MG system can support enough power to a percentage of critical load. The percentage of critical load α is set to 100% in all the tests in Table 3.9. To evaluate the performance of the proposed optimization model, all values of SR are based on the ROP algorithm that excludes the resilient enhancement step in Table 3.8. The SR of C1 is 95% and is expected to decline steadily with the gradual increase of inverter failure probabilities from C1 to C6. The results shown in Table 2 meet the expectation, and these cases

will be used to model the different events for further analysis of the proposed ROP algorithm.

Table 3.9 Different cases of inverter failure and related probability

	Case	C1 [%]	C2 [%]	C3 [%]	C4 [%]	C5 [%]	C6 [%]
Prob. of inverter failure (10 Inverters)	1	0.5	1	1	2	3	5
	2	0.5	1	1	2	3	5
	3	0.5	1	1	2	3	5
	4	0.5	1	1	2	3	5
	5	0.5	1	1	2	3	5
	6	0.5	1	2	2	3	5
	7	0.5	1	2	2	3	5
	8	0.5	1	2	2	3	5
	9	0.5	1	2	2	3	5
	10	0.5	1	2	2	3	5
Microgrid SR	ROP	95	90	86	82	73	58
	MEM	86	73	63	55	40	22

Figure 3.6 compares the summary statistics of SR for ROP and MEM according to Table 2. As can be seen from the figure, both groups of SR decrease from C1 to C6. However, for the same cases, the ROP algorithm can achieve substantially higher SR than the MEM algorithm. Also, the difference in SR between ROP and MEM increases from C1 to C6. In other words, when the inverter failure probabilities increase, the proposed ROP has greater ability to enhance the value of SR compared to the MEM algorithm. From Figure 3.6, we can find that the performance of the ROP algorithm is solid and can improve the reliability of an MG significantly.

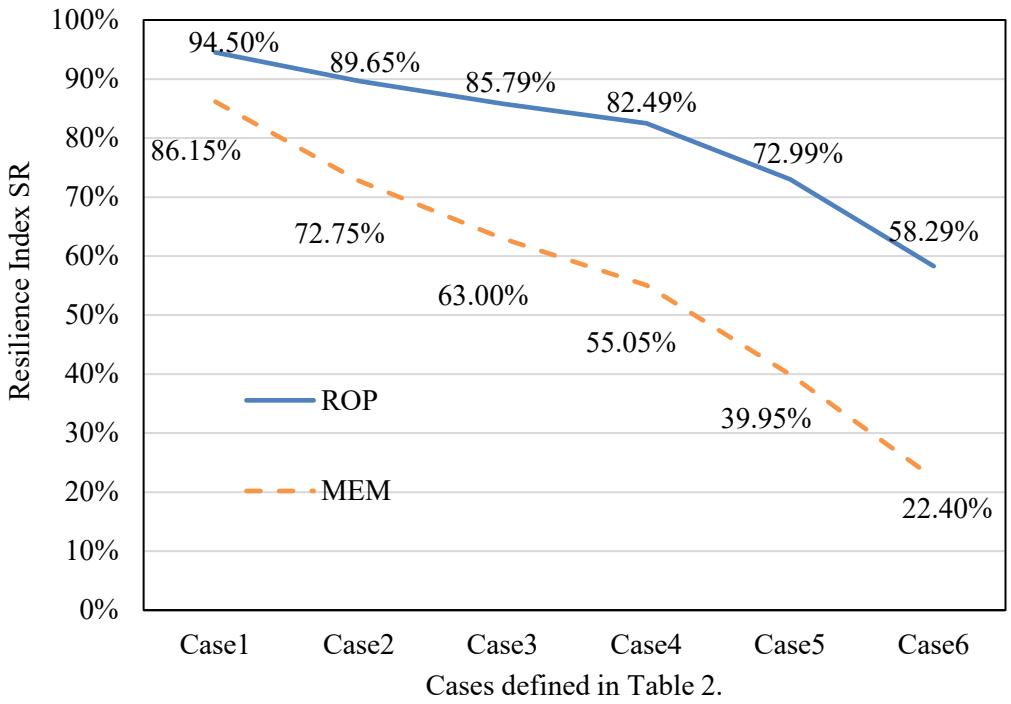

Fig. 3.6 Plot of survivability rate.

Table 3.10 presents the correlation between the value of SR and the pre-set α value. The probabilities of inverter failure are set to those of C1 from Table 3.9. The length of time interval is set to four hours. On the other hand, the value of SR will always be 100% when α value is below 95%. When α is 98%, the value of SR barely decreases to 99.5%, which means the MG is able to supply 98% power of critical load for almost all the generated scenarios. When α increases to 100%, the value of SR decreases to 94.5%. If we further increase α to 105% the MG fails to supply enough power due to the aggregated available power being less than 105% of the critical load even when there is no inverter failure.

Table 3.10 Survivability Rate sensitivity test of α

α	90%	95%	98%	100%	102%	105%
SR	100%	100%	99.5%	94.5%	94.2%	0%

To further evaluate the ROP algorithm, different events are created with different inverter failure probabilities and longer time intervals. There are a total of three events as shown in Figure 3.7. All events are designed with a 12-hour time period. The 12 hours are split into three stages: pre-contingency (hour $1-4$); on-contingency (hour $5-8$); and post-contingency (hour $9-12$). Each designed period will apply a certain case of inverter failure probabilities from Table 3.9. For non-emergency events, all three periods follow the probability from C1, which represents a normal condition with low inverter failure probabilities. The moderate event applies C2-C5-C2 for the inverter failure probabilities of the three stages, which represent a moderate condition such as a storm. The extreme event's inverter failure probabilities follow C2-C6-C2 for the three stages, which represents an extreme condition such as a hurricane. The worst condition will result on higher inverter failure probabilities. Figure 4 illustrates the inverter failure probabilities that are calculated based on the generated scenarios. The probability patterns follow the previously mentioned cases for each event. By implementing the different events, the effectiveness of the resilience improvement of the proposed ROP algorithm is verified.

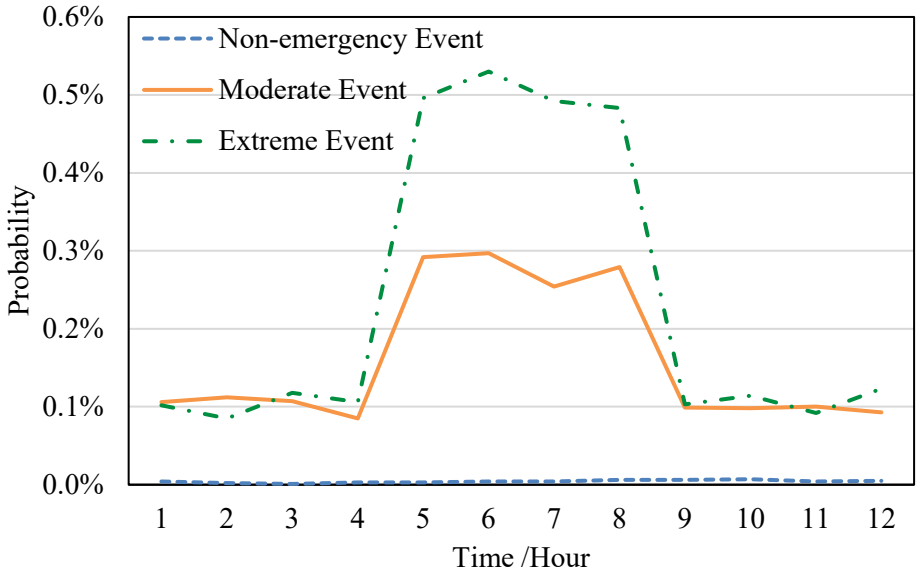

Fig. 3.7 Probability of at least one inverter failure under different events.

Table 3.11 represents the results from the implementation of the events from Figure 3.7. The value of SR for the non-emergency event is 96.2% which is over the pre-set value 95%, which reveals that the MG satisfies the requirement, and no extra DG is needed. For the moderate event, the value of SR drops significantly to 36% so the algorithm is adding an extra DG to the system. Note that the capacity of the extra DG is equivalent to the capacity of one of the inverter-based renewable energy sources. After implementing an extra DG to the system, the value of SR is updated to 97% which satisfies the requirement. The value of SR drops to 22.3% when testing the extreme event. Therefore, the same procedure of adding an extra DG is performed by the algorithm. However, after dispatching the extra DG, the value of SR increases to 94%, still not yielding the pre-set value. As a result, an additional DG is dispatched, and the SR value is finally improved to 99.9%.

Table 3.11 Evaluation of ROP under different events

SR	ROP	Add 1 DG	Add 2 DG
Non-emergency Event	96.2%	/	/
Moderate Event	36%	97%	/
Extreme Event	22.3%	94%	99.9%

3.4 Summary

This section delves into a feasibility test and economic analysis of the OHRES model. Three resilience models are designed to enhance the reliability of the OHRES model by imposing extra power capability and energy storage of BESS and/or HESS. The total cost of OHRES model increases with a higher level of resilience. Based on the current unit costs, the average electricity cost of the OHRES models are higher than the traditional onsite diesel generators. Also, the statistical economic results of the proposed system give an insight regarding when the OHRES model will be more economical than the traditional diesel generators with the decreasing cost of renewable units. To summarize, the OHRES model is feasible to replace the traditional system while maintaining the system reliability, and its zero emission benefits largely contribute to global decarbonization.

A novel resilient operational planning algorithm is proposed in section 3.2. The main contribution is that the proposed ROP algorithm can incorporate predicted values of inverter failure probabilities at different stages of extreme events to minimize the loss of power supply to critical loads. In addition, a microgrid survivability rate as a resilience metric is proposed to quantify the possibility that the microgrid will be able to supply enough power to its critical loads. The proposed

algorithm consists of the ROP optimization step and a resilience enhancement step. In the ROP optimization step, the SR is obtained, and the resilience enhancement step further improves the SR if needed. As demonstrated in the case studies section, numerical tests validate the effectiveness of the proposed ROP optimization obtaining a higher SR value than the cost-based optimization of a traditional MEM. Also, it is demonstrated that the proposed algorithm is able to improve the SR value of an MG system by analyzing different extreme events causing different inverter failure probabilities. In summary, the proposed ROP algorithm further reinforces an MG's ability to handle the critical load during emergency conditions.

4. MICROGRID ENERGY MANAGEMENT WITH BATTERY DEGRADATION MODEL

4.1 Literature Review

The proportion of RES in power generation is growing significantly. However, the system stability is substantially weakened by the stochastic and intermittent generation of high penetration RES. Battery energy storage system (BESS) is an effective flexible solution for addressing the uncertainty of variable RES induced system [55]. Thus, much more BESSs will be available in bulk power systems and small-scale microgrids in near future.

The characteristic of rechargeable chemical battery makes it degrade during cycling. This degradation can be accelerated by extreme fast charging or discharging cycles, extreme low or high ambient temperature and over charging or over discharging. However, the internal states of battery remain difficult to estimate while the battery is taking a more important role as BESS in power energy systems [7]. Therefore, the battery degradation is quite hard to predict. The working principle of a BESS is similar to a voltage source in series with impedances, but the operating conditions and environments are various for BESS in microgrids, as well as in bulk power systems. Thus, the BESS model cannot be simply treated as a voltage-source based model [56]. Li-ion battery (LiB) has been widely used as energy storage due to its high energy density and low memory effect nature. LiB degrades mainly because of the loss of Li-ions, the loss of electrolyte and the increase of internal resistance [57]. During battery cycling, the influential factors that cause the degradation include the battery operating ambient temperature, charging/discharging rate, state of charge

(SOC), state of health (SOH), and depth of discharge (DOD) [58].

Previous studies have developed some energy management strategies for BESS-integrated microgrids. In [59]−[65], it has been proved that the BESS can be seamlessly integrated into microgrid especially for those microgrids with high penetration renewable energy sources. However, battery degradation is not considered in those energy management strategies.

Some simple models of battery degradation are proposed in the literature. In [66], DOD is used to calculate the remaining useful cycles. The battery degradation is estimated based on the remaining useful battery cycle and the actual capacity. The only variable considered in [66] is the DOD and they assume the degradation process to be linear throughout the battery life which is not reasonable. Similar to [66], [67]−[70] pro-posed some DOD based models to estimate the battery degradation for each cycle which omits other important degradation factors. Pascali in [71] adopts the Butler-Volmer equation for battery degradation model to illustrate the diffusion of the solvent reactants. However, the degradation data are based on the experiment for different discharge currents and SOC values, which are not sufficient as they omit other important factors contributing to battery degradation. As mentioned in [72]−[76], the linear assumption of battery degradation may simplify the problem and reduce the computational difficulty, but the degradation value may not be accurately predicted. In summary, these popular heuristic battery degradation models can be represented as two battery degradation models [77]: (i) linear degradation model that applies a linear degradation cost based on the power output or the energy usage which

may lead to a large error on battery degradation quantification, and (ii) DOD and/or SOC based model that considers DOD and/or SOC as the input which omits the other important degradation factors such as charge/discharge rate and ambient temperature.

A temperature based battery degradation model is proposed in [78] for electric vehicle (EV). However, the model is only reflected by the internal temperature of EV's battery pack and may not suitable for the BESS. Saldana's paper [79] proposed a battery degradation matrix reference for EV. Whereas, it is impractical to consider this model in the microgrid day-ahead scheduling (MDS) problem due to the computational complexity in the optimization problem. The electric vehicle has been researched and con-ducted in the V2G system in [80]−[81] due to the similarity between EV and BESS. On the other hand, an important EV battery degradation factor, the charge/discharge rate, is neglected in those papers which may lead to an inaccurate battery degradation prediction. A data driven degradation model is presented in [82]. A quadratic equation is formed based on the collected data; however, the data are collected only under different profiles of DOD and SOC which omits other degradation related factors. References [83]−[85] present some advanced methodology to predict the lifetime of the battery cell and then the degradation can be averaged for each cycle. However, those methodologies are specially designed for the battery aging tests in which the battery's cycle is set as a fixed charge or discharge rate. In other words, the battery degradation or remaining cycle prediction is based on the fixed charging or discharging cycles in those methodologies. Therefore, they cannot reflect the degradation prediction for usage-based BESS due to the battery's

dynamic schedule such as various charge or discharge rates at different time intervals in power system/microgrid applications.

In summary, there are mainly three gaps for all the afore-mentioned battery degradation models, which are addressed in this chapter:

1) Existing models do not consider all major critical degradation factors. They focus on only a couple of variables and ignore other critical factors, which limits the accuracy of their battery degradation models.

2) BESS operations are often very dynamic; for instance, they may have very different charge/discharge rates and SOC levels at different time intervals. This is not respected by existing methods that are unable to accurately consider such dynamics in usage-based battery degradation prediction.

3) Some existing degradation models are not positioned to be efficiently incorporated into MDS.

To address the above-mentioned gaps, a fully connected neural network (NN) is proposed to train a battery degradation model, and a cycle based battery usage processing (CBUP) method is developed for the BESS scheduling to accurately predict the battery degradation with the proposed NN model. The input of the NN model is a vector of five features including ambient temperature, charging/discharging rate, SOC, DOD and SOH. This neural network based battery degradation (NNBD) model contains non-linear activation functions in the hidden layers, which makes it complex. When incorporating the proposed NNBD model into MDS, we can establish a battery degradation based MDS (BDMDS) model that can consider the equivalent

battery degradation cost.

The BESS scheduling in MDS does not always operate in a fixed charging or discharging cycle. Therefore, the CBUP method is designed to fill the research gap between the fixed-cycle based NNBD model and the dynamic BESS operation in MDS. However, such a complex neural network embedded optimization problem would be hard to solve directly. To ad-dress this issue, a neural network and optimization decoupled heuristic (NNODH) algorithm is proposed in this section to effectively solve the BDMDS problem. The proposed NNODH algorithm iteratively solves the transformed BDMDS problem that is decoupled to the battery degradation calculation and MDS optimization problems. BESS operation constraints with tighter bounds will be generated in each iteration to limit the usage of BESS which can reduce the battery degradation and the relevant cost in the next iteration. However, the microgrid's operation cost will increase if the BESS usage is limited. The goal of the proposed NNODH algorithm is to find the lowest value for the sum of battery degradation cost and microgrid operation cost. It can also record the total cost for each iteration and locate the vertex point which is also the optimal solution for the BDMDS problem. Three benchmark models are also developed to test and compare the performance of the proposed NNODH algorithm. The main contributions of this chapter are summarized as follows:

- Quality analysis is conducted on the heuristic battery degradation models.
- A set of battery cycle generators is designed to simulate battery degradation under different battery operational profiles. The key features (ambient temperature,

charge/discharge rate, SOC level, DOD and updated battery energy capacity) that affect battery degradation are collected for each cycle.

- A neural network based battery degradation model with the above five input features is proposed in this chapter and it is able to accurately predict the degradation respect to the current maximum battery energy capacity.
- A cycle based battery usage processing method is pro-posed to process the BESS profile to correctly incorporate the proposed NNBD model into MDS, addressing the inconsistence between the fixed-cycle based NNBD model and BESS scheduling.
- A BDMDS model is proposed to capture the effect of battery degradation by incorporating the proposed NNBD model into microgrid energy management.
- An NNODH algorithm is proposed to efficiently solve the battery degradation based MDS model that is hard to solve directly. Four battery usage-limiting MDS models, referred to as conserved MDS (CMDS), are developed and used by the NNODH algorithm. The optimal scheduling obtained with NNODH leads to the lowest total cost including the battery degradation cost and microgrid operation cost.
- Validation of the performance for the proposed NNODH algorithm is conducted. Case studies prove that by limiting the battery operation that leads to lower degradation, the total cost can be reduced significantly.

4.2 Quality Analysis of Battery Degradation Models

Previous studies have proved that BESS can be a perfect solution to deal with the uncertainty caused by RESs [86]−[87]. However, none of those papers consider the battery degradation of the BESS in their energy management strategy. The main component of the majority types of BESS in the current market is lithium-ion battery cell. Lithium-ion batteries are connected in parallel and/or series in the battery modules. A BESS battery pack consists of multiple battery modules. The chemical characteristics of lithium-ion batteries make it degrade during the cycling. This could lead to huge battery degradation over the years and result to financial losses for investors if it is not considered in the energy management system.

Thus, some papers proposed heuristic battery degradation models (BDMs) to mitigate the gap that the battery degradation can be considered in the energy management system. References [72] − [73] proposed a linear degradation cost parameter that is related to the power or energy usage. In other words, they added a linear battery degradation cost in the objective function in the scheduling optimization problem. A battery degradation model based on the depth of discharge (DOD) of each cycle is proposed in [79] and [88]. The degradation is calculated based on the average degradation value of each cycle respect to the experimental data that under certain DOD. These heuristic models seems reasonable and effective in the battery degradation quantification. However, they are not evaluated and compared with the real battery aging experiment data.

To evaluate the performance of the popular heuristic BDMs, this section conducted a quantity analysis of those BDMs with the real battery aging experiment data. A benchmark model is also created based on the true degradation from the experiment data to gauge the accuracy of the heuristic BDMs. Also, the real data analysis is conducted in this section. Therefore, we will be able to verify the performance of the heuristic BDMs and learn the degradation characteristic of the lithium-ion batteries.

4.2.1 Heuristic Battery Degradation Models

A. Linear Degradation Model:

The linear degradation model with a constant degradation rate [72]−[73]. The battery degradation cost (BDC) in their proposed BDM is either linear with the power usage or the energy usage of BESS. The constant degradation rate is determined with the manufacture battery data: dividing the capital cost by the projected total available energy as shown in (4.1), where the $Cycle$ represents the predicted lifecycle number, E_{BESS} (kWh) represents the maximum energy capacity of BESS and c_{BESS} represents the total investment costs of BESS. The battery degradation cost is shown in (4.2) where $P_{BESS}^{Charge,t}$ (kW) and $P_{BESS}^{Discharge,t}$ (kW) represent the charging and discharging power at time period t respectively. The degradation cost are calculated as below,

$$c_{BD} = c_{BESS}/(Cycle * E_{BESS}), \tag{4.1}$$

$$f(BDC) = \sum_t c_{BD} * \left(P_{BESS}^{Charge,t} + P_{BESS}^{Discharge,t}\right). \tag{4.2}$$

B. DOD based Degradation Model

The second BDM that proposed in [79] and [88] is based on the DOD value for each cycle. The degradation value for each cycle is determined by the average cycle degradation under that certain DOD at the experiment data. The DOD value versus predicted number of lifecycle is shown in Fig. 4.1 [15]. Different DOD values will lead to the different numbers of cycles to reach a certain percent of the original capacity. In other words, the degradation value will be different under different DOD values. The $c_{BD}^{DOD,t}$ in this BDM represents the degradation cost variable that is determined by different DOD value based on the battery degradation data as shown below,

$$f(BDC) = \sum_t c_{BD}^{DOD,t}. \tag{4.3}$$

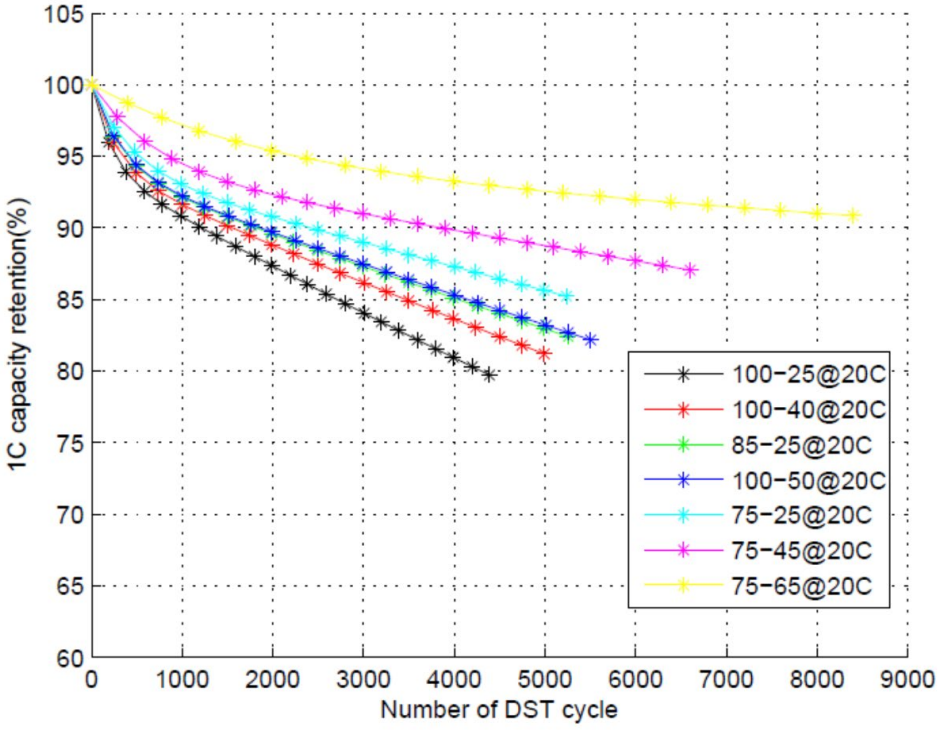

Fig. 4.1. Dynamic stress test (DST) under different DOD values [89].

4.2.2 Battery Degradation Data

The real battery degradation dataset analyzed in this section is obtained from the Battery Archive website [90] that is maintained by Sandia National Lab. It has data for over 100 lithium-ion battery aging tests, which are publically available and open source for use. Those battery aging tests covers different ambient temperature, charge or discharge rate, DOD values and different materials of cathode for the lithium-ion batteries. Table 4.1 presents the numbers of the battery aging tests under different discharge rates.

Table 4.1 Distribution of battery aging tests

Battery Aging Tests #	Discharge Rate				
Cathode Type	0.5C	1C	1.5 C	2C	3C
LCO	7	/	/	8	/
NMC-LCO	/	/	15	/	/
LFP	7	9	/	6	7
NCA	29	10	/	6	/
NMC	8	10	/	6	8

Fig. 4.2 represents six independent battery aging tests that were tested under 100% DOD, and 1.5C discharge rate at 25℃ ambient temperature. This figure gives an overview of the battery degradation results. The y axis represents the capacity of the battery and the x axis represents the cycle number. The capacity is determined by the available fully discharge capacity at each cycle. The degradation is calculated by the difference in energy capacities between two continuous cycles. From the figure, even though the six tests operates at the same condition, we can observe that the capacity curve does not overlap. Each battery performs different especially after the 700 cycles, this is due to the stochastic characteristic of lithium-ion battery. Also,

there are a lot of spikes from the capacity curve, those spikes are resulted by procedures of battery aging tests. After a certain number of cycling, they conduct a lower discharge rate for 1 cycle which results to a higher available discharge capacity for that certain cycle. In this case, the normal discharge rate is 1.5C while it is 0.5C for those spikes' cycle. Also, there are some cycles' capacities dropping down to 0, which is because those cycles are in the idle mode. Thus, when we analyze the tests, we can ignore those spikes in the following figure. Fig. 3 shows the detail of Fig. 2 by limiting the y axis between 0.5 and 3 Ah. From Fig. 3, it is more clearly to observe the capacity degrades diversely even under the same aging test condition with the same battery. This also indicates the difficulty of the battery degradation prediction.

Similar to Figs. 4.2 and 4.3, we also present another groups of battery aging tests with lithium ferro-phosphate battery (LFP). Fig. 4.4 shows the battery aging data of 4 groups of tests. From the figure, it seems the LFP is even worse in terms of performance consistency and stability. Only tests c and d follow the expected trend of the expected capacity curve. It is extreme unstable for tests a and b. Thus, we can conclude that different types of lithium-ion batteries may perform very differently.

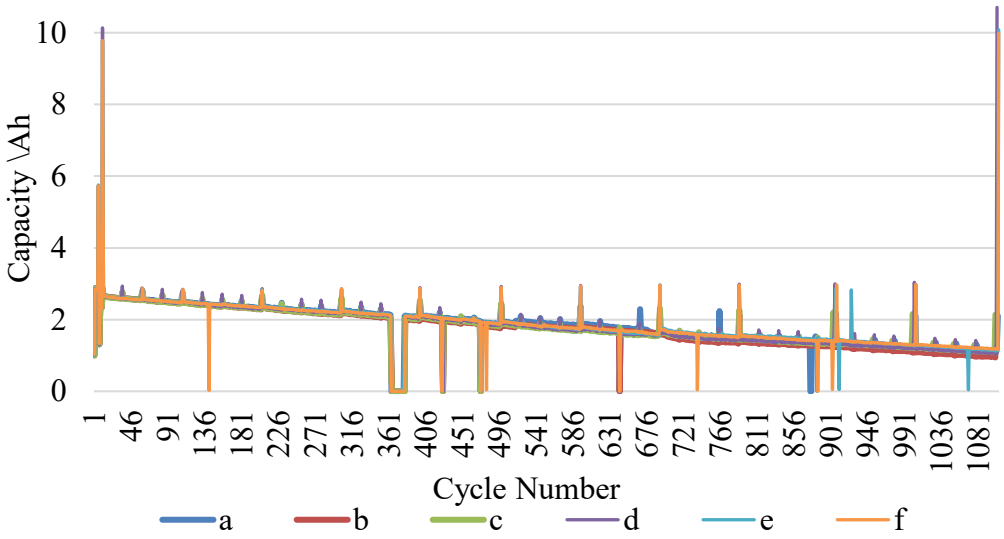

Fig. 4.2. Battery capacity curve of HNEI NMC LCO 25℃ 0-100 0.5-1.5C.

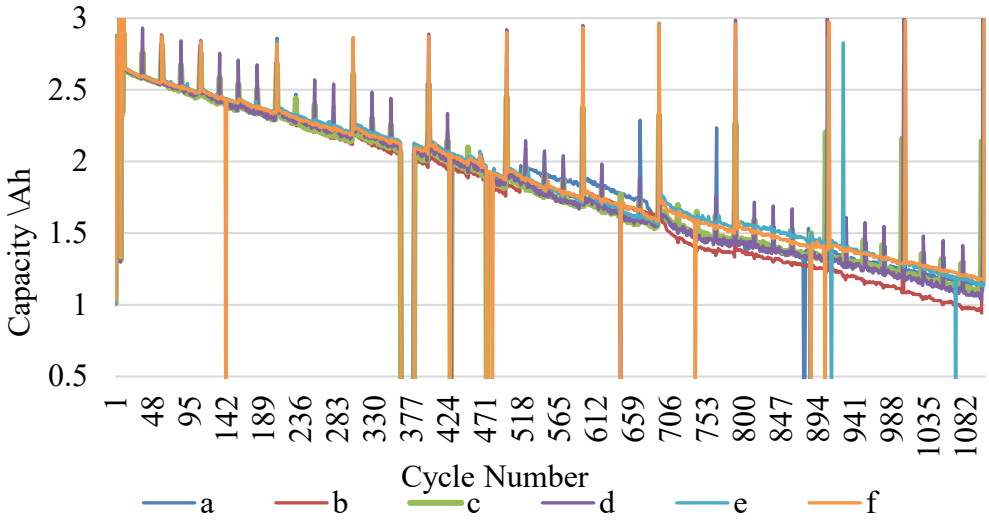

Fig. 4.3. Detailed battery capacity curve of NMC LCO 25℃ 0-100 0.5-1.5C.

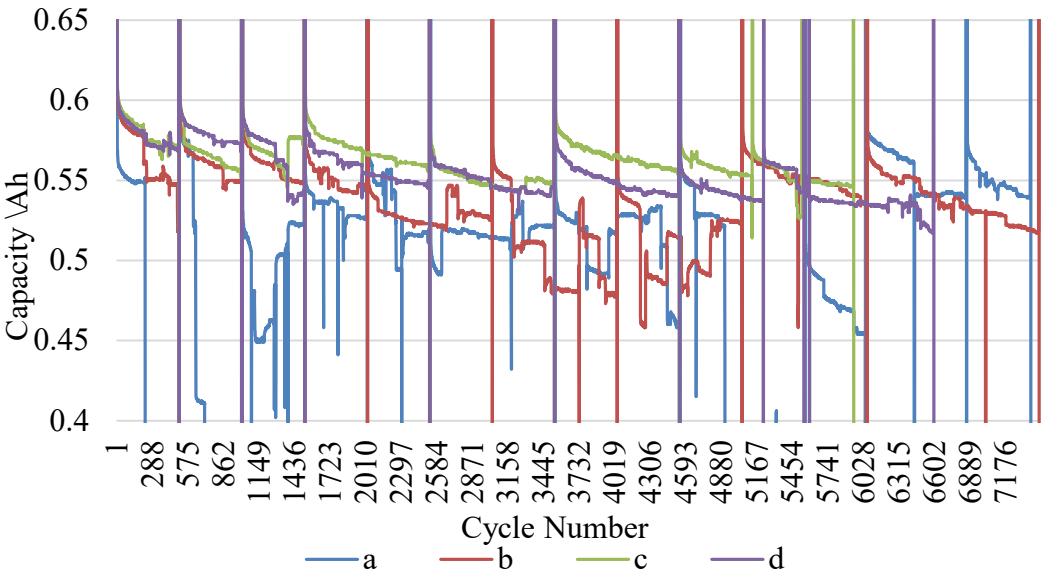

Fig. 4.4. Battery capacity curve of SNL LFP 20-80 0.5C/0.5C 25℃.

Fig. 4.5 presents the capacity curve of the same battery with Fig. 4.4 but the aging tests are under different discharge rates. The data applied here is the LFP battery at 35℃ with 100% DOD. The charge rate is kept at 0.5C while the discharge rate varies by 0.5C, 1C, 1.5C and 2C for 4 battery aging tests respectively. From the figure, we can tell that the test with 3C discharge rate has the highest degradation among all other aging test while the degradation for 1C and 2C discharge rates is similar to each other. The 0.5C discharge rate results into the lowest degradation value. It seems that a higher discharge rate will lead to a higher degradation value.

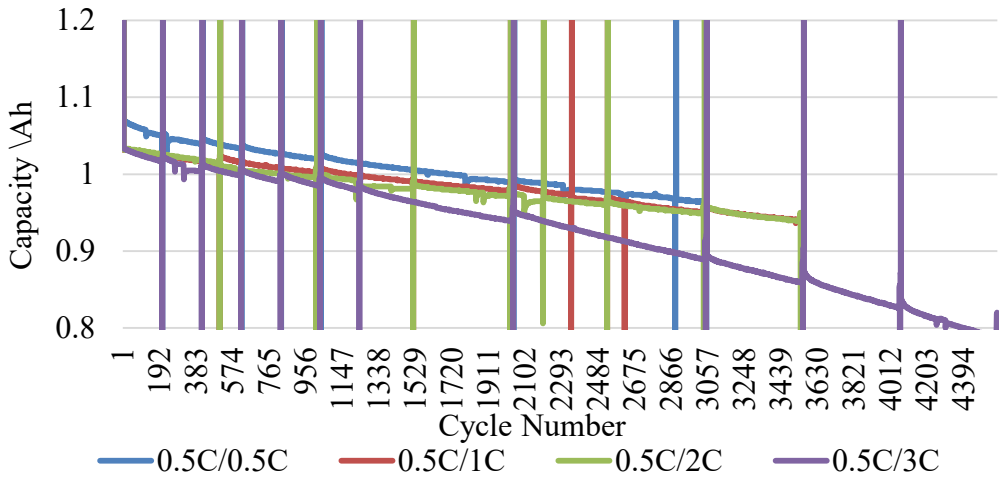

Fig. 4.5. Battery capacity curve of SNL LFP 0-100 25℃.

There are also some battery degradation tests with different ambient temperature from the dataset. Fig. 4.6 shows the capacity curve under different operating temperature. All the aging tests applied here is under 1C charge rate and 100% DOD. From Fig. 4.6, we can observe that the higher ambient temperature leads to a higher battery degradation value. It takes more cycles for the battery test under 15℃ to degrade to the same capacity level than the battery aging test under 25℃ and 35℃. The lowest ambient temperature test that is available is 15℃. We believe that the extreme low temperature (lower than freeze point) will fast degrade the battery as well [18]. Unfortunately, there is no such real degradation data to prove it. Also, if we increase the discharging rate to 2C, the previous conclusion from Fig. 4.6. is not true anymore. Fig. 4.7 shows that the battery has the lowest degradation when the ambient temperature is at 25℃. This may not be true if we switch to another type of battery.

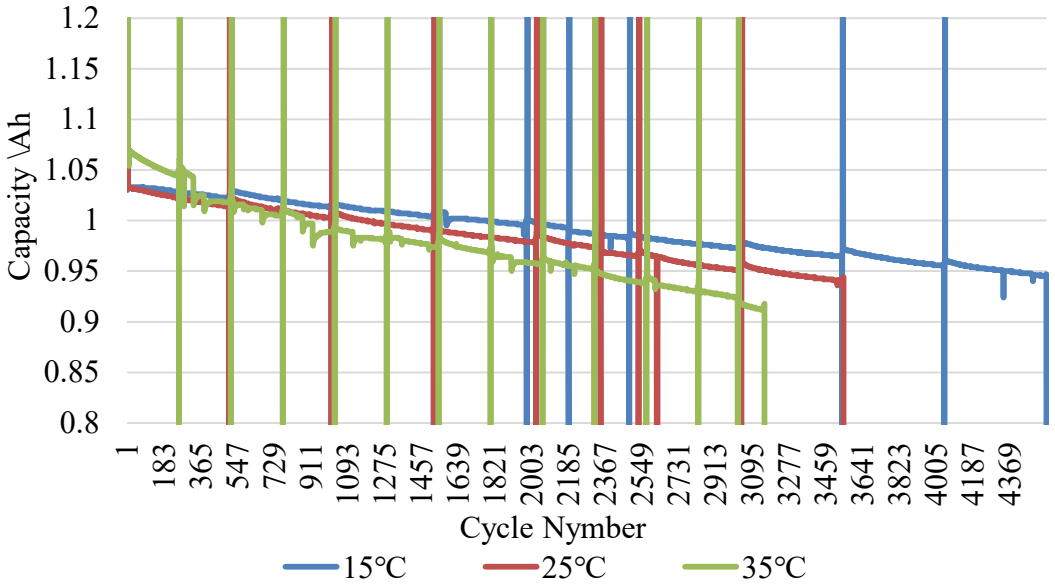

Fig. 4.6. Battery capacity curve of SNL LFP 0-100 1C.

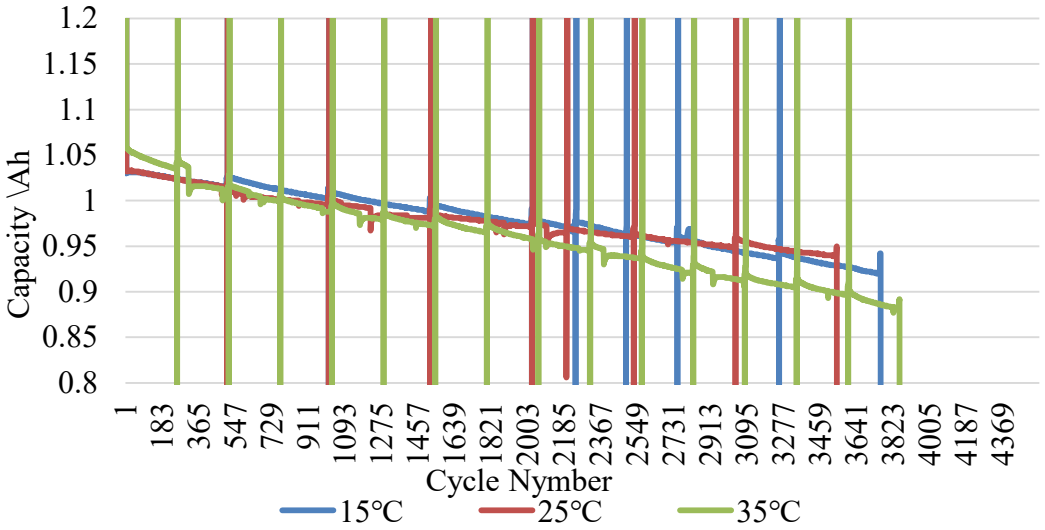

Fig. 4.7. Battery capacity curve of SNL LFP 0-100 2C.

4.2.3 Heuristic Battery Degradation Models Comparison

The quality analysis of heuristic BDMs used in the literature is conducted in this section. There are three models studied in this section: two heuristic models and

one benchmark model. Model 1 and model 2 represent the two popular heuristic models mentioned in the previous section, referred to as linear BDM and DOD related BDM respectively. The benchmark model represents the averaged degradation value for each cycle from the real degradation data. The quality analysis is applied with different scenarios including different ambient temperature, charge or discharge rate and DOD. Note that the c_{BD} and $c_{BD}^{DOD,t}$ for model 1 and model 2 are determined by one group of the aging tests from the real battery degradation data mentioned in section III. The battery degradation value of the benchmark model is the average degradation for each cycle based on the real battery degradation data under certain scenarios.

Fig. 4.8 presents the performance of the BDMs under different operating ambient temperature. The three groups of battery aging tests from the dataset that we applied here are the "100% 1C SNL 15 a", "100% 1C SNL 25 a" and "100% 1C SNL 35 a" respectively. We can observe that battery degradation predictions by model 1 are the same under different operating ambient temperature, so does model 2. This is because these heuristic popular BDMs do not consider the effectiveness of ambient temperature in their model. Compared to the benchmark model, the most accurate prediction on battery degradation value is model 2 at 15℃. This might be because the aging test that determines the $c_{BD}^{DOD,t}$ in model 2 is under a similar testing condition with the aging test of "100% 1C SNL 15". The benchmark model shows that the average degradation per cycle at 35℃ is double more than 15℃. The degradation value at 25℃ increases 25% from 15℃. It seems that a lower ambient temperature

may lead to a lower battery degradation value. However, this may not be true; no further analysis can be conducted for now since there is no battery aging tests under extreme low ambient temperature in the battery archive dataset. From Fig. 4.8, we can conclude that the heuristic BDMs predict the battery degradation value with huge errors under different operating ambient temperatures. In other words, the heuristic BDMs are unable to perform well when dealing with varying ambient temperatures.

Fig. 4.9 shows the performance of BDMs under different discharge rates. The charge rate is fixed as 0.5C of the selected aging test data. “100% 1C SNL 15 b” and “100% 2C SNL 15 b” are the two groups of aging tests that are analyzed here. The DOD and the ambient temperature are fixed with 100% and 15℃. From Fig. 4.9, similar to the previous analysis, model 1 and model 2 perform the same on the battery degradation prediction with different discharge rates. Compared with the benchmark model, Model 2 predicts the same degradation value when the discharge rate is 1C. However, both model 1 and model 2 have low accuracies on the battery degradation prediction at the 2C degradation rate. Thus, we can conclude that the heuristic popular BDMs may not work well with different discharge rates. For benchmark model, the battery degradation value at 2C discharge rate is higher than it at 1C. We believe the 3C discharge rate will lead to a much higher degradation value. However, the database doesn’t have enough 3C discharge rate data to be analyzed.

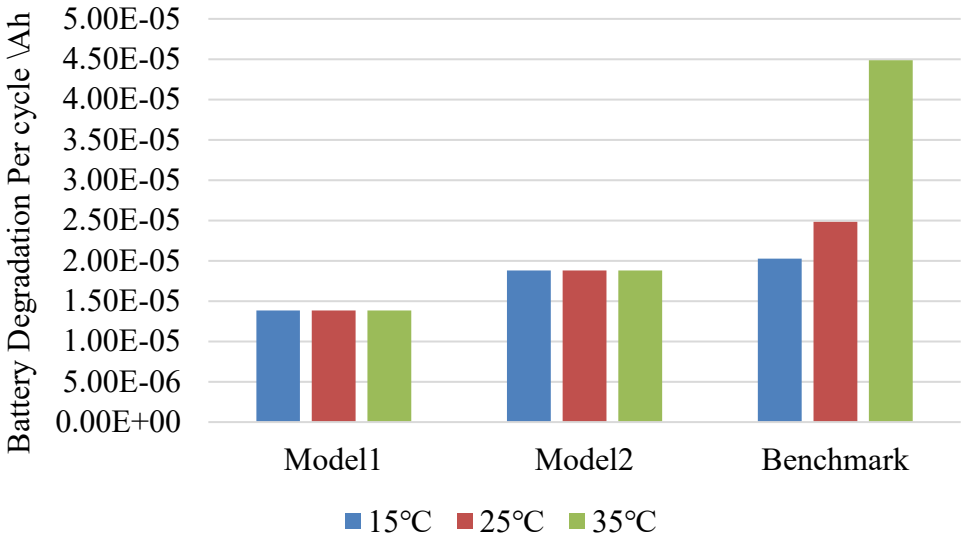

Fig. 4.8. Degradation comparison under different ambient temperatures.

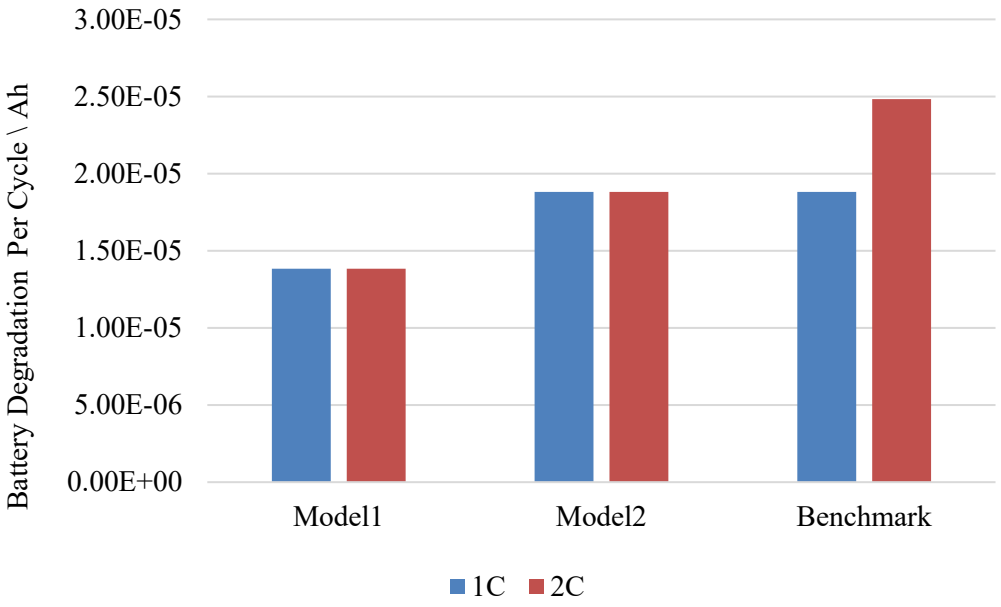

Fig. 4.9. Degradation comparison under different discharge rates.

The DOD is also a key factor that affects the battery degradation value. Fig. 12 presents the results of the BDMs with different DOD value. Three battery aging tests with different DOD values of 100%, 60% and 40% respectively from the battery

degradation dataset are used here for the analysis. It is clear that all three models share the same pattern that higher DOD values result into higher degradation values. This results also meet the expectation of the heuristic BDMs. However, the accuracy of the prediction of model 1 and model 2 is low. The scenarios that determine c_{BD} and $c_{BD}^{DOD,t}$ are different from the aging tests that are selected here, which leads to the inaccurate battery degradation prediction. In other words, the aging test that applied to determine the degradation parameter in the heuristic models is the key to improve the prediction accuracy. It may need to update the c_{BD} and $c_{BD}^{DOD,t}$ each time to keep the prediction accurate. However, the open source battery degradation data are limited and such data are not always available practically. Thus, a better BDM is required to accurately predict the battery degradation with limited degradation data resource.

4.3 Neural Network Based Battery Degradation Model

The traditional microgrid day-ahead scheduling model determines the optimal operational profiles for BESS, controllable generators and tie-line exchange power. However, the BESS in traditional MDS model is considered to be ideal with-out any degradation and the equivalent battery degradation cost is zero. This may substantially accelerate the aging and replacement of expensive BESS which may lead to economic loss in the long run. Besides, the BESS degradation needs to be accurately quantified for various battery daily operational profiles to obtain the truly optimal scheduling solutions. Thus, a deep learning method, particularly a deep neural network, is proposed in this section to accurately predict the BESS degradation.

4.3.1 Input Data for Neural Network Model

The deep neural network is applied to learn and predict the battery degradation with several critical features. A battery model implemented in the MATLAB Simulink [91] is used to conduct the battery aging tests. The aging test model is modelled with the battery model and cycling generator in Simulink. The SOC variable can be adjusted in the battery setting. The battery model of Simulink contains several default types of batteries and the battery parameters can also be adjusted with the manufacture's datasheet if we want to introduce a new type of battery. It can also simulate the ambient temperature effects and aging effects of battery. A dynamic internal resistance that is highly related to the battery degradation is also simulated within the battery model. This battery model can simulate various types and configurations of batteries, various conditions, and operating profiles. Built upon this battery model, a battery cycle generator is designed to simulate the charging and discharging cycles under the preset charging/discharging rates. For each battery aging test, each cycle is simulated to discharge from a certain SOC to a certain lower SOC and then charge back to the starting SOC. The data collected from the battery aging tests include the ambient temperature, charging/discharging rate, SOC, DOD and reduced energy capacity level. The battery's energy capacity level for each cycle is also used to calculate each cycle's battery degradation value. Table I lists the numbers of battery aging tests that are simulated under different SOC and DOD. Each battery aging test represents a group of simulated battery profile under initial SOC and fixed DOD until the battery capacity degrades to 80% of the maximum rated capacity. This

indicates each battery aging test may contain different numbers of cycles. It is common to consider the 80% of the rated capacity as the end of battery's life in battery aging test [92]. For instance, the "4" in Table 4.2 means there are four battery aging tests that are simulated at an initial SOC level of 100% with a DOD level of 10%. Moreover, each of these SOC&DOD combinations will be simulated under different ambient temperatures and charging/discharging rates. The charging/discharging rate is also referred as C rate. C rate measures the speed at which a battery is fully charged or discharged as shown below,

$$C\ rate = \frac{I_{Battery}}{E_0}, \tag{4.4}$$

where $I_{Battery}$ represents the charging/discharging current of the BESS and E_0 denotes the rated capacity of BESS. For example, 2C means the battery will discharge the full capacity in 0.5 hour. This work conducted 945 different battery aging tests with different values of degradation factors.

Table 4.2 Numbers of battery aging tests under various SOC and DOD levels

	Initial SOC					
DOD	100%	80%	60%	50%	40%	20%
20%	4	5	17	23	22	23
30%	20	34	36	32	37	/
40%	36	41	41	40	44	/
50%	38	41	36	42	/	/
60%	37	37	37	/	/	/
70%	41	36	/	/	/	/
80%	39	35	/	/	/	/
90%	35	/	/	/	/	/
100%	36	/	/	/	/	/

4.3.2 Data Pre-processing

The battery capacity level or SOH in percent at the end of each cycle is recorded from each simulation of battery aging test. Battery degradation per cycle is defined as the difference between the initial SOH and ending SOH for a given cycle. However, for some battery aging tests with low C rates and small DODs, the degradation for some cycles may be too less to measure and could even be zero. Also, some of the degradation data contain outlier points which may require some further process for a better training result. The battery degradation data are processed with different methods: (i) raw, (ii) smoothed method, and (iii) regressed method, as shown in Fig. 1. "Raw" represents the original data without any pre-processing and the associated training results can be used as a benchmark to gauge the effectiveness of the other two pro-posed data pre-processing methods. The smoothed method filters out the outliers of the raw data. Regressed method applies linear regression on the smoothed data. All three groups of input data are normalized to increase the training efficient-cy. The normalization used in [93] is applied in the data pre-processing and shown as,

$$\widehat{x_k} = \frac{x_k - E(x_k)}{\sqrt{Var(x_k)}}, \tag{4.5}$$

where $E(x_k)$ represents the expectation of x_k and $Var(x_k)$ represents the variance of the x_k. The input data will be split into two parts, 80% as the training dataset and 20% as the validation dataset. At last, three groups of data will be fed into the NN separately to evaluate their performance.

Data preprocessing is conducted with the smoothed method to reduce the random variation representing random measurement errors, which makes it harder to train a neural network model. Also, the MDS problem in this section means that we focus on the degradation cost for a relatively long period which is typically 24 hours. Comparing with the unsmoothed data and the smoothed data, we found for the same cycle, the total battery degradation is almost the same for a 24 hour time period. However, the training accuracy of the NNBD model can be increased by smoothing out the input data while the prediction error does not increase with the smoothed data. The reason is that the unsmoothed data is quite unstable in some short period as shown in the Fig. 4.10, which increases the training difficulty and decreases the training accuracy of the machine learning model. However, if we look at the degradation for a long time period, the smoothed data and the unsmoothed data have a similar degradation value as shown in Table 4.3. The cumulative degradation numbers in Table 4.3 are calculated based on the battery aging test with 60% SOC, 20% DOD, 0.75 C rate and 32℃ ambient temperature. There are five cycle intervals analyzed in Table II; from the results, we can observe that the total degradation value for the certain interval between the raw data and the pre-processed data are very similar. Also, when the length of the interval increases, the difference between the raw and the pre-processed data decreases. This ensures that the data pre-processing method improves the training accuracy without affecting the cumulative degradation value.

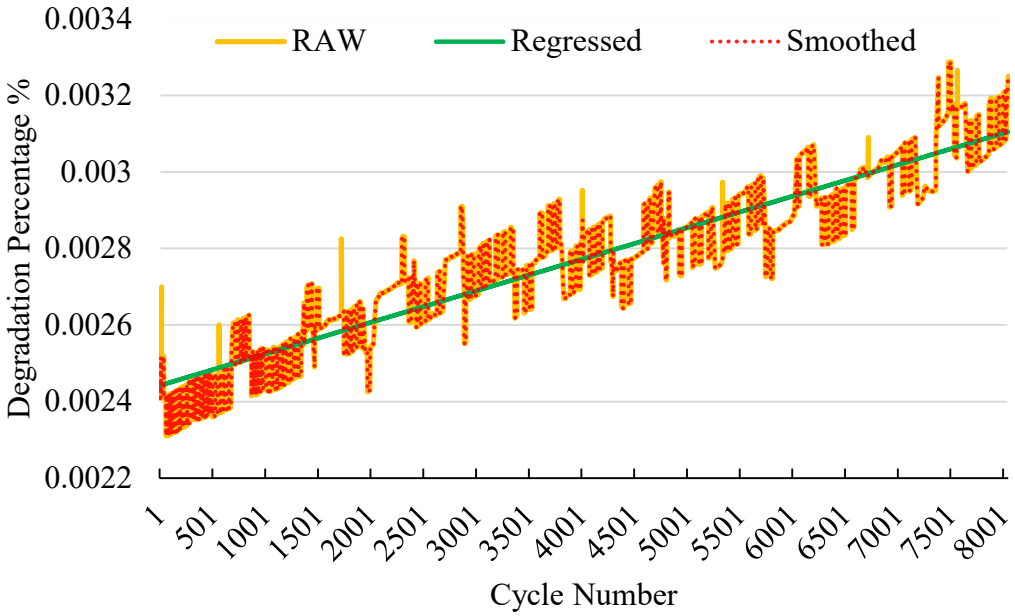

Fig. 4.10. Battery degradation data under different data processing methods.

Table 4.3 Cumulative degradation comparison over raw data and pre-processed data

Cycle Range	Raw data degradation	Pre-processed degradation	Difference
0-500	1.213%	1.231%	1.5%
0-1000	2.454%	2.483%	1.18%
0-1500	3.711%	3.752%	1.10%
0-2000	5.007%	5.048%	0.82%
0-2500	6.347%	6.362%	0.24%

4.3.3 The Proposed NNBD Model

A fully connected neural network is constructed to model the battery degradation. Five aging factors (ambient temperature, C rate, SOC, DOD and SOH) form a five-element input vector for the neural network. Each input vector corresponds to a single output value which is the amount of battery degradation in percentage respect to the SOH level for the same cycle. A dynamic learning rate scheme is used in the training process to improve the training result. The learning rate will decrease

automatically after a certain number of training epochs. The structure of the trained neural network is shown in Fig. 4.11 plotted by NN-SVG [39]. It has an input layer with 5 neurons, first hidden layer with 20 neurons, second hidden layer with 10 neurons and an output layer with 1 neuron. The activation function for the hidden layers is ReLU and "linear" for the output layer.

Mini batch gradient descent strategy is applied to train the neural network. Different batch sizes are tested to achieve the best training results. Mean squared error (MSE) represents the average of the square of the difference between the actual and predicted values over all training data points. MSE is used as the criterion, a loss function, to train the neural network and measure the neural network quality shown as,

$$MSE = \frac{1}{n}\sum_{i=1}^{n}(y_i - \tilde{y}_i)^2. \tag{4.6}$$

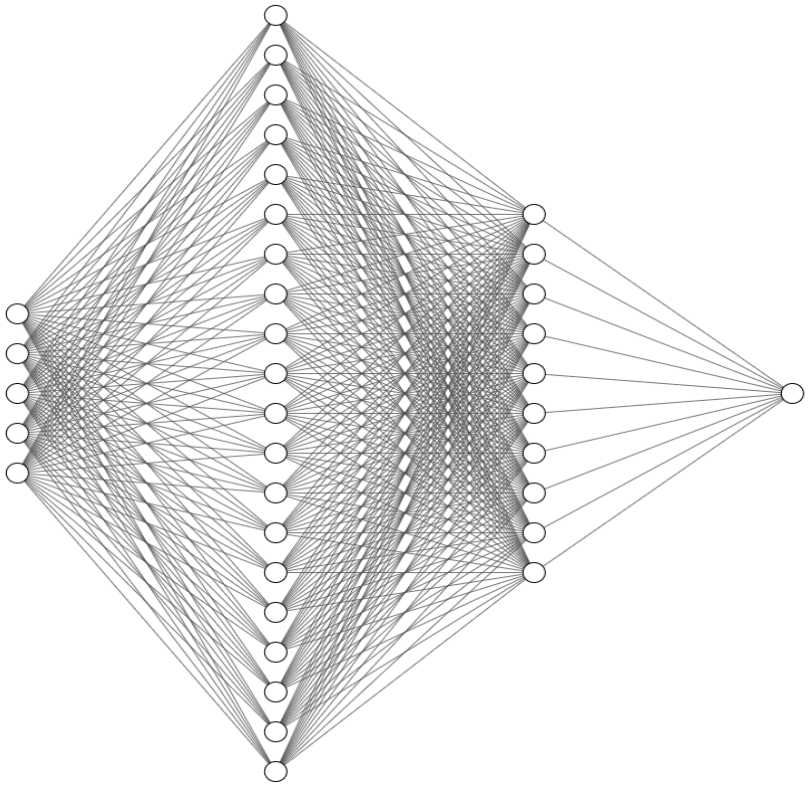

Fig. 4.11. Structure of the proposed NNBD model [94].

4.3.4 Battery Degradation Calculation

From the BESS operation profile, the SOC level is required as the input of the proposed NNBD model. The absolute value of the difference in the SOC levels between time intervals t and $t-1$ will be the DOD level as shown in (4.7). C rate is calculated by (4.8). It is assumed that the battery SOH level is available prior to the microgrid day ahead scheduling. The input vector can be formed as shown in (4.9) and then fed into the trained NNBD model to obtain the total battery degradation over the MDS time horizon in (4.10). The degradation calculation is formulated as:

$$DOD_t = |SOC_t - SOC_{t-1}|, \tag{4.7}$$

$$C_t^{Rate} = DOD_t/\Delta T, \tag{4.8}$$

$$\overline{x}_t = (T, C, SOC, DOD, SOH), \tag{4.9}$$

$$BD = \sum_{t \in S_T} f^{NN}(\overline{x}_t) SOH. \tag{4.10}$$

4.3.5 Cycle Based Battery Usage Processing Method

The equation (4.10) for battery degradation calculation mentioned in the previous section covers all the time periods for the microgrid day ahead scheduling. However, the BESS is not scheduled in fixed cycles with constant charge/discharge rates per MDS, leading to inconsistency with the fixed-cycle based data that are used for training NNBD model which is the gap mentioned in the introduction section. Furthermore, the idle status is also considered in (4.10) but it is out sampled for the NNBD model. In other words, equation (4.10) considers each time interval as a BESS cycle and feeds the associated data directly into the NNBD model, which may not accurately predict the BESS degradation. Therefore, the proposed cycle based battery usage processing method is developed to address the inconsistency and accurately apply the proposed NNBD model in the MDS problem.

In the CBUP method, instead of considering each time interval as a cycle, the operating time intervals of BESS scheduling are combined and averaged into different cycles. For any continuous time intervals, if the operation status (charging or discharging) does not change, they will be aggregated as a single charging or discharging cycle. For the aggregated cycle, the charging or discharging power will be the average of the aggregated time periods. The SOC will be the initial SOC value of the first time period in the aggregated time periods and the DOD will be the absolute

value of the SOC difference between the start time period and the end time period respectively. Thus, equation (4.10) is replaced by (4.11) while $\overline{x}_c$ represents the input vector for the aggregated cycles and AC represents the set of feasible aggregated cycles shown as,

$$BD = \sum_{c \in AC} f^{NN}(\overline{x}_c)\, SOH. \tag{4.11}$$

4.3.6 Incorporating NNBD into Microgrid Scheduling

A traditional MDS model is established as a basic model to gauge the proposed BDMDS model. This traditional MDS model consists of (4.12)−(4.26) as described below and it does not consider battery degradation.

The objective of this traditional MDS model is to minimize the total cost of the microgrid operations as illustrated in (4.12). The power balance equation involving controllable generators, renewable energy sources, power exchange with the main grid, BESS output and the load is shown in (4.13). Constraint (4.14) enforces the power limits of the controllable units such as diesel generators. The ramping up and down limits are enforced by (4.15) and (4.16). Equation (4.17) ensures the status of power exchange between microgrid and main grid to be either purchasing or selling or stay idle. The thermal limit of the tie-line is enforced by constraints (4.18)−(4.19). Equation (4.20) restricts the BESS to be either in charging mode or in discharging mode or stay idle. Constraints (4.21)−(4.22) limit the charging/discharging power of BESS. As shown in (4.23), the SOC level of BESS can be calculated based on current energy stored in BESS. Equation (4.24) calculates the energy stored in the BESS for each time inter-val. The ending SOC level of BESS is forced to be equal to the initial

SOC value (4.25). Constraint (4.26) ensures the microgrid to have sufficient backup power to address outage events.

Objective is shown as,

$$f^{MG} = \sum\sum (P_{Gi}^{t} c_{Gi} + U_{Gi} c_{Gi}^{NL} + V_{Gi} c_{Gi}^{SU}) + P_{Buy}^{t} c_{Buy}^{t} - P_{Sell}^{t} c_{Sell}^{t}, \forall i, t. \quad (4.12)$$

Constraints are as follows:

$$BP_{Buy}^{t} + \sum_{i \in S_G} P_{Gi}^{t} + \sum_{i \in S_{WT}} P_{WTi}^{t} + \sum_{i \in S_{PV}} P_{PVi}^{t} + \sum_{i \in S_S} P_{Disc}^{t,i} = P_{Sell}^{t} + \sum_{i \in S_L} P_{Li}^{t} + \sum_{i \in S_S} P_{Char}^{t,i}, \forall i, t, \quad (4.13)$$

$$P_{Gi}^{Min} \leq P_{Gi}^{t} \leq P_{Gi}^{Max}, \forall i, t, \quad (4.14)$$

$$P_{Gi}^{t+1} - P_{Gi}^{t} \leq \Delta T \cdot P_{Gi}^{Ramp}, \forall i, t, \quad (4.15)$$

$$P_{Gi}^{t} - P_{Gi}^{t+1} \leq \Delta T \cdot P_{Gi}^{Ramp}, \forall i, t, \quad (4.16)$$

$$U_{Buy}^{t} + U_{Sell}^{t} \leq 1, \forall t, \quad (4.17)$$

$$0 \leq P_{Buy}^{t} \leq U_{Buy}^{t} \cdot P_{Grid}^{Max}, \forall t, \quad (4.18)$$

$$0 \leq P_{Sell}^{t} \leq U_{Sell}^{t} \cdot P_{Grid}^{Max}, \forall t, \quad (4.19)$$

$$U_{Disc}^{t,i} + U_{Char}^{t,i} \leq 1, \forall i, t, \quad (4.20)$$

$$U_{Char}^{t,i} \cdot P_{Si}^{Min} \leq P_{Char}^{t,i} \leq U_{Char}^{t,i} \cdot P_{Si}^{Max}, \forall i, t, \quad (4.21)$$

$$U_{Disc}^{t,i} \cdot P_{Si}^{Min} \leq P_{Disc}^{t,i} \leq U_{Disc}^{t,i} \cdot P_{Si}^{Max}, \forall i, t, \quad (4.22)$$

$$SOC_{Si}^{t} = E_{Si}^{t} / E_{Si}^{Max}, \forall i, t, \quad (4.23)$$

$$E_{Si}^{t} - E_{Si}^{t-1} + \Delta T \cdot \left(P_{Disc}^{t-1,i} / \eta_{Si}^{Disc} - P_{Char}^{t-1,i} \eta_{Si}^{Char}\right) = 0, \forall i, t, \quad (4.24)$$

$$E_{Si}^{t=24} = E_{Si}^{Initial}, \forall i, \quad (4.25)$$

$$P_{Grid}^{Max} - P_{Buy}^{t} + P_{Sell}^{t} + \sum_{G \in S_G} (P_{Gi}^{Max} - P_{Gi}^{t}) \geq R_{percent} \left(\sum_{i \in S_L} P_{Li}^{t} \right), \forall i, t. \tag{4.26}$$

When considering battery degradation in microgrid day-ahead scheduling, the objective function needs to be updated by including the associated equivalent battery degradation cost. The updated objective function is shown in (4.27),

$$f = f^{MG} + f^{BESS}, \tag{4.27}$$

where f^{MG} is defined in equation (4.12); and f^{BESS} denotes the battery degradation cost that can be estimated by the proposed NNBD model. f^{BESS} can be calculated as follows,

$$f^{BESS} = \frac{c_{BESS}^{Capital} - c_{BESS}^{SV}}{1 - SOH_{EOL}} BD, \tag{4.28}$$

where $c_{BESS}^{Capital}$ represents the capital investment cost of BESS; c_{BESS}^{SV} denotes the salvage value at the end of life; SOH_{EOL} represents state of health value that the BESS is considered as the end of life; BD represents the percentage battery degradation calculated by (4.11).

Thus, the proposed battery degradation based MDS model can be represented by (4.7)−(4.9), (4.11), and (4.13)−(4.28).

4.4 The Proposed NNODH for Microgrid Scheduling

The proposed battery degradation based microgrid day-ahead scheduling model, which is presented in the above section, would be very hard to solve directly

since the proposed NNBD model that is highly non-linear and non-convex is now a part of the proposed BDMDS model. To address this issue, a novel algorithm, neural network and optimization decoupled heuristic, is proposed in this section to decouple the complex BDMDS model and solve it in the following five steps in an iterative manner. This iterative procedure is illustrated in Fig. 4.12.

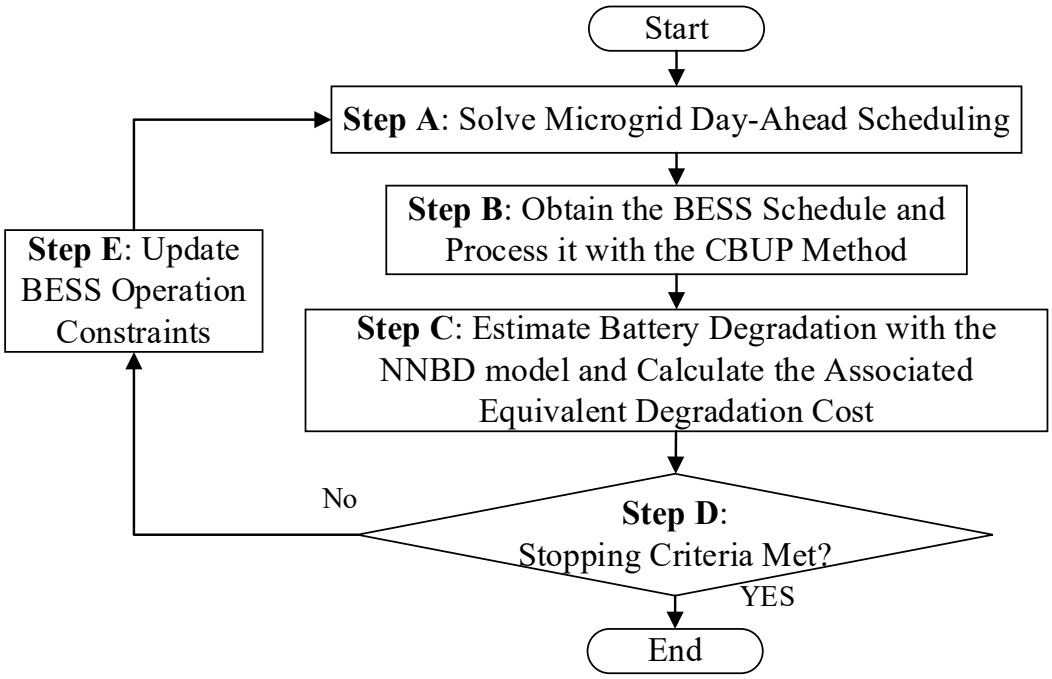

Fig. 4.12. Flowchart of the proposed NNODH algorithm.

- Step A is to solve the microgrid day-ahead scheduling with additional constraints by limiting BESS usage that is generated from Step E. Note that in the first iteration, there is no extra limit on BESS usage.
- Step B obtains the scheduled BESS operating profile that is then processed with the proposed CBUP method.

- Step C estimates BESS degradation with the proposed NNBD model that is trained beforehand and calculates the associated equivalent battery degradation cost.
- Step D determines whether the solutions meet the designed stopping criteria: stop the iteration process and report the solution if yes; otherwise, go to Step E.
- Step E updates the boundaries for the BESS related operating constraints from section 4.4.2 which can limit the BESS operations to reduce the degradation cost; and the associated constraints will be sent to Step A to be included in MDS for the next iteration.

4.4.1 Microgrid Scheduling

The traditional microgrid day-ahead scheduling that introduced in Section II is conducted to obtain an initial solution which does not consider the battery degradation. It is solved only in the first iteration. When considering battery usage limiting constraints that will be presented in Section 4.4.2, Step A will solve the CMDS instead of the traditional MDS. To sum up, traditional MDS is solved in the first iteration while CMDS is solved in all subsequent iterations.

4.4.2 Operation Limits of BESS

The goal of Step E is to generate new constraints that can limit or change the battery output to reduce the total battery degradation. The generated constraints will further tighten the range that BESS can operate after each iteration. Three types of extra constraints are proposed to limit battery output. Constraint (4.29) named as battery consumption limit (BCL) is to reduce the sum of battery output power over 24

hours by forcing it to be less than the previous iteration. Constraint (4.30) only limits the sum of output power in three time intervals that have the highest battery charging or discharging power, named as precise battery consumption limit (PBCL). Constraints (4.31)−(4.32) are designed to limit the maximum charging/discharging power that is named as battery C rate limit (BRL). The proposed constraints will be generated and updated in each iteration by using the scheduled battery operational profile from previous iteration and the proposed battery operation restriction factor (BORF) α which is a preset parameter. Note that the value of BORF can determine the limits in BCL, PBCL, and BRL for each iteration. The limit constraints of BESS are listed as:

$$\sum_{t\in T}(P_{Char}^{t,i}+P_{Disc}^{t,i}) \le (1-\alpha) * P_{BatteryTotal}^{Pervious\_SCUC}, \tag{4.29}$$

$$\sum_{t\in Top\ 3} P_{Disc}^{t,i}+P_{Disc}^{t,} \le (1-\alpha) * P_{BatteryTotal}^{Perviou s_{SCUC}}, \tag{4.30}$$

$$P_{Char}^{t,i} \le P_{Si}^{Max}(1-\alpha)^{iteration-1}, \tag{4.31}$$

$$P_{Disc}^{t,i} \le P_{Si}^{Max}(1-\alpha)^{iteration-1}. \tag{4.32}$$

Depending on which battery usage limiting constraint is used in CMDS, there are four variations of the proposed NNODH algorithm. They are all conducted to compare the performance of the proposed constraints. The proposed four variations are presented in Table 4.4. The CMDS model in this table is solved instead of the traditional MDS model starting from the second iteration of the proposed NNODH algorithm.

Table 4.4 The proposed four NNODH strategies

Strategies	CMDS Model for Step A
NNODH-BCL	(4.12)-(4.26), (4.29)
NNODH-PBCL	(4.12)-(4.26), (4.30)
NNODH-BRL	(4.12)-(4.26), (4.31)-(4.32)
NNODH-ALL	(4.12)-(4.26), (4.29)-(4.32)

4.4.3 NNODH Algorithm

Fig. 4.13 illustrates the iteration process of determining the optimal solution for the battery degradation based MDS using the proposed NNODH algorithm. As is discussed in Section 4.4, the first iteration only considers the traditional microgrid day-ahead scheduling model that ignores the battery degradation. The NNODH algorithm can assure that the solution is guaranteed to reach optimal. The first iteration will provide the optimal solution when the battery degradation is not considered. The BESS operation will be compressed or limited to reduce the battery degradation in the rest of the iterations. During the iterations, the battery degradation will decrease gradually while the operation cost will increase gradually. Thus, the vertex point of the total cost curve is the optimal solution. In Fig. 4.13, the red star denotes the global optimal solution for the battery degradation based MDS that considers the proposed NNBD model; and the black star represents the solution for MDS/CMDS problem in the current iteration while the grey star denotes the solution for the MDS/CMDS problem in the previous iteration. The MDS/CMDS solutions are approximations to the global optimal solution for the battery degradation based MDS; they are referred to

as pseudo solutions (feasible but may not be global optimal) for the battery degradation based MDS. Graph 1 in Fig. 4.13 represents the first iteration. The BESS usage limit constraints that generated in each iteration will reduce the feasible region for the MDS/CMDS problem in the next iteration. Graphs 2-4 show the feasible region shrinks after each iteration and the black star (pseudo solution) is moving towards the red star (global optimal solution for BDMDS). Graph 5 shows the red star and black star overlap which indicates that the black star here is the optimal solution for the BDMDS problem. If the iteration continues, the feasible solution area of BDMDS will continue to reduce such that the optimal solution might be cut out. Since the proposed NNODH algorithm is an iterative method, the α values (BORF) in (4.29)−(4.32) would change over iterations and may result into different BDMDS solutions, among which the best solution should deviate slightly away from the global optimal solution. To ensure the best pseudo solution is close enough to the global solution with least total cost, small α value is preferred. However, it may take more iterations for a smaller α value to find the optimal solution.

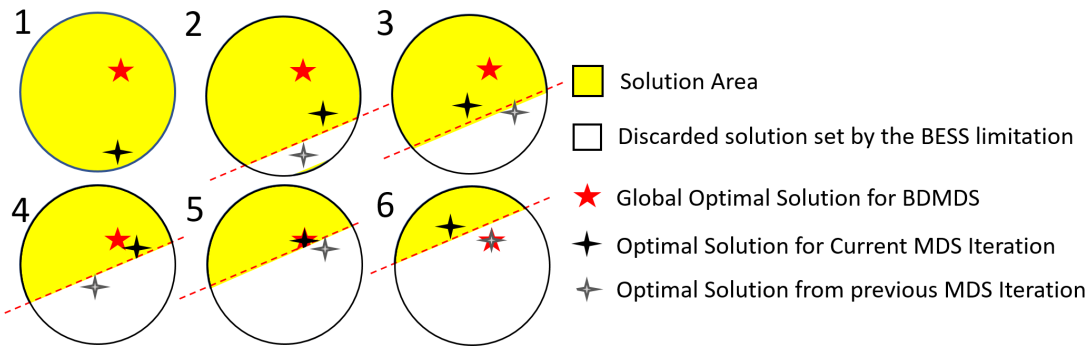

Fig. 4.13. Illustration of the proposed NNODH algorithm.

4.4.4 Evaluation Metrics

Three metrics are designed to evaluate the performance of the proposed model: degradation cost reduction (DCR), total cost reduction (TCR) and operational cost increment (OCI). They are defined in (4.33), (4.34), and (4.35) respectively. The degradation cost reduction illustrates how much the battery degradation cost can be reduced as compared to the maximum value when battery degradation is not considered in traditional MDS. The TCR represents how much the total cost can be reduced by the proposed model while the OCI shows how much the operation cost would increase when considering the battery degradation model. Notations $BDC^{Max}, TC^{Max}, OC^{Min}$ represent the maximum battery degradation cost, maximum total cost, and the minimum operation cost respectively. These metrics are obtained by solving the traditional MDS problem in the first iteration when battery degradation cost is not considered. The proposed metrics are modeled as:

$$DCR = \frac{BDC^{Max} - BDC}{BDC^{Max}} * 100\%, \tag{4.33}$$

$$TCR = \frac{TC^{Max} - TC}{TC^{Max}} * 100\%, \tag{4.34}$$

$$OCI = \frac{OC - OC^{Min}}{OC^{Min}} * 100\%. \tag{4.35}$$

When we consider these proposed metrics to evaluate the proposed algorithm, the TCR will be the first choice since the objective of the algorithm is to reduce the total cost. The algorithm with a higher TCR is always preferred in the analysis. In the meanwhile, the DCR and OCI are designed to gauge the degradation cost and

operation cost. We prefer a higher number of the DCR and a lower number of the OCI. However, DCR and OCI are not as important as the TCR here.

A stopping criterion is proposed as part of the NNODH algorithm. It is used to terminate the iterations and then the best solution can be reported. The designed stopping criteria is defined as follows: for any past 10 iterations, if the $TC^n - TC^{n-1}$ is less than 0 for the first five iterations but greater than 0 for the last five iterations, then the iteration will stop and the best solution with lowest total cost for BDMDS will be reported. Here, TC^n and TC^{n-1} denotes the total costs in n^{th} and $(n\text{-}1)^{\text{th}}$ iterations respectively. The total cost here represents the lowest total cost rather than the lowest battery degradation cost. The optimal solution may be affected by the battery size as well as the unit price.

4.4.5 Benchmark MDS Models

Benchmark models are designed to evaluate and demonstrate the effectiveness and performance of the proposed NNODH algorithm. Three benchmark models are presented below and summarized in Table 4.5.

1. Traditional MDS Model is set with no BESS degradation cost and the MDS will maximize the usage of BESS to minimize the operation cost of the microgrid.
2. Cycle Limit Model is widely adopted in the industry. It is designed to limit the charging and discharging cycles to decrease the degradation of the BESS. This model is formulated with the following constraints where the $V_{Char/Disc}^{t,i}$ is a binary

variable that represents the status change of charging or discharging operation. The formulation are listed as:

$$DV_{Char/Disc}^{t,i} \leq U_{\frac{Char}{Disc}}^{t,i} + U_{\frac{Char}{Disc}}^{t-1,i}, \forall i, t, \tag{4.36}$$

$$V_{Char/Disc}^{t,i} \geq U_{\frac{Char}{Disc}}^{t,i} - U_{\frac{Char}{Disc}}^{t-1,i}, \forall i, t, \tag{4.37}$$

$$V_{Char/Disc}^{t,i} \geq U_{\frac{Char}{Disc}}^{t-1,i} - U_{\frac{Char}{Disc}}^{t,i}, \forall i, t, \tag{4.39}$$

$$V_{Char/Disc}^{t,i} \leq 2 - U_{Char/Disc}^{t,i} - U_{Char/Disc}^{t-1,i}, \forall i, t, \tag{4.40}$$

$$V_{c/disc}^{1} = 0, \tag{4.41}$$

$$\sum_{t} V_{Char/Disc}^{t,i} \leq 2. \tag{4.42}$$

3. Linear Battery Degradation Cost (BDC) Model: The third benchmark model is based on constant battery degradation cost parameters. It is assumed that the battery degradation cost is linear to the energy consumption of the BESS as shown in (39) where the c_{BESS} is a fixed rate that represents the battery degradation cost per unit usage of BESS shown as,

$$f^{BESS} = c_{BESS} \sum_{t,i} P_{Char/Disc}^{t,i} * length(t). \tag{4.43}$$

Table 4.5 Benchmark models

MDS Models	Formulations
Traditional MDS	(4.12)-(4.26)
Cycle Limit	(4.12)-(4.26), (4.36)-(4.42)
Linear BDC	(4.12)-(4.26), (4.43)

4.5 Results Analysis

A typical grid-connected microgrid with renewable energy sources is created in this section as a testbed to examine the performance of the proposed NNBD model, BDMDS model and NNODH algorithm. This testbed includes one 180kW diesel generator (DG), five 200kW wind turbines (WT), 300 residential houses that contains solar panel (5kW capacity per house), and a 300kWh lithium-ion based BESS with a charging/discharging efficiency of 90%. The load data representing 1000 residential houses. The ambient temperature and available solar power for a time period of 24 hours are obtained from the Pecan Street Dataport [22]. The wholesale electricity price is obtained from ECROT [95]. The price of the electricity sold to the main grid is set to 80% of the purchase price. Sensitivity analysis is conducted with different RES penetration levels and different BESS sizes. The computer with Intel® Xeon(R) W-2295 CPU @ 3.0 GHz, 256 GB of RAM, and Nvidia Quadro RTX 8000 (48GB GPU) was utilized to conduct the numerical simulations including the training of battery degradation model and the optimization of microgrid day-ahead scheduling. The microgrid resource scheduling problem studied in this work covers a total time horizon of 24 hours, which is solved by the Pyomo package [96] with the Gurobi solver [97].

4.5.1 Training Results of NNBD

The training results of NNBD and hyperparameters are presented and analyzed in this section. Mini-batch technology is used for the NN training. The optimal batch size may vary for different input data. Different training batch sizes are

tested to determine the optimal training batch-size and the test results are presented in Table 4.6. It can be observed that the batch size of 256 can achieve the highest accuracy while requiring less epochs to complete the training process. The validation accuracy can reach up to 94.5% while it only requires 50 epochs to reach a steady accuracy. The error tolerance is set to 15% when calculating prediction accuracy in Table 4.6 and Table 4.7. Larger or smaller batch size will either reduce the accuracy or increase the training epochs. We found that large batch size can help smooth the oscillation of the training accuracy curve. The training accuracies with batch sizes of 128 and 256 are almost equally the best. However, the training accuracy curve with a batch size of 256 is much smoother than the other one. Moreover, we observed that if the input data are shuffled, then the neural network cannot obtain good results. This may be due to the characteristic of the input data: the battery degradation data are time-series for each battery aging test. The results with different data pre-processing methods are compared in Table 4.7. Note that the test results in Table 4.7 are obtained with the batch-size of 256 for all the trainings. The regressed data pre-processing method has the highest accuracy and efficiency. Based on the results from Table 4.6 and Table 4.7, the regressed method performs the best and is applied for all subsequent simulations.

Table 4.6 Sensitivity test of batch-sizes

Batch-Size	16	32	64	128	256	512	1024	2048
Number of Epochs	20	20	85	110	50	50	75	75
Accuracy	40%	50%	90.5%	94.0%	94.5%	92.5%	88%	67%

Table 4.7 Training results with different data pre-processing methods

Data Pre-processing Methods	Accuracy	Number of Epochs
Raw	78%	150
Smoothed	82%	100
Regressed	94.5%	50

The best training results are shown in Fig. 4.14 that illustrates the training loss versus validation loss and the accuracy curves under different error thresholds. The accuracy is around 60% under a 5% error tolerance, 80% under a 10% error tolerance and 94.5% under a 15% error tolerance. The accuracy with 20% error tolerance is 95.5% which is only 1% higher than the 15% error tolerance. Thus, we choose 15% as the error tolerance level when calculating accuracy in all subsequent results.

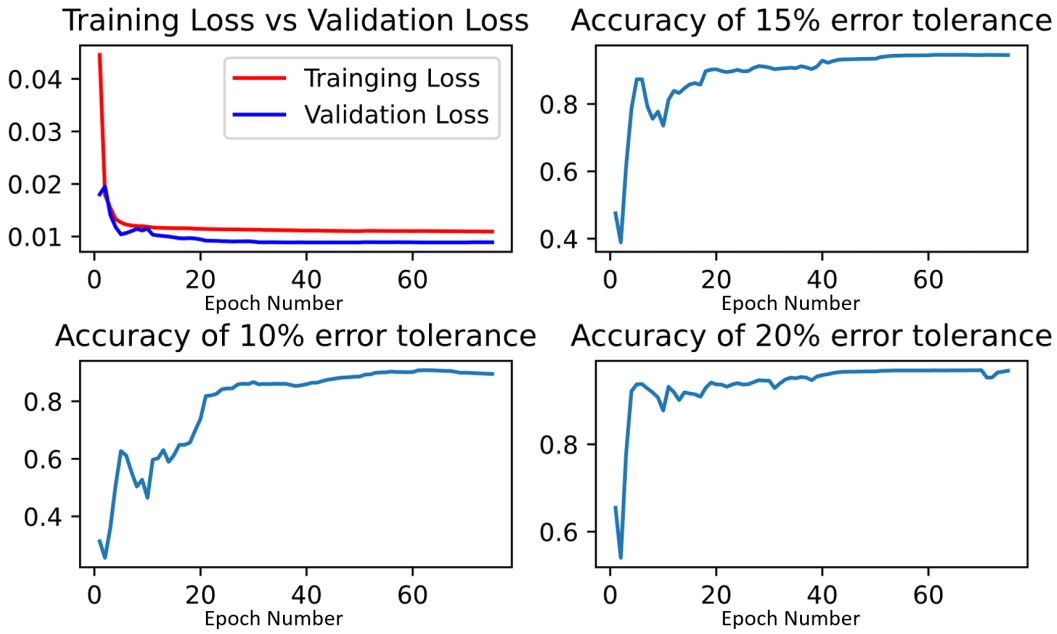

Fig. 4.14. DNN training and validation results.

4.5.2 Results of NNODH Algorithm

In this section, the BDMDS results obtained with the NNODH algorithm are presented. The load profile of the test bed is shown in Fig. 4.15. Table 4.8 presents the results for different strategies of the proposed NNODH algorithm presented in Section IV. The BCL, PBCL, BRL and ALL CMDS models are implemented and tested separately. The combination of all three types of constraints as the added constraints to MDS in the next iteration, marked as ALL in Table 4.8, is tested as well. In Table 4.8, for all the proposed models, the initial iteration does not have any limits of the BESS operation. This also leads to the solution of the first iteration having the highest battery degradation cost. Similarly, the maximum total cost for different models is the same. For metric DCR, the ALL option performs the best among all strategies, and it decreases the battery degradation cost by 79.27%. BCL performs the best in terms of metric TCR. The increased operation cost is similar between BCL and PBCL, which is less than BRL and ALL. Overall, we prefer the NNODH-BCL strategy due to its best performance to decrease the total cost and the fast solving time.

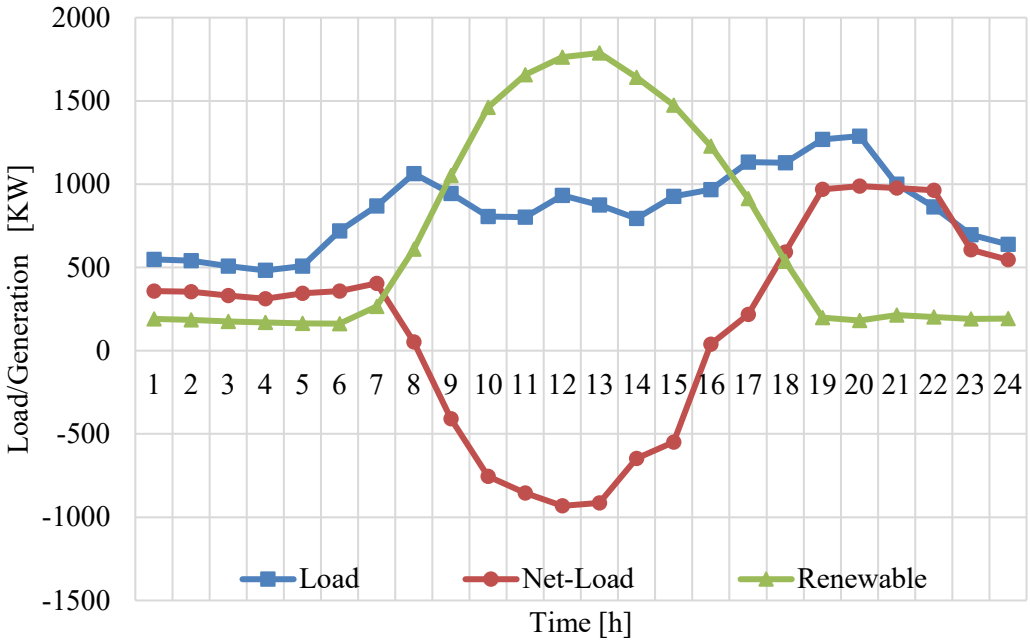

Fig. 4.15. Load profile of the microgrid testbed.

Table 4.8 Results for proposed strategies

NNODH	BCL	PBCL	BRL	ALL
Total Cost ($)	494.36	503.49	502.50	500.32
Degradation Cost ($)	10.74	19.50	11.99	10.39
TCR	5.82%	4.08%	4.27%	4.69%
DCR	78.57%	60.23%	76.08%	79.27%
OCI	1.83%	1.81%	3.20%	3.09%
Solving time (s)	8.68	12.82	10.00	8.48
Iteration Numbers	37	56	46	37

Fig. 4.16 shows the results for NNODH-BCL including the degradation cost, operation cost, battery degradation in percent, and total cost. These results are based on the battery unit price of 400 $/kWh and the value of BORF is set to 0.03. From Fig. 4.16, we can observe that the valley of the total cost curve is at the 37th iteration with

$494.36 including the equivalent battery degradation cost of $10.74 and the microgrid operation cost of $483.62. The total cost is reduced by 5.82% compared to the traditional MDS model that does not consider the battery degradation cost, which proves that the proposed NNODH algorithm can reduce the total cost significantly. Note that the results shown in Fig. 4.16 did not implement the stopping criteria to show how the system behaves when the battery's usage is further limited until idle. If not, the iteration will stop at the 42nd iteration since the minimum total cost can be found at the 37th iteration. After the 37th iteration, we can observe that even though the battery degradation cost keeps decreasing, the total cost starts to increase due to the increased slope of the operation cost.

The scheduled BESS operation for different models are shown in Fig. 4.17. Positive output means the BESS is in discharging mode and negative output means it is in charging mode. The scheduled BESS operations for the Traditional MDS model, Cycle Limit model, Linear BDC model and the proposed BDMDS model are all shown in Fig. 4.17. It can be observed for the traditional MDS that does not consider the battery degradation, BESS operates at a wider output range from -150 kW to 150 kW in seven different time intervals. When battery degradation is considered, BESS is scheduled to charge and discharge in a narrow range and in less active time intervals. The BESS operation patterns for different models match in most of the time intervals, which proves the effectiveness of those four models. For the proposed BDMDS, after applying the NNODH algorithm to solve it, the BESS operates only in three different time intervals. Total exchanged energy is limited to reduce the battery degradation

which meets the designed purpose of constraint BCL. The total usage of BESS for Traditional MDS model is 920 kWh while it is 325 kWh for BDMDS, 601 kWh for Cycle Limit model and 473 kWh for Linear BDC model.

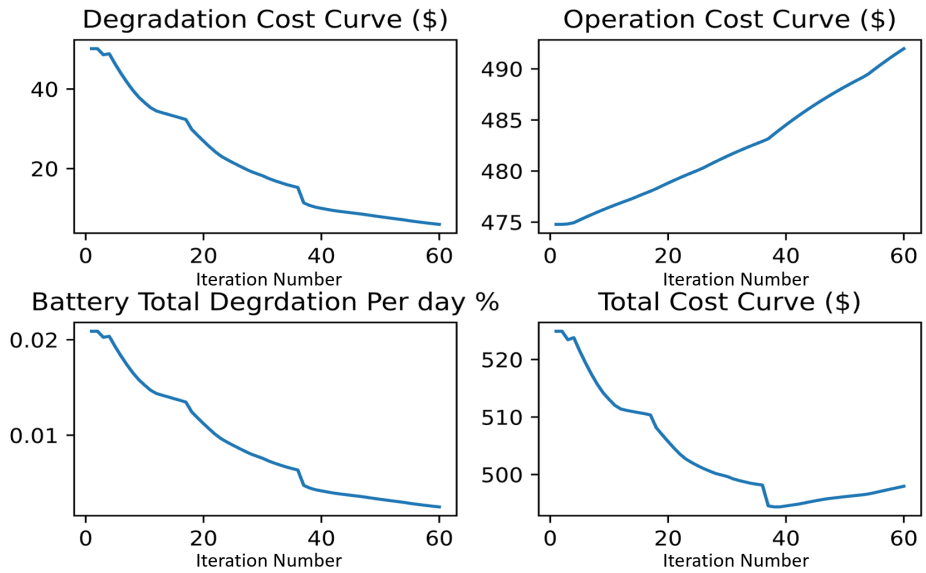

Fig. 4.16. BDMDS Results of the NNODH-BCL method.

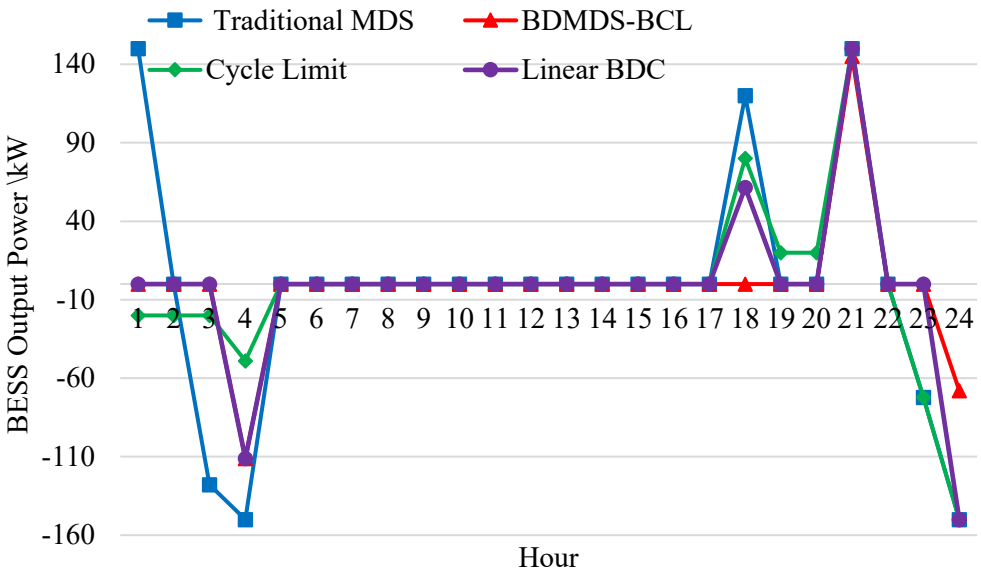

Fig. 4.17. BESS scheduled operations comparison.

Table 4.9 presents the results of the CBUP method applied on the solutions obtained from BDMDS model and traditional MDS model. It can be clearly observed that the battery degradation prediction is pretty close to the true battery degradation in a small percent of error. Without the CBUP method, the error of BD prediction from NNBD model is significantly higher. Thus, the results proves the effectiveness of the proposed CBUP method. From Table 4.10, we can observe that the proposed BDMDS model has the lowest daily degradation and the lowest annual degradation cost among all the models. Moreover, the BDMDS model is outstanding in annual cost saving. Also, if we consider the load profile is the same for each day, then the proposed BDMDS model can significantly extend the lifetime of the BESS than all the benchmark models. Note that the expect end of life is set to 70% of SOH value.

Table 4.11 shows the results of the sensitivity tests with different BORF values. The results show that larger BORF can achieve the lowest total cost in less iterations and less solving time. As a tradeoff, the optimal total cost of larger BORF will be slightly higher. Smaller BORF will lead to a smaller area cut from the feasible solution area in each iteration, which requires more iterations to converge to the optimal solution. However, the optimal solutions for the different BORFs do not have a significant difference. Thus, a higher value of BORF such as 0.05 is preferred due to the high computing efficiency.

Table 4.9 Battery degradation prediction with different methods

Model	True BD	Without CBUP		With CBUP	
		Degradation	Error	Degradation	Error
BDMDS	0.00468%	0.037%	690%	0.0044%	5.9%
MDS	0.0108%	0.066%	511%	0.0120%	9.7%

Table 4.10 Model comparison

Model	Daily BESS Degradation	Annual Degradation Cost ($)	Annual Cost Saving ($)	Expect Lifetime (years)
MDS	0.02%	18,301.1	N/A	4.1
Cycle Limit	0.012%	12,540.8	6,205	6.8
Linear BDC	0.01%	8,832.5	6,935	8.2
BDMDS	0.0045%	3,920.1	11,151	18.3

Table 4.11 Results of sensitivity analysis with different BORF values

BORF	Number of Iterations	Optimal Total Cost ($)	Time (s)
0.01	113	494.35	25.21
0.02	57	494.35	12.51
0.03	38	494.36	8.42
0.05	22	494.36	5.20
0.1	11	494.38	2.85
0.2	5	494.40	1.41

4.5.3 Sensitivity Analysis of RES Penetration Levels

Table 4.12 presents the TCR and OCI results under different RES penetration levels for the microgrid. The penetration level is defined as the ratio of the average renewable generation to the average load in a typical day. The proposed microgrid testbed is set to an 80% RES penetration level. From Table 4.12, we can observe that with the increase of RES penetration level, the value of TCR will increase and the value of OCI will decrease. This is because that in a system with higher RES penetration, BESS is required to charge/discharge more frequently to mitigate the uncertainty resulted by the RES generation, which leads to a higher battery degradation.

Table 4.12 Results of different RES penetration levels

	RES Penetration Level			
	20%	40%	60%	80%
TCR	1.60%	2.1%	3.12%	5.82%
OCI	0.47%	0.63%	0.94%	1.83%

4.5.4 Sensitivity Analysis of BESS Unit Price and Size

In this section, the sensitivity analysis on different BESS unit prices and sizes is conducted. Fig. 4.18 shows that the total cost reduction in percentage. It can be clearly observed that for the same size of BESS, higher unit price corresponds to a higher total cost reduction in percent. For the same unit price of BESS, higher BESS size tends to achieve a lower TCR. Table 4.13 shows that for the same unit price except $200/kWh, higher BESS size has a lower DCR. This may be because that for the same battery output power, bigger battery size will likely have a lower C rate which is one of the main contributing factors of battery degradation. Also, for the same size BESS, higher unit price leads to a higher DCR. Thus, we can conclude that the BESS price of per unit capacity is the major factor affecting how much the proposed model reduces the degradation cost. The BESS size is the major factor affecting how much the proposed model reduces the battery degradation. The result of the sensitivity analysis in this section may help determine the size of the BESS for microgrid planning. In the meanwhile, as the unit price of BESS keeps decreasing, the battery degradation cost will be lower and account for smaller percentage respect to the total cost in the future.

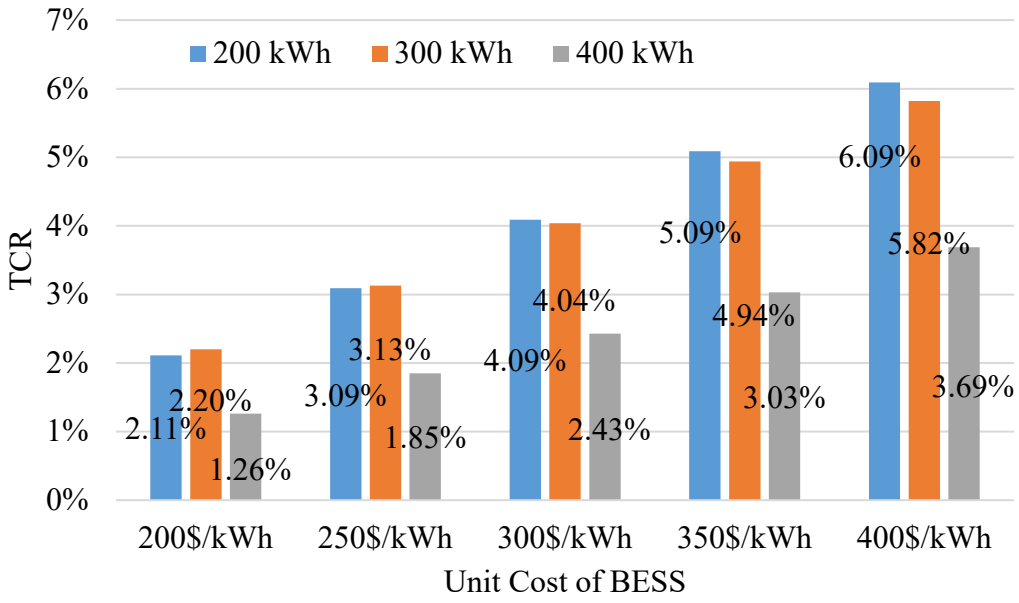

Fig. 4.18. Results of TCR sensitivity tests.

Table 4.13 DCR of different BESS sizes and unit prices

	Unit Price ($/kWh)				
Size (kWh)	200	250	300	350	400
200	75.15%	82.16%	82.96%	85.18%	88.58%
300	77.29%	77.29%	78.57%	78.57%	78.57%
400	52.95%	54.48%	54%	71.90%	72.68%

4.6 Hierarchical Deep Learning Model

A fully connected neural network (NN) based battery degradation model and an iterative solving algorithm are proposed in previous section. This model works well under different scenarios and have an accuracy of 94.5% on the degradation prediction at a 15% error tolerance. However, the input of the NN only consist the ambient temperature, charging/discharging rate, SOC, DOD and SOH. The internal features such as internal temperature and internal resistance that are more likely to affect the

battery degradation are ignored in the previous NN model. To overcome this limitation, a hierarchical deep learning based battery degradation quantification (HDL-BDQ) model is proposed as shown in the left part in Fig. 4.19. The proposed HDL-BDQ model aims to improve the training accuracy of the battery degradation by utilizing two sequential deep neural networks (DNN) which are DNN for unobtainable battery degradation features (DNN-UBDF) and DNN for battery degradation prediction (DNN-BDP). The DNN-UBDF predicts critical battery degradation features that are difficult to obtain for look ahead scheduling (LAS), which are then used as input features for the DNN-BDP to quantify the corresponding battery degradation per scheduled usage profile.

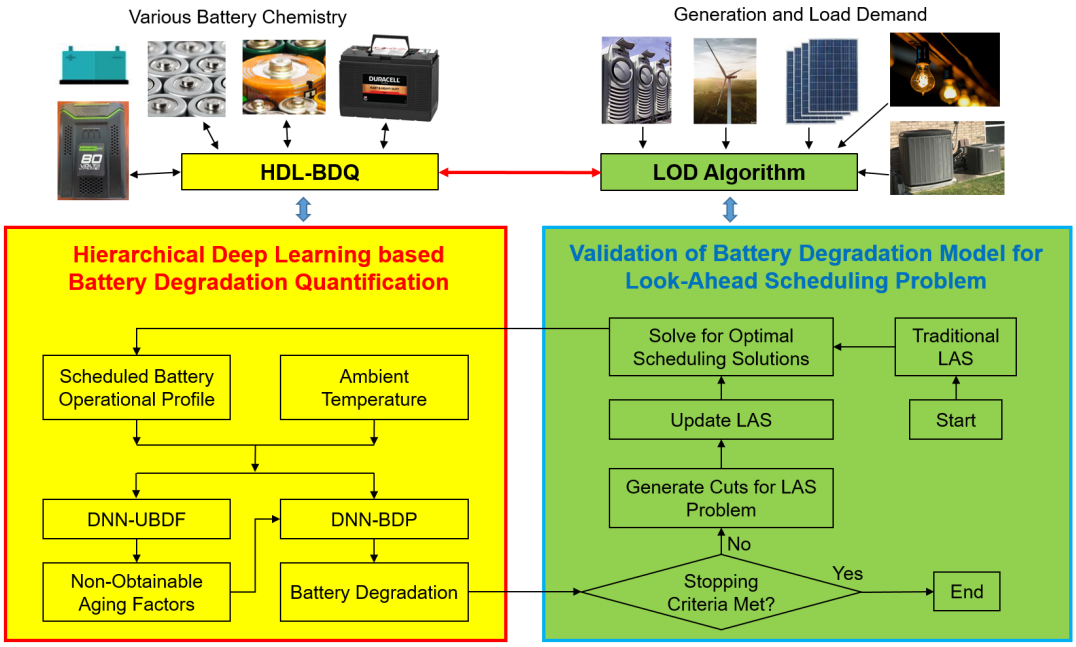

Fig. 4.19. HDL-BDQ and LOD algorithm.

The HDL-BDQ models are designed to quantify the battery degradation. However, a DNN embedded LAS problem would be hard to solve directly due to the

highly non-linear and non-convex nature of the DNN model. To address this challenge, a learning and optimization decoupled (LOD) algorithm is implemented to efficiently solve the proposed HDL-BDQ embedded LAS optimization problem. As shown in the right part of Fig. 4.18, the LOD algorithm iteratively solves the HDL-BDQ model embedded LAS that is decoupled to the battery degradation calculation and LAS optimization problems. In each iteration of LOD algorithm, tighter constraints will be updated on BESS operation to restrict its usage and lower the battery degradation and associated costs in the next iteration. However, limiting BESS output will result in a higher microgrid operation cost. The objective of the proposed LOD algorithm is to find the minimum combined cost of battery degradation and microgrid operation. The algorithm also keeps track of the total cost in each iteration and finds the optimal solution for the HDL-BDQ embedded LAS problem at the vertex point. Thus, an optimal solution is guaranteed with respect to the vertex point of the combined total cost.

4.6.1 HDL-BDQ Model

The proposed HDL-BDQ model utilizes two sequential deep neural networks to adaptively quantify the battery degradation associated with the scheduled battery operational profiles over multiple time intervals. Several factors affect battery degradation during a (dis)charge cycle, as listed in Table 4.14 including (i) ambient temperature (Temp), (ii) current battery energy capacity or SOH, (iii) SOC level, (iv) DOD level, (v) (dis)charge rate (C Rate), (vi) battery internal temperature (IT), (vii) battery internal resistance and (viii) equivalent life cycle numbers (ELCN) which

varies per other degradation features. However, battery internal temperature, battery internal resistance and equivalent life cycle numbers cannot be obtained explicitly in advance. To address this issue, we have developed a DNN-UBDF model that uses the first five features to predict these unknown factors. Subsequently, the output of DNN-UBDF model, along with the other features, will be used as inputs to the trained DNN-BDP model to predict and quantify battery degradation. By comparing the training results of the proposed DNN models, we can identify the most efficient and accurate combination for the proposed HDL-BDQ model.

Table 4.14 Battery degradation factors

Features	Existing or Obtainable
State of Charge	Yes
Depth of Discharge	Yes
Ambient Temperature	Yes
Charge/Discharge Rate	Yes
Current Capacity	Yes
Internal Temperature	No
Internal Resistance	No
Equivalent Life Cycle Numbers	No

The HDL-BDQ proposed in this section consists of two deep neural networks: the first DNN model (DNN-UBDF) will predict the battery internal parameters that cannot be calculated or measured directly per the scheduled battery operational profile in advance. The outputs of DNN-UBDF, which are the predicted battery parameters, will then be used as additional input features for DNN-BDP, along with the scheduled battery operational profile, to quantify the corresponding battery degradation in the same look-ahead time period.

As mentioned in the introduction section above, some highly influential battery degradation factors such as battery internal temperature and internal resistance are hard to predict or measure in the look-ahead scheduling. Thus, DNN-UBDF is proposed to capture the non-linearity between the available variables and unknown features that are highly correlated with battery degradation. IT, IR and LCN are hard to measure or calculate based on the available information as shown in Table 4.14 To address this issue, several potential DNN models are proposed and listed in Table 4.15 DNN-UBDF is modeled using a fully connected neural network. The deep neural network takes five critical factors (ambient temperature, C rate, SOC, DOD, and SOH) as inputs to predict the value of IT, IR and/or ELCN. A dynamic learning rate, which decreases automatically after a specified number of epochs, is employed during the training process to enhance the results. The trained network has a 5-neuron input layer, 20-neuron first hidden layer, and a 10-neuron second hidden layer. The number of the output neurons depends on the number of outputs in the proposed model in Table II. The activation functions used are rectified linear unit (ReLU) for the hidden layers and "linear" for the output layer.

Table 4.15 Potential models for DNN-UBDF

Model #	Inputs	Outputs
1	SOC, DOD, Temp, C Rate, SOH	IT
2	SOC, DOD, Temp, C Rate, SOH	IR
3	SOC, DOD, Temp, C Rate, SOH	IT, IR
4	SOC, DOD, Temp, C Rate, SOH	IT, ELCN
5	SOC, DOD, Temp, C Rate, SOH	IR, ELCN
6	SOC, DOD, Temp, C Rate, SOH	IT, IR, ELCN

DNN-BDP is proposed to predict the battery degradation value with the inputs of major battery degradation factors, including the outputs of DNN-UBDF. As these factors are highly correlated to battery degradation, including them as inputs can significantly improve the training results. Similar to DNN-UBDF, we proposed several potential DNN models for DNN-BDP as shown in Table III: several different combinations of critical battery degradation factors are utilized separately to predict the battery degradation value in terms of percentage with respect to SOH for a given cycle. The structure of DNN-BDP models is similar to the model of DNN-UBDF. The number of input neurons depends on the number of input features of the proposed DNN-BDP models as listed in Table 4.16.

Table 4.16 Potential models for DNN-BDP

Model #	Inputs	Outputs
1	IT, ELCN	Degradation
2	IR, ELCN	Degradation
3	SOC, DOD, Temp, C Rate, IT	Degradation
4	SOC, DOD, Temp, C Rate, IR	Degradation
5	SOC, DOD, Temp, C Rate, IT, ELCN	Degradation
6	SOC, DOD, Temp, C Rate, IR, ELCN	Degradation
7	SOC, DOD, Temp, C Rate, IT, SOH	Degradation
8	SOC, DOD, Temp, C Rate, IR, SOH	Degradation
9	SOC, DOD, Temp, C Rate, IT, SOH, ELCN	Degradation
10	SOC, DOD, Temp, C Rate, IR, SOH, ELCN	Degradation

4.6.2 Benchmark Models

A. Benchmark NNBD:

The neural network based battery degradation (NNBD) model that uses SOC, DOD, C rate, temperature and SOH as the inputs to predict the battery degradation is

served as the benchmark model for this section. As discussed in the introduction section, the accuracy of this model is 94.5% with an error tolerance of 15%. It is worth mentioning that its training dataset was preprocessed in addition to normalization to obtain this accuracy.

B. Benchmark NNBD2:

Another benchmark is proposed with an extra hidden layer included into the first benchmark model. Since the proposed HDL-BDQ model utilizes two DNNs to predict the battery degradation. It is possible that a single stage DNN model with extra hidden layer as shown in Fig. 4.20 may also achieve similar performance.

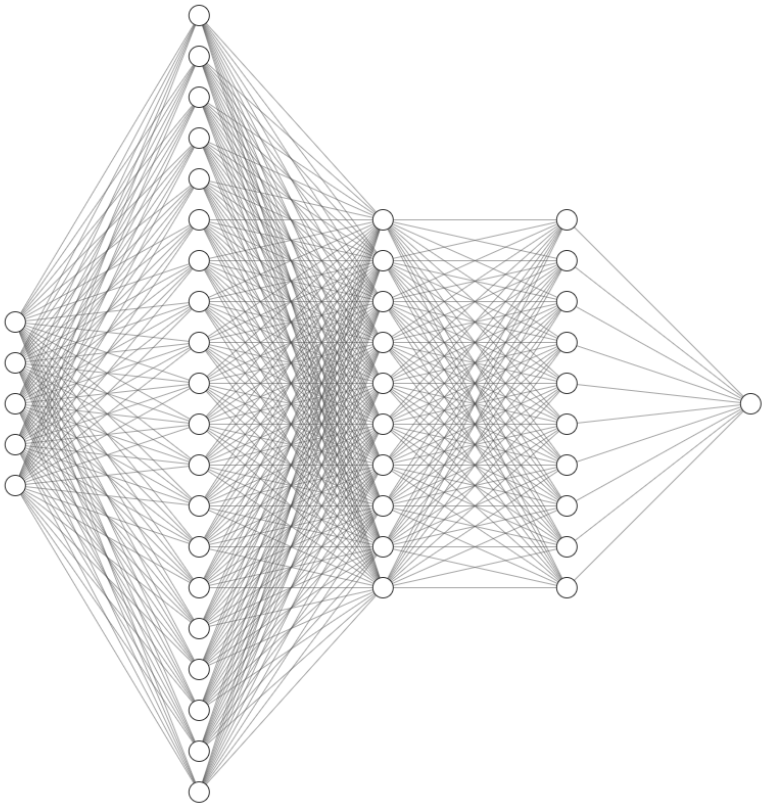

Fig. 4.20. Structure of the proposed Benchmark 2 model [94].

4.6.3 DNN-UBDF Training Results

The training results of proposed DNN-UBDF models are presented in Table IV. From this table, we can observe that the training accuracies are similar at 15% error tolerance level between DNN-UBDF Model 1 and Model 2, as well as Model 4 and Model 5. However, the accuracies of the various models vary at different error tolerance levels. For instance, while DNN-UBDF Model 1 outperforms Model 5 at the 10% error tolerance level, Model 5 surpasses Model 1 at the 15% tolerance level. The main objective is to have a high training accuracy HDL-BDQ model in this section. Thus, the selection of DNN-UBDF is based on the performance of the proposed DNN-BDP models. DNN-BDP can determine the inputs that lead to the highest accuracy of the ultimate battery prediction model.

Table 4.17 Training results of proposed models for DNN-UBDF

Error Tolerance	5%	10%	15%	20%
DNN-UBDF Model 1	45.25%	77.33%	88.63%	89.74%
DNN-UBDF Model 2	48.66%	78.37%	89.21%	90.59%
DNN-UBDF Model 3	37.96%	69.14%	85.47%	87.19%
DNN-UBDF Model 4	48.82%	73.86%	88.58%	91.23%
DNN-UBDF Model 5	51.05%	75.12%	89.90%	90.11%
DNN-UBDF Model 6	39.78%	65.61%	81.31%	83.74%

4.6.4 DNN-BDP Training Results

Based on the results shown in Table 4.18, it is evident that the DNN-BDP Model 10 outperforms all other models across the tolerance levels. Thus, it can be concluded that, given the training dataset, Model 10 which takes SOC, DOD, Temp, C Rate, IR, Cap and ELCN as inputs, is the best model for DNN-BDP in battery degradation prediction. Model 10 includes the most input features among the models

besides Model 9. Model 1 and Model 2 are the simplest model that consists only two input features and perform well, but the accuracy at 5% tolerance level is low comparing to Model 10. Conversely, Model 7 and Model 8 yield very low prediction accuracy. Interestingly, the prediction accuracy of Model 3 and Model 4 are quite high. The only difference is the SOH is added in the input features for Model 7 and Model 8. Moreover, when we compare Model 8 and Model 10, the huge accuracy difference shows the importance of ELCN in battery degradation prediction. Further analysis shows that even-numbered models, which include IR as an input variable, perform better than odd-numbered models, which include IT. This suggests that IR is a better indicator of degradation than IT, at least on the dataset that has been examined in this work. Fig. 4.21 shows the results in the training process of the Model 10 that becomes stable after 200 epochs.

Table 4.18 Training results of proposed models for DNN-BDP

Error Tolerance	5%	10%	15%	20%
DNN-BDP Model 1	45.30%	77.57%	93.94%	97.89%
DNN-BDP Model 2	48.80%	82.16%	97.23%	99.89%
DNN-BDP Model 3	48.76%	82.04%	97.41%	99.91%
DNN-BDP Model 4	50.82%	79.37%	94.20%	99.91%
DNN-BDP Model 5	34.38%	65.57%	86.15%	95.91%
DNN-BDP Model 6	25.99%	59.11%	88.12%	97.76%
DNN-BDP Model 7	15.67%	21.66%	30.81%	45.85%
DNN-BDP Model 8	12.17%	18.85%	23.66%	30.82%
DNN-BDP Model 9	56.39%	88.87%	96.67%	97.07%
DNN-BDP Model 10	58.36%	91.56%	99.36%	99.99%

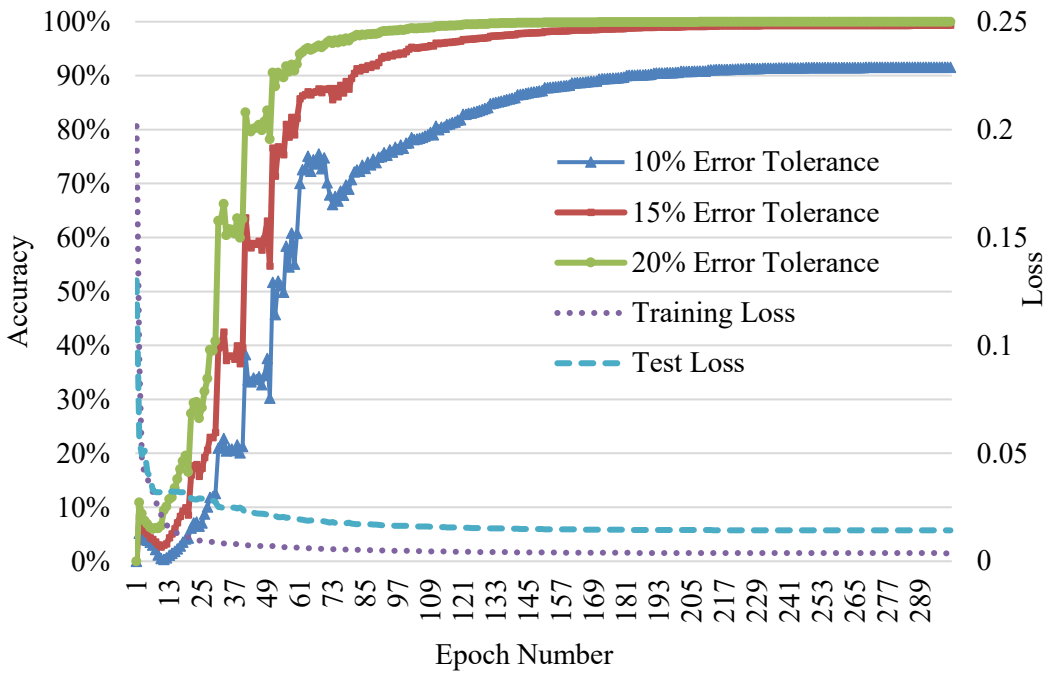

Fig. 4.21. Training result of Model 10 for DNN-BDP.

4.6.5 Overall Performance of HDL-BDQ Model

Since the superior performance of Model 10 for DNN-BDP, we have selected Model 5 from DNN-UBDF and Model 10 from DNN-BDP as the two sequential DNN models for the proposed HDL-BDQ model. The overall performance of HDL-BDQ model is evaluated by connecting DNN-UBDF and DNN-BDP together. Table 4.19 present the overall performance of the HDL-BDQ model and the benchmark models. At the 15% error tolerance level, the proposed HDL-BDQ model achieves an accuracy of 91.7%, whereas the NNBD model only attains 83.1%. It is evident that the proposed HDL-BDQ model can outperform the benchmark models completely across all tolerance levels. The proposed HDL-BDQ model achieves a high accuracy especially when the tolerance is in 5% and 10%. Note that the results for three models

shown in Table 4.19 are based on the same training dataset that do not undergo any filtering or pre-processing.

Table 4.19 Performance Comparison of Battery Degradation Prediction

Error Tolerance	5%	10%	15%	20%
HDL-BDQ	37.4%	73.4%	91.7%	97.3%
NNBD	31.4%	57.0%	83.1%	97.3%
NNBD2	27.3%	55.6%	79.2%	91.4%

4.7 Summary

In this chapter, a neural network based battery degradation model is introduced to predict the BESS degradation value for each scheduling period. A cycle based battery usage processing method is designed to accurately apply the proposed NNBD model with the microgrid day-ahead scheduling model. The NNODH algorithm is proposed to decouple the battery degradation based microgrid day-ahead scheduling problem that is hard to solve directly due to the highly non-linear characteristic of the proposed NNBD model. The proposed NNODH algorithm can solve the MDS optimization problem and calculate the battery degradation cost iteratively and effectively find the optimal solution with the lowest total cost. The CMDS problem is created with the options of using different proposed constraints to limit the BESS usage and obtain a lower battery degradation cost. An RES-enriched microgrid is used to evaluate the performance of the proposed BDMDS model and the proposed NNODH algorithm.

The test results demonstrate that the battery degradation can be accurately predicted (5.9% error) by the proposed NNBD model with the adjusted inputs

obtained by the proposed CBUP method. The proposed NNODH algorithm can obtain the optimal solution efficiently. Compared with the traditional MDS models, the total cost can be reduced significantly by 5.82% with the proposed BDMDS model. Also, the proposed model can reduce the daily BESS degradation significantly from 0.02% to 0.0045%. The annual degradation cost is reduced by 78.6% with the proposed model. Moreover, the expected lifetime is extended from 4.1 years to 18.3 years with the proposed model. The NNODH-BCL performs the best among the proposed four strategies in this case. Sensitivity tests demonstrate the performance of the proposed NNODH algorithm under different BESS sizes and unit prices. Overall, this work demonstrates the effectiveness of the proposed BDMDS model for reducing battery degradation cost and total cost, and the capability of the proposed NNODH algorithm for efficiently solving BDMDS that is a deep neural network embedded optimization problem.

Also, a hierarchical deep learning-based battery degradation quantification model is proposed to predict the BESS degradation value for each scheduling period. Multiple potential DNN models are proposed and tested separately to determine the most accurate and efficient combination of the HDL-BDQ model (DNN-UBDF and DNN-BDP). The simulation results demonstrate that the proposed HDL-BDQ is more advanced than the single stage NNBD model since it requires less training data and achieves higher training accuracy (91.7% versus 83.1% & 79.2%, with an error tolerance of 15%). The proposed various potential models for the two sequential DNN

models also help determine that the IR and ELCN are the most correlated battery degradation parameters at least for the dataset used in this work.

5. PIECEWISE LINEARIZED BATTERY DEGRADATION BASED ENERGY SCHEDULING MODEL

5.1 Literature Review

A number of previous studies have developed various battery degradation models for BESS. A piecewise linear battery degradation model that is based on Arrhenius law is proposed in [53] to predict battery degradation. However, this degradation model only reflects the impact of depth of discharge (DOD), which is not sufficient. Similarly, the battery degradation in [71] is calculated based on the remaining useful life (RUL) of BESS that is predicted by the DOD of each cycle. It is not reasonable to consider the linear relationship between DOD and RUL throughout the lifetime of BESS. Moreover, the RUL is affected by several other degradation factors besides the DOD. A linear degradation rate is applied to quantify the battery degradation cost in the optimization problem [73]−[75]. The linear degradation may decrease the difficulty of solving the unit commitment problem, but the inaccurate degradation information of the linear model may substantially reduce the lifetime of the BESS. For all the aforementioned battery degradation models, they either consider a linear degradation cost or the models missing several critical degradation factors such as state of charge (SOC), C rate, and ambient temperature; none of them developed a comprehensive model to cover the majority critical degradation factors.

A neural network based battery degradation (NNBD) is developed in [98]. Although the NNBD model can accurately predict the battery degradation with major degradation factors (SOC, DOD, C rate, state of health (SOH) and ambient

temperature), the proposed iterative method seems to only address systems with only one BESS integrated bus and cannot scale to large-scale systems.

To bridge the aforementioned gaps, this chapter proposes a novel security-constrained unit commitment model with linearized neural network based battery degradation model, referred to as linearized battery degradation model based SCUC (Linearized BD-SCUC or L-BD-SCUC). The proposed L-BD-SCUC model that considers the equivalent battery degradation cost is directly solvable. The NNBD model is structured to learn and predict the value of battery degradation with major degradation factors. The non-linear activation function for each neuron in each hidden layer is linearized to enable a linearized NNBD model. As a result, L-BD-SCUC can be solved directly to provide the optimal solution with the lowest total cost that is the sum of the operation cost and the equivalent battery degradation cost.

5.2 Traditional SCUC Model

A traditional SCUC (T-SCUC) model is established as a benchmark model to gauge the proposed L-BD-SCUC model. This T-SCUC model consists of (5.1)-(5.18) as described below and it does not consider equivalent degradation cost of BESS. The cost of BESS degradation will be presented in next section. The objective of the T-SCUC model is to minimize the total operation cost of the generators which is shown below,

$$f(\text{cost}) = f^G, \tag{5.1}$$

where f^G denotes the total cost of all the generator units that are shown below,

$$f^G = \sum_{t\in S_T}\sum_{g\in S_G} P_g^t c_g + U_g^t c_g^{NL} + V_g^t c_g^{SU}. \quad (5.2)$$

The nodal power balance equation involving synchronous generators, renewable energy sources, BESSs and demand of bus n is shown in (5.3). Constraints (5.4)−(5.6) represent the power output limits and ramping limits of each generators. Equations (5.7) − (5.9) define the relation between generator start-up status and generator on/off status. The thermal limit of the transmission line is enforced by (5.10). Constraint (5.11) represents the network power flow equation. As shown in (12), the SOC level can be represented by the ratio between the current stored energy and maximum available energy capacity. Constraints (5.13) − (5.14) enforce the charging/discharging power limits of BESS. Constraint (5.15) restricts the BESS to be either in charging mode or in discharging mode or stay idle. Equation (5.16) calculates the stored energy of BESS at each time interval. The ending BESS SOC level is forced to equal the initial value in (5.17). Equation (5.18) enforces the limit of the stored energy for BESS. The T-SCUC model is listed as:

$$\sum_{g\in S_G} P_g^t + \sum_{r\in S_R} P_r^t + \sum_{k\in K(n-)} P_k^t + \sum_{s\in S_S} P_{Disc}^{t,s} = \sum_{k\in K(n+)} P_k^t + \sum_{d\in S_L} P_d^t + \sum_{s\in S_S} P_{Char}^{t,s}, \forall n, t, \quad (5.3)$$

$$P_g^{Min} U_g^t \le P_g^t \le P_g^{Max} U_g^t, \forall g, t, \quad (5.4)$$

$$P_g^{t+1} - P_g^t \le \Delta T \cdot P_g^{Ramp}, \forall g, t, \quad (5.5)$$

$$P_g^t - P_g^{t+1} \le \Delta T \cdot P_g^{Ramp}, \forall g, t, \quad (5.6)$$

$$V_g^t \ge U_g^t - U_g^{t-1}, \forall g, t, \quad (5.7)$$

$$V_g^{t+1} \le 1 - U_g^t, \forall g, t, \quad (5.8)$$

$$V_g^t \le U_g^t, \forall g, t, \tag{5.9}$$

$$-P_k^{Max} \le P_k^t \le P_k^{Max} \ , \forall k, t, \tag{5.10}$$

$$P_k^t - b_k(\theta_n^t - \theta_m^t) = 0 \ , \forall k, t, \tag{5.11}$$

$$SOC_s^t = E_s^t / E_s^{Max} \ , \forall s, t, \tag{5.12}$$

$$U_{Char}^{t,s} P_s^{Min} \le P_{Char}^{t,s} \le U_{Char}^{t,s} P_s^{Max}, \forall s, t, \tag{5.13}$$

$$U_{Disc}^{t,s} P_s^{Min} \le P_{Disc}^{t,s} \le U_{Disc}^{t,s} P_s^{Max}, \forall s, t, \tag{5.14}$$

$$U_{Disc}^{t,s} + U_{Char}^{t,s} \le 1, \forall s, t, \tag{5.15}$$

$$E_s^t - E_s^{t-1} + \Delta T \cdot \left(P_{Disc}^{t-1,s} / \eta_s^{Disc} - P_{Char}^{t-1,s} \eta_s^{Char} \right) = 0, \forall s, t, \tag{5.16}$$

$$E_s^{t=24} = E_s^{Initial} \ (i \in \ S_S), \forall s, t, \tag{5.17}$$

$$E_s^{Min} \le E_s^t \le E_s^{Max}, \forall s, t. \tag{5.18}$$

5.3 Linearization of NNBD model

Since the iteration method developed in chapter 4 for solving BD-SCUC is limited to single-BESS systems, an alternative method L-BD-SCUC is proposed in this section to linearize the NNBD model and make the BD-SCUC directly solvable. The proposed L-BD-SCUC model consists of (4.7)−(4.9), (4.11), and (5.3)−(5.19) and (5.21)−(5.24).

The NNBD model can be expressed by a set of equations that represent neuron's calculation and activation. Equation (5.19) represents the calculation for each neuron that involves the input features from the first layer, corresponding weights matrix W and the biases matrix. The non-linear ReLU activation function is

represented in (5.20) which is linearized with an auxiliary variable δ_h^i by (5.21)−(5.24). Note that δ_h^i is a binary variable: one indicates activation is enabled and zero otherwise. a_h^i represents the activated value of x_h^i. The linearized ReLU formulation as listed as:

$$x_h^i = \sum x_{h-1}^i * W + Bias, \tag{5.19}$$

$$a_h^i = relu\left(x_h^i\right) = ma\,x\left(0, x_h^i\right), \tag{5.20}$$

$$a_h^i \le x_h^i + BigM * \left(1 - \delta_h^i\right), \tag{5.21}$$

$$a_h^i \ge x_h^i, \tag{5.22}$$

$$a_h^i \le BigM * \delta_h^i, \tag{5.23}$$

$$a_h^i \ge 0. \tag{5.24}$$

5.4 Multi-BESS Test Case

A typical IEEE 24-bus system [99] that has 33 generators is used as a test bed to evaluate the proposed L-BD-SCUC method in this section. Fig. 5.1 illustrates the IEEE 24-bus system. The benchmark model T-SCUC does not consider the battery degradation. The L-BD-SCUC model and the T-SCUC model are solved by the python package “Pyomo” [96] and “Gurobi” optimizer solver [97].

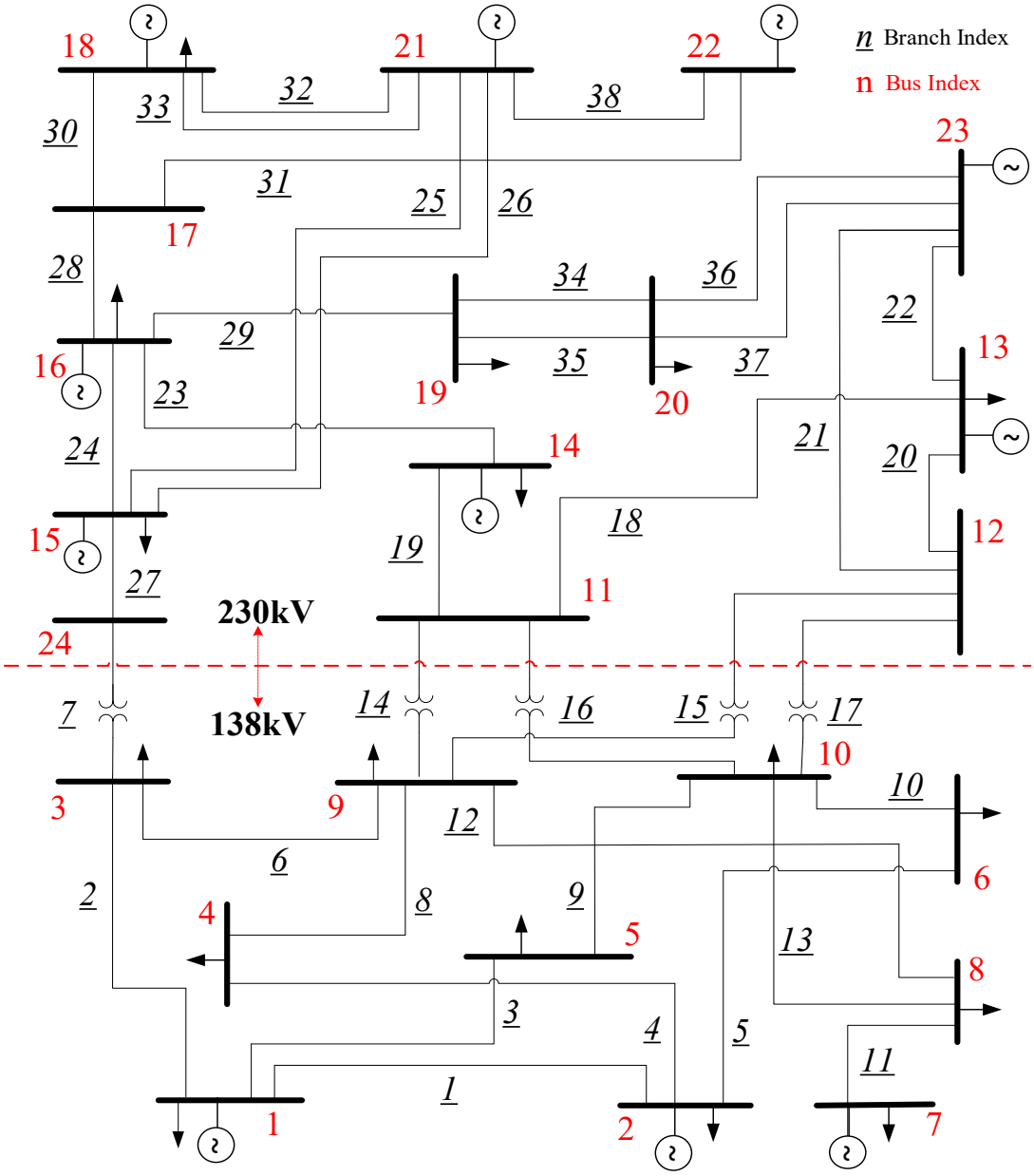

Fig. 5.1. IEEE 24-bus system [99].

5.5 Results Analysis

A verification test is first conducted by solving SCUC for a single BESS integrated system to demonstrate the proposed L-BD-SCUC model against the BD-SCUC model.

The BESS schedule profile that obtained from the result of L-BD-SCUC model is fed into the NNBD model to calculate the battery degradation and its equivalent cost. From the results, the battery degradation cost obtained from the trained NNBD model is \$14,289.50, while it is \$14,289.49 reported directly from the L-BD-SCUC model. The degradation cost between the two models are negligible, which verifies the effectiveness of the proposed linearization model. This is actually expected since the piecewise linearization with an auxiliary binary variable is an exact reformulation of activation function ReLU.

Table 5.1 presents the parameters of BESSs that are installed at different buses in the IEEE 24-bus system. The energy capacities of different BESSs are different. The BESS numbered four has the largest energy capacity and the highest output power among all five BESSs. Table 5.2 presents the wind farms that are integrated in the IEEE 24-bus system. There are five wind farms and each contains different numbers of wind turbines. The capacity for each wind turbine is 200 kW. The wind profile data originally from Pecan Street Dataport [22] are scaled for this study.

Table 5.1 BESS parameters.

BESS *No*.	Bus *No*.	Capacity (MWh)	*P_Max* (MW)	*P_Min* (MW)	Price \$/MWh	Initial SOC
1	21	50	20	0	100,000	40%
2	22	10	4	0	120,000	40%
3	7	10	4	0	120,000	40%
4	14	200	100	0	75,000	40%
5	9	30	10	0	110,000	50%

Table 5.2 Wind farm locations and sizes.

Wind Farm *No*.	Wind Farm Bus	# of Wind Turbines
1	21	200
2	22	80
3	2	100
4	14	100
5	15	100

Table 5.3 compares the results from T-SCUC and L-BD-SCUC. The total cost represents the summation of generators' fuel cost and the equivalent battery degradation cost. Since the T-SCUC model does not consider the battery degradation, the equivalent battery degradation cost for T-SCUC in Table 5.2 is obtained by collecting the BESS output results from T-SCUC and feed it into the NNBD model. In other words, the battery degradation cost is calculated independently after the T-SCUC is solved while it is directly considered and solved in the L-BD-SCUC model. The results meet the expectation that there will be a total cost reduction achieved by the proposed L-BD-SCUC model. With the proposed L-BD-SCUC model, the total cost decreases by 4.21% comparing with the T-SCUC model. The battery degradation cost significantly decreases by 41.3%. On the other hand, the fuel cost increases by 0.8% due to the change of BESSs' schedule. Comparing with the decreasing battery degradation cost, the increment of fuel cost is insignificant.

Table 5.3 Results for IEEE-24 bus system.

IEEE 24-bus test systems with 5 BESSs			
	Fuel Cost ($)	BD Cost ($)	Total Cost ($)
T-SCUC	256,404.60	34,643.80	291,048.40
L-BD-SCUC	258,448.90	20,348.10	278,797.00
Reduction	-0.80%	41.30%	4.21%

Fig. 5.2 to Fig. 5.6 present the scheduled BESS operation curves with the L-BD-SCUC model and benchmark model for the five-BESS integrated system. From the results, we can observe that all the BESSs are scheduled to be more "active" for T-SCUC than L-BD-SCUC. "Active" represents the periods that BESS is on charging/discharging status instead of idle. In addition, the BESS output/input power in each time period is generally scheduled to be higher in T-SCUC than L-BD-SCUC. These results are because battery degradation cost is considered in the L-BD-SCUC model. The charge/discharge rate and DOD play a vital role in the NNBD model. Therefore, the BESS is scheduled to charge/discharge in a narrow power range and in less time periods to decrease the amount of battery degradation and the equivalent cost. The results show that the majority time periods are set to idle for BESS 1 and 2 in L-BD-SCUC model. For BESS 3, 4, and 5, active time periods are similar between L-BD-SCUC and T- SCUC. However, they are scheduled in a narrow power range for L-BD-SCUC model to decrease battery degradation. The results may be affected by the bus location of the BESSs and wind farms. Overall, the BESSs' schedule indicates that the proposed L-BD-SCUC method is able to obtain the solution for multi-BESSs integrated bulk power system.

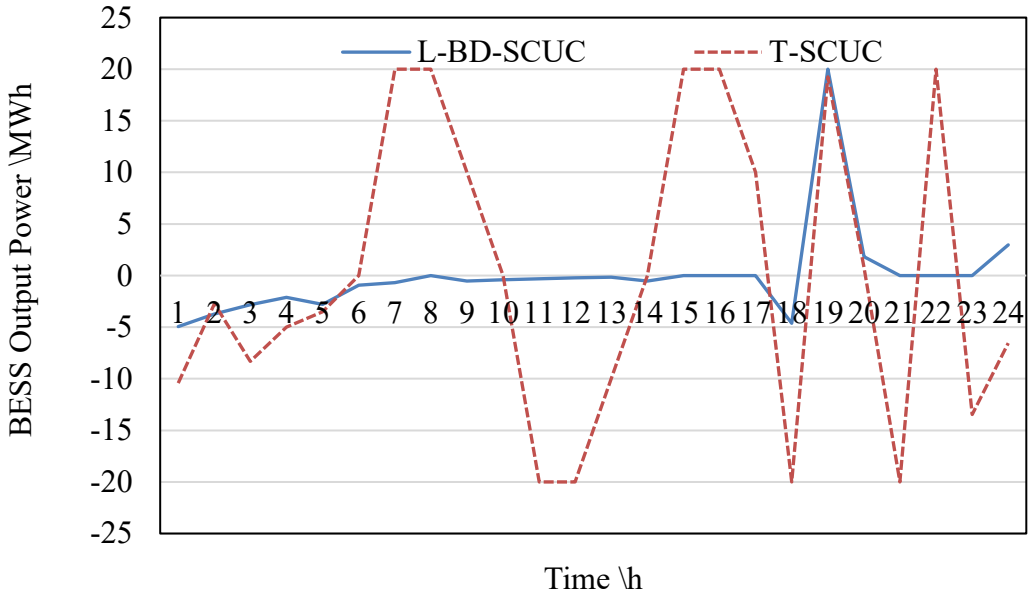

Fig. 5.2. Output power of BESS #1.

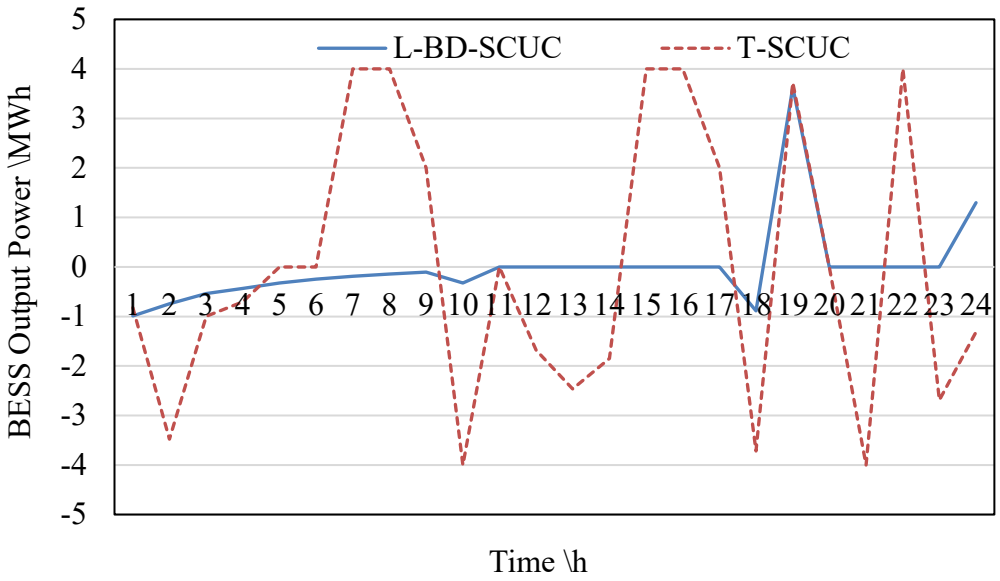

Fig. 5.3. Output power of BESS #2.

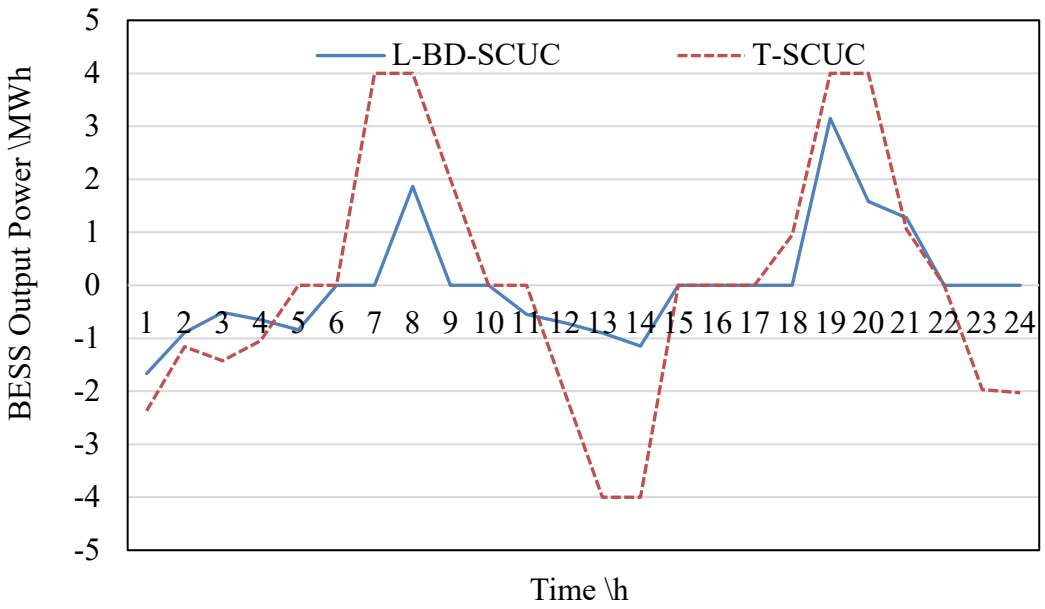

Fig. 5.4. Output power of BESS #3.

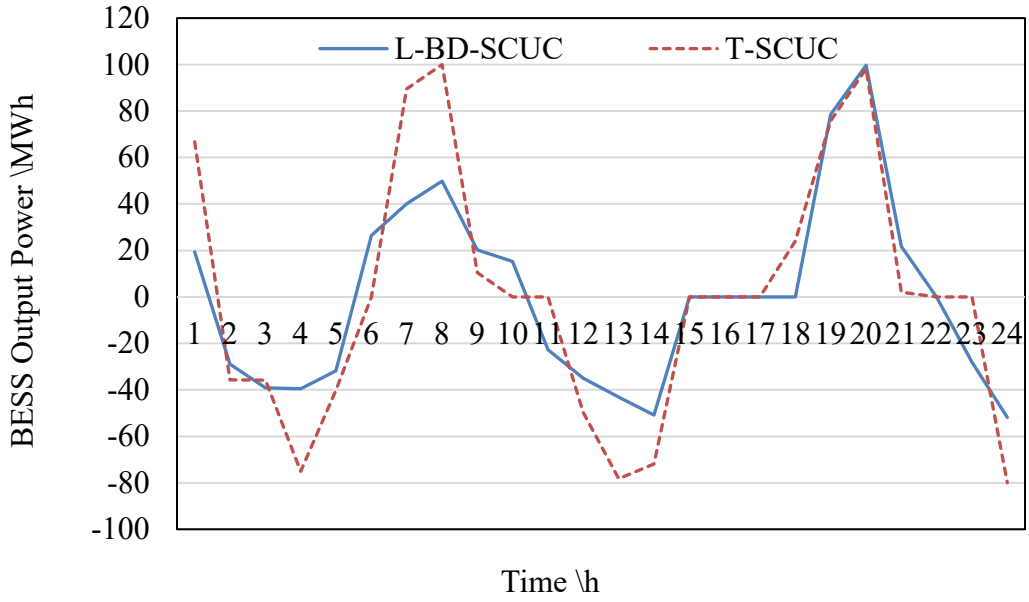

Fig. 5.5. Output power of BESS #4.

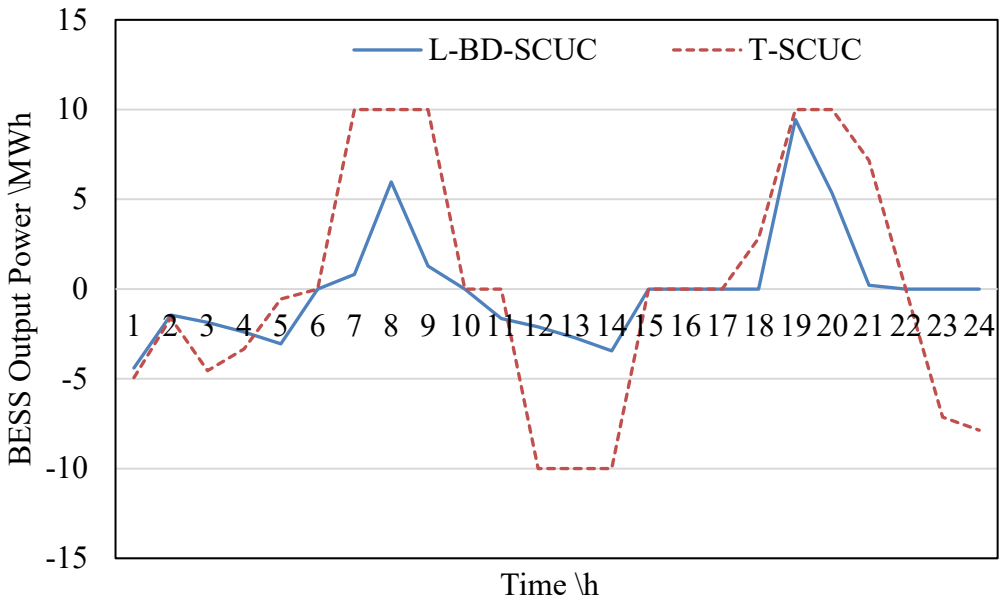

Fig. 5.6. Output power of BESS #5.

Table 5.4 presents the sensitivity tests on optimization relative mipgap (rel-mipgap) with the implement of L-BD-SCUC method shown above. In previous results, we select the 0.01 as the value of rel-mipgap and it took 357.2 seconds to converge. For rel-mipgaps with 0.001 and 0.0001, the program terminates due to the pre-set maximum solving time, which indicates the model cannot find the optimal solution within desired mipgaps. The long computing time and convergence issue motivate us to conduct further sensitivity tests on system scenarios with different numbers of BESSs.

Table 5.4 Relative mipgap tests on 5-BESS system.

Optimization Mipgap	Total Cost ($)	Degradation Cost ($)	Solving Time (s)
0.1	302,843.2	19,515.2	47.2
0.01	278,797.0	20,348.1	357.2
0.001	278,777.4	20,338.3	3600
0.0001	278,774.5	20,338.5	3600
0	278,774.5	20,338.5	3600

Table 5.5 presents the results of sensitivity analysis on the number of BESSs. The rel-mipgap is set to 0.01 for all the tests in Table 5.5. From Table 5.5, it is clear that the solving time significantly increases as the number of BESSs increases, which indicates the solving efficiency decreases with more BESS buses integrated into the system.

The proposed model can also be applied to illustrate the economic benefits of integrating BESS into power systems. Table 5.6 shows the economic results for different total energy capacities of BESSs. The cost represents the capital investment cost of all the BESSs. The economic benefit represents the total lifetime revenue with the implementation of BESSs. The revenue is calculated based on the difference between the total cost of a BESS integrated system and a benchmark system with no BESS. The expected lifetime is obtained based on average daily battery degradation with SOH_{EOL} being set to 50%. The average daily battery degradation is obtained from the proposed model which consists no extra operation limits for BESS such as cycle limit, rate limit, DOD limit and SOC limit. However, the battery operation is usually limited in order to extend the lifespan in practice. Thus, the actual lifetime should be longer than the results listed in Table VI at the cost of limiting battery daily usage. We find that with a higher installed BESS capacity, the SCUC cost decreases. The SCUC cost here represents the total cost of L-BD-SCUC model. However, the higher BESS capacity may not be the optimal choice. It also depends on the renewable generation capacity and the bus location of BESSs in the system.

Table 5.5 Results of sensitivity analysis on number of BESS in the system

Numbers of BESS	1	2	3	4	5
Solving Time (s)	17.7	29.3	134.3	234.7	357.2

Table 5.6 Economic results.

Total BESS Capacity (MWh)	Cost ($ in millions)	Economic benefit ($ in millions)	Expected lifetime (years)	SCUC total cost ($)
50	5.5	12.02	11.6	$300,202
100	8	46.04	11.6	$292,166
200	15	78.65	11.4	$284,136
300	22	101.3	9.2	$270,935
500	36	102.94	9.6	$273,661

5.6 Summary

This chapter introduces a novel security-constrained unit commitment model with linearized neural network based battery degradation model that is proposed to linearize the learning based battery degradation model to make battery degradation considered SCUC problem directly solvable in this chapter. A linearization model is formulated to linearize the activation functions of the NNBD model. The results of this research demonstrate that the proposed L-BD-SCUC method can effectively solve battery degradation-based SCUC for a power system with multiple BESS buses. The statistical economic results of the proposed method give an overview of the potential economic benefit of the BESS integration and provide insights into power system planning. One finding from this study is that the computational burden will increase substantially as the number of BESS in the power system increases. Although the

proposed L-BD-SCUC method can solve the cases with multi-BESSs, the low efficiency indicates that further research beyond this work and our prior work is still needed. To summarize, with the proposed L-BD-SCUC, an alternative method is available to efficiently solve the NNBD embedded SCUC problem.

6. COMPUTATIONAL ENHANCEMENT OF BATTERY DEGRADATION BASED ENERGY SCHEDULING MODEL

6.1 Literature Review

Deep learning (DL) is playing a crucial role in enhancing the operational efficiency and reliability of power systems, particularly in the context of high RES penetration and the associated challenges of intermittency and unpredictability [100]. DL has been widely adapted to assist the power system operation such as, optimal power flow, day ahead scheduling, restoration, and state estimation [101]–[103]. DL is an important technology for contributing to the transition towards more sustainable and resilient power grids.

The outstanding performance of deep learning technologies has ushered in innovative solutions for numerous challenging power system issues that traditional methods struggle to address. Today's power system is confronting formidable challenges, primarily due to the extensive integration of RES into the grid. Deep learning methods have emerged as indispensable tools within the power system area. Based on different attributes of DL models, they have been found to be useful in diverse applications in solving a range of power system problems. For example, a deep neural network (DNN) consisting of only fully connected dense layers is developed in [104] to predict active power flows and it outperforms the widely-used linearized DC power flow model. The utilization of graph neural networks (GNN) in [105] allows for efficient predictions of current and power injection, capitalizing on GNN's topological advantages. Convolutional neural network is adapted to predict the

rate of change of frequency under large disturbances to ensure the system stability in [106]. Furthermore, fault detection including fault type and location can be predicted by the artificial neural network as presented in [107]. Meanwhile, recurrent neural networks are widely used in time sequential prediction such as load forecasting, electricity price prediction, weather forecasting, and renewable generation forecasting, offering versatile solutions to contemporary power system challenges [108]−[111].

Most DL models adopt the rectified linear unit (ReLU) as the nonlinear activation function between the hidden layers to enhance the training efficiency and robustness [112]. Nevertheless, the ReLU introduces the nonlinearity to the DL models which make them nonlinear [113]. While this nonlinearity poses no issue for deterministic problems like fault detection and power flow prediction, it can become a significant obstacle when integrating the trained DNN model into optimization problems where DNN's input features are decision variables to be solved, rendering them suddenly unsolvable due to the introduced nonlinearity. Remarkably, none of the previously mentioned studies have addressed the crucial challenge of linearizing the ReLU function in DNNs. Thus, there exists a significant research gap concerning the development of methods to linearize ReLU-based DNNs.

6.2 ReLU Approximation Methods

To address the challenge, we have proposed four different models to linearize the ReLU activation function. The proposed four models include: (i) Big-M based piecewise linearization (BPWL), (ii) convex triangle area relaxation (CTAR), (iii)

penalized CTAR (P-CTAR), and (iv) penalized convex area relaxation (PCAR). BPWL is able to fully linearize the ReLU activation function without any approximation while the rest three models make some approximations to decrease the computational complexity.

Our previous work in chapter 4 has introduced a novel neural network based battery degradation (NNBD) model aimed at accurately quantifying the battery degradation values per usage profile. The proposed NNBD model is able to predict the battery degradation value for each cycle based on the input of state of charge (SOC), state of health (SOH), depth of discharge (DOD), ambient temperature, and charge/discharge rate (C Rate). The NNBD model enables the incorporation of battery degradation into microgrid daily operational energy scheduling. However, this integration encountered unexpected computational burden due to the nonlinear nature of the NNBD model that utilizes the ReLU activation function in the hidden layers; this poses challenges when NNBD is incorporated into the optimal day-ahead generation scheduling problems. To address this issue, we will evaluate the proposed four ReLU linearization models in the testbed of NNBD-integrated microgrid day-ahead scheduling (MDS) model. It is worth mentioning that the proposed ReLU linearization methods not only fit the proposed NNBD model and optimal energy scheduling applications, but also applicable to a broader spectrum of DL-embedded optimization models that contains neural networks with ReLU activation functions.

6.2.1 Proposed Linearization Models

This section presents the formulations of four models designed to linearize the ReLU activation function within the neural network model. The fully connected neural network models are characterized by a series of equations that describe the calculation and activation processes of neurons. Each neuron's pre-activated value x_h^i is computed by (6.1), factoring in input features from the previous layer, the corresponding weight matrix W, and biases matrix B. Most neural network models employ ReLU as the activation function, as shown in (6.2). While this activation function is prevalent for introducing nonlinearity to capture intricate relationships among variables, the nonlinearity of the ReLU function can pose challenges when it is embedded in the optimization problem. To address this challenge, the ReLU activation function can be linearized by applying the proposed linearization models described in this section. Notably, the proposed linearization models can be applied to any optimizations models that needs to efficiently integrate nonlinear ReLU activation function. The ReLU activation function and neuron calculation are shown as,

$$x_h^i = \sum a_{h-1}^i * W + B, \tag{6.1}$$

$$a_h^i = ReLU\left(x_h^i\right) = max(0, x_h^i). \tag{6.2}$$

BPWL method is adapted to reformulate the ReLU function represented by (6.1) into (6.3)-(6.6) as listed below:

$$a_{\mathrm{h}}^i \le x_{\mathrm{h}}^i + BigM * (1 - \delta_{\mathrm{h}}^i), \tag{6.3}$$

$$a_{\mathrm{h}}^i \ge x_{\mathrm{h}}^i, \tag{6.4}$$

$$a_{\mathrm{h}}^{i} \leq BigM * \delta_{\mathrm{h},}^{i} \tag{6.5}$$

$$a_{h}^{i} \geq 0, \tag{6.6}$$

where δ_{h}^{i} is a binary variable represents the activation status of neuron i in layer h, and $BigM$ is a pre-specified numerical value that is larger than any possible value of $|x|$. As shown in Fig. 6.1, the BPWL model offers the distinct advantage of perfectly linearizing the ReLU activation function without any reformulation losses, which is illustrated by the fact that the BPWL line in Fig. 6.1 completely overlaps the ReLU function curve. However, this method requires one additional binary variable for each neuron that applies the ReLU function, which may significantly increase the computational complexity.

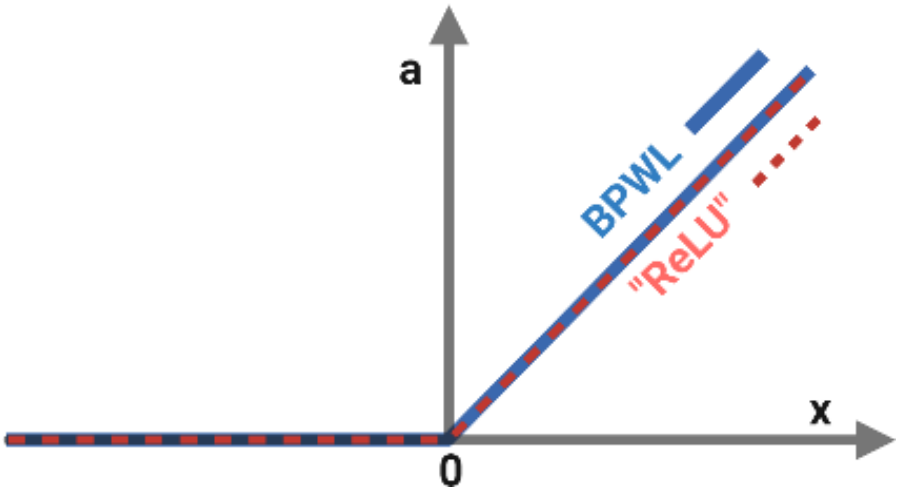

Fig. 6.1. Illustration of the BPWL model for ReLU linearization.

The proposed CTAR approximate the ReLU function at each neuron with (6.4) and (6.6)−(6.7) as shown below,

$$a_{\mathrm{h}}^{i} \leq \frac{UB}{UB - LB} x_{\mathrm{h}}^{i} - \frac{UB \cdot LB}{UB - LB}, \tag{6.7}$$

which constrains the feasible solution set. CTAR offers a pure linear representation of ReLU, introducing minimal complexity to optimization problems while acknowledging the presence of approximation errors. As shown in Fig. 6.2, the blue area denotes the feasible region, delimited by the lower bound (LB) and upper bound (UB), both of which are determinable from the neural network model. Specifically, LB should be less than the minimum neuron preactivated value, while UB should exceed the maximum neuron preactivated value. In most cases with normalized training data, each neuron's value falls within the range between -1 to 1. It's noteworthy that different choices for LB and UB can impact the performance of the CTAR linearization method.

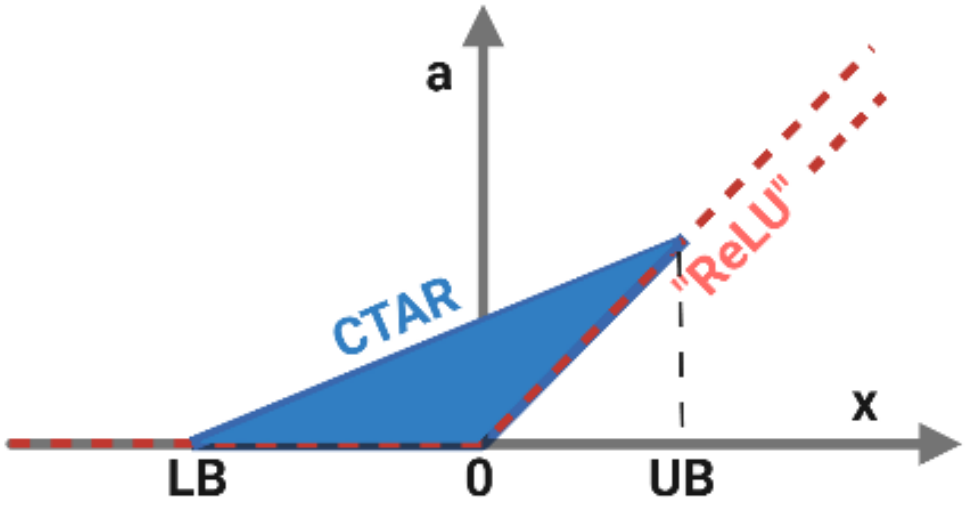

Fig. 6.2. Illustration of the CTAR model for ReLU linearization.

The proposed P-CTAR model is introduced to reduce the approximation error associated with CTAR model with (6.4) and (6.6)−(6.8). To achieve this, a mitigation

strategy involves incorporating a penalty term c_h into the objective function of the optimization model shown as,

$$f^c = \sum a_{\mathrm{h}}^i c_h, \tag{6.8}$$

in which the penalty encourages the nonnegative variable a_h^i to be positioned closer to the lower two sides, corresponding to the actual ReLU activated values, within the triangular representation as shown in Fig. 6.3.

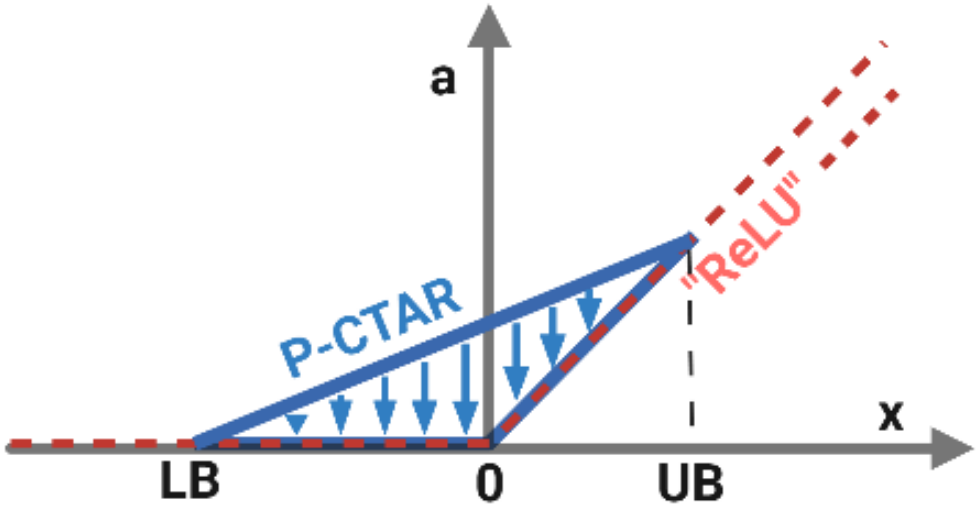

Fig. 6.3. Illustration of the P-CTAR model for ReLU linearization.

The proposed PCAR method is designed to add a penalty term c_h on nonnegative a_h^i without LB and UB, represented by (4), (6), and (8), which force the a_{h}^i to be set at the ReLU activated values as shown in Fig. 4. As compared to CTAR, the PCAR method offers enhanced accuracy, especially when equipped with sufficiently large penalty terms, and notable efficiency gains due to the absence of constraints (7). Thus, this method stands out for its ability to significantly reduce computational complexity when compared to other available linearization approaches.

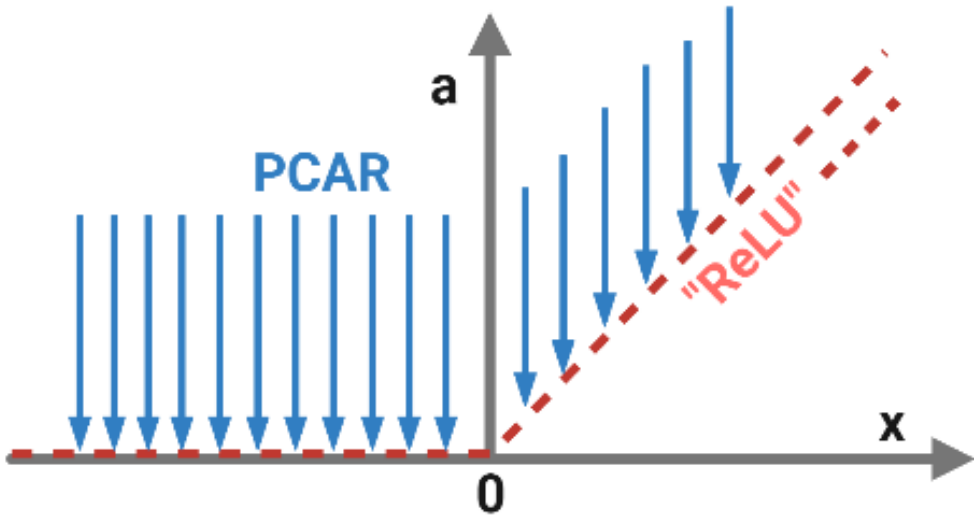

Fig. 6.4. Illustration of the PCAR model for ReLU linearization.

6.2.2 ReLU Approximation for NNBD based MDS Models

Since the nonlinear ReLU activation function make the optimization model extremely hard to solve if not unsolvable, we have reformulated the MDS models to make it linear and solvable with the proposed four ReLU linearization models respectively. The updated objective function (33) is required for two of the proposed models: P-CTAR and PCAR. The linearized NNBD-integrated day-ahead energy scheduling models are defined in Table 6.1.

Table 6.1 The Proposed Linearized ReLu Models

Models	Equations
BPWL-MDS	(6.3)-(6.6)
CTAR-MDS	(6.4), (6.6)-(6.7)
P-CTAR-MDS	(6.4), (6.6)-(6.8)
PCAR-MDS	(6.4), (6.6), (6.8)

6.2.3 Results Analysis

To evaluate the effectiveness of the linearized day-ahead scheduling model, we utilized a representative grid-connected microgrid [19] as the test case in this work, featuring several distributed energy resources including renewables and controllable units. The microgrid setup encompasses various key components, notably a conventional diesel generator, wind turbines, residential houses with solar panels, and a lithium-ion BESS with a charging and discharging roundtrip efficiency of 90%. The parameters for these main components are provided in Table 6.2. To simulate real-world scenarios accurately, the load data for the microgrid is obtained from the electricity consumption patterns of 1000 residential households from the Pecan Street Dataport [22]. Additionally, for a comprehensive representation of environmental conditions, the ambient temperature and available solar power data are sourced over a 24-hour period from the same Pecan Street Dataport source.

Table 6.2 Microgrid Testbed

Main Components	Diesel Generator	Wind Turbines	Solar Panels	Lithium-ion BESS
Size	180kW	1000kW	1500kW	300kW

Table 6.3 presents the performance results obtained from the microgrid testbed based on the four proposed linearization models. In Table II, the term, *Degradation*, represents the degradation value calculated by the proposed linearization methods, while the term, *Real Degradation*, represents the degradation value computed separately by the NNBD model with the BESS operation profile to gauge the accuracy of the linearization models. The term, *Error*, is derived from the

comparison between *Degradation* and *Real Degradation*. The term, *Total Cost*, represents the combined MDS operation cost and the equivalent degradation cost. It's important to note that this equivalent degradation cost is derived from *Degradation* which may introduce the linearization approximation error. The term, *Real Total Cost* represent the combined MDS operation cost and the real equivalent degradation cost based on the *Real Degradation.* Also, the *Total Cost* in Table III has already excluded the penalty cost for P-CTAR and PCAR models. The outcomes indicate that BPWL yields the lowest linearization error, attributed to its complete linearization of the ReLU activation function. The minimal degradation prediction error is a result of rounding the weights in the NNBD model during the battery degradation value verification process. Ideally, there should be zero linearization error.

Table 6.3 MDS Results

MDS	BPWL	CTAR	P-CTAR	PCAR
Degradation	0.0368%	0%	0.0344%	0.094%
Real Degradation	0.037%	0.0487%	0.0348%	0.15%
Error %	0.543%	100%	1.14%	37%
Total Cost	$530	$489	$530	$651
Real Total Cost	$530	$543	$530	$719
Solving Time	28 s	0.9 s	8.75 s	0.58 s

However, it's worth mentioning that the BPWL model does require a relatively longer solving time due to the exponential addition of new binary variables to the optimization problem. Although the current solving time of 28 seconds remains acceptable for a microgrid case, it will increase significantly for larger systems. Overall, the BPWL model accurately represents the ReLU function with no reformulation losses but introduces binary variables, complicating the optimization

model and leading to longer solving times. In contrast, the computation times for the other linearization methods are significantly less. Notably, PCAR yields the shortest solving time, as expected, given its fewer constraints compared to CTAR and P-CTAR.

The three MDS models with non-exact ReLU linearization achieve different accuracies. The proposed P-CTAR model exhibits the second-lowest error among the four proposed methods, signifying its ability to accurately linearize the ReLU activation function. A comparative analysis between CTAR and P-CTAR reveals that CTAR introduces substantial linearization errors, suggesting an ineffective linearization approach in this particular case. The significant approximation error in CTAR results from the absence of a penalty term in the model. This may change if the MDS model changes. In contrast, the P-CTAR model incorporates a penalty term in addition to the CTAR model, leading to a considerable enhancement in performance relative to CTAR. The P-CTAR model outperforms the PCAR model which implies that the chosen lower bound and upper bound values for CTAR are appropriate and effective in this testbed. The PCAR model, however, exhibits a linearization error of 37%, notably higher than P-CTAR. It's important to note that both PCAR and P-CTAR models' linearization errors are influenced by the penalty constant in the objective function, which requires additional sensitivity test to determine the optimal setup. While BPWL outperforms the other three models in terms of linearization accuracy, it lags behind in solving efficiency, especially when considering larger systems where it could potentially lead to significantly extended solving times. In

contrast, P-CTAR stands out as the best performance model in terms of linearization error among the rest of the models. The solving time is decreased significantly compared to the BPWL model while maintaining the linearization performance.

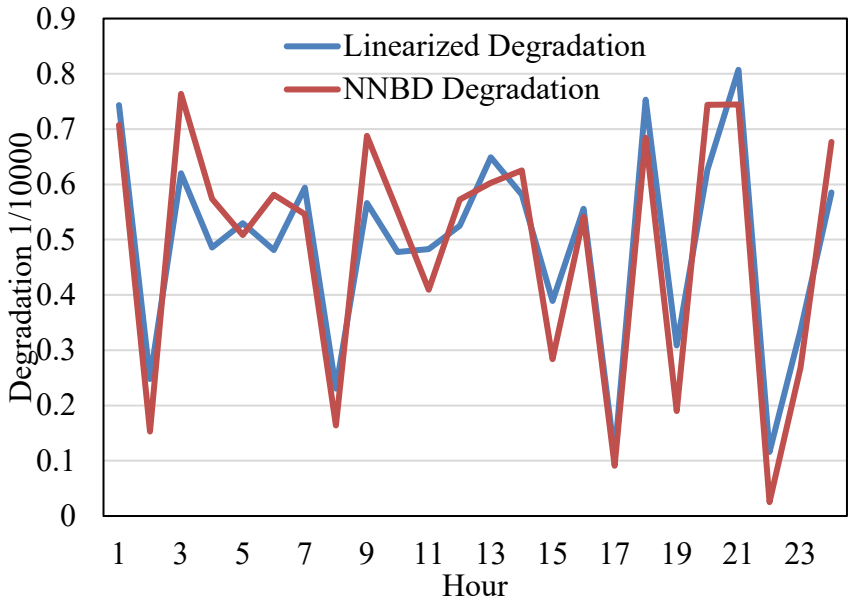

Fig. 6.5. P-CTAR model degradation comparison.

Figure 6.5 graphically illustrates the linearization performance of the P-CTAR model when compared to the reference NNBD degradation value, which is based on the BESS operation profile per usage cycle. The linearized degradation, produced directly from the optimization model using the P-CTAR model to linearize the internal ReLU function of the NNBD model, exhibits a trend that closely aligns with the benchmark model. While there are some deviations in specific time periods, the overall degradation value over the 24-hour look-ahead scheduling horizon demonstrates minimal prediction error, affirming the efficacy of the P-CTAR linearization model.

It's noteworthy that during the design of the proposed linearization models, the expectation was that P-CTAR might introduce additional complexity to the optimization model, potentially leading to longer solving times. The results indeed align with this expectation, as the P-CTAR model's solving time surpasses that of the CTAR model. This trade-off between model efficiency and accuracy is duly considered in our evaluation.

Figure 6.6 presents the results of a sensitivity test for the P-CTAR model using different penalty cost constants denoted as c_h. This penalty cost serves the purpose of mitigating the approximation error associated with the CTAR model. However, it's important to note that different values of c_h may lead to different outcomes, as the penalty cost is directly integrated into the objective function of the optimization problem. The objective cost reflects the expenses incurred by the objective function (33), while the penalty cost accounts for the costs introduced by the P-CTAR model. The real cost represents the MDS operating cost and the battery degradation cost, calculated as the difference between the objective cost and the penalty cost. However, the battery degradation cost here may include an error due to the linearization approximation of the P-CTAR model. Upon examination of the figure, it becomes evident that there is no significant variation in the real cost as c_h increases. However, the lowest linearization error is observed when c_h is set to 10. Beyond this threshold, increasing c_h leads to an escalation in battery degradation error which is directly caused by the error of linearization model. In summary, the selection of c_h demands careful consideration and thorough preliminary testing to ensure the

optimal performance of the P-CTAR model. It's essential to emphasize that the optimal c_h value provided here pertains specifically to the NNBD-based MDS optimization problem. If the optimization model undergoes any modifications, it would require recalibration to determine the ideal c_h value for the optimal setup.

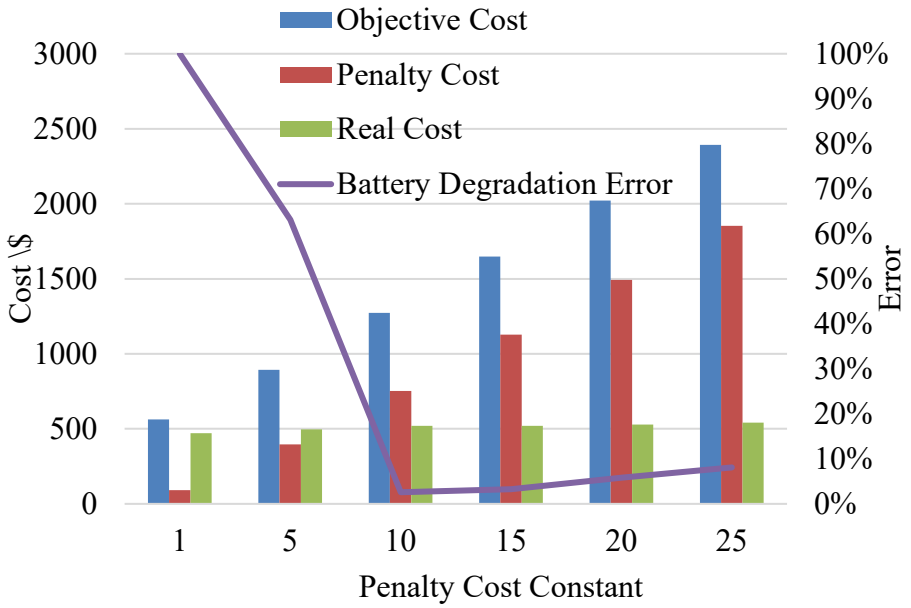

Fig. 6.6. P-CTAR sensitivity tests.

We also conducted a sensitivity test on the PCAR model with varying c_h values, and the results are depicted in Figure 6.7. It's noticeable that as we increase the c_h value, the linearization error does not exhibit a substantial decrease. In essence, there doesn't appear to be an optimal c_h value for the PCAR model that significantly enhances linearization accuracy. While the PCAR model demonstrates effectiveness, it doesn't achieve the same level of performance as the P-CTAR model. Consequently, for the NNBD-integrated MDS optimization problem, the PCAR model may not represent the most ideal solution. However, it's worth noting that the PCAR model

could potentially serve as the optimal solution for other neural network-based optimization models with distinct characteristics and requirements.

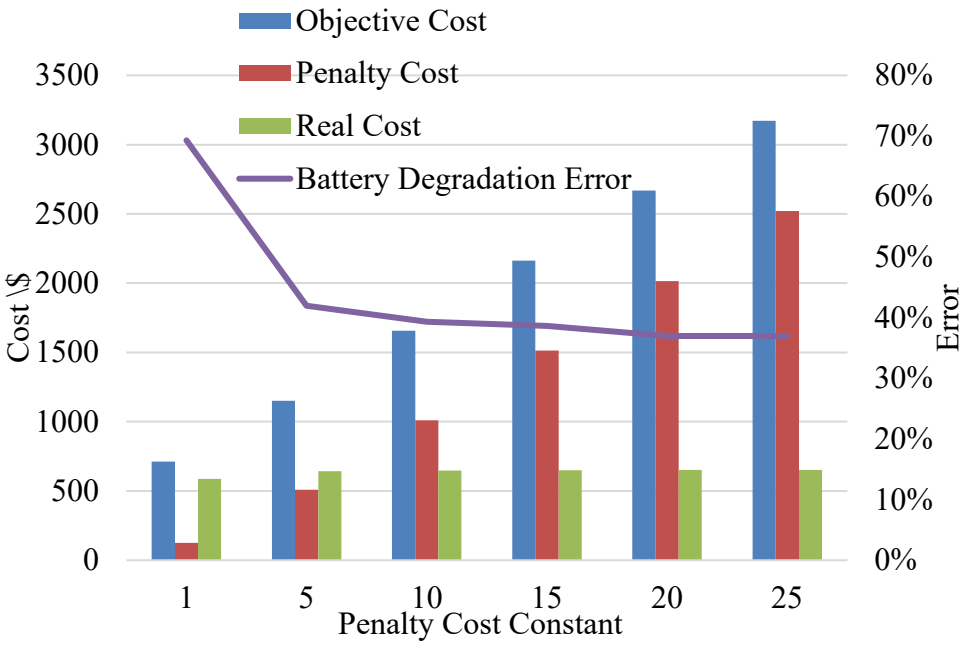

Fig. 6.7. PCAR sensitivity tests.

6.3 Sparse Neural Network Model

Heuristic methods were proposed in reducing the complexity of neural network models. For instance, in [114], a low-complexity neural belief propagation decoder is constructed using network pruning techniques. This approach involves removing unimportant edges from the network structure. However, it should be noted that these techniques may inadvertently decrease the training accuracy. Another approach to reducing complexity is the utilization of a sparse feature learning model [115]. This model focuses on learning useful representations and decreasing the complexity of hierarchical deep neural network models. In [116], the effectiveness of

sparse convolutional neural networks for single-instruction-multiple-data (SIMD)-like accelerators is demonstrated. This technique helps alleviate the computational burden by applying pruning methods to eliminate unnecessary connections within fully connected structures, as exemplified in [117] for wideband power amplifiers' neural network models. Similarly, pruning techniques are also employed in [118] to compact the deep neural networks for SCADA applications. Furthermore, [119]−[120] suggest that modern deep neural networks often suffer from overparameterization, with a large number of learnable parameters. One potential solution to this issue is model compression through the use of sparse connections. These approaches contribute to reducing the complexity and computational burden associated with neural network models, enabling more efficient and streamlined implementations.

Since the sparsity and pruning techniques have proved to be efficient to reduce the complexity of neural networks in many other applications, it may be a perfect solution to obtain a low computational complexity model in battery degradation prediction. Thus, we propose a sparse neural network-based battery degradation model (SNNBD) to quantify the battery degradation in BESS daily operations. SNNBD is designed to be significantly less complex than the traditional fully-connected dense neural network model. SNNBD is designed to reduce the computation burden induced by the ReLU activation function. Achieving this entails a strategic process of pruning during training, whereby a predetermined percentage of neurons is systematically pruned. The sparsity percentage is defined as the ratio of pruned neurons to the total neurons in the neural network. A higher percentage of

sparsity may decrease the computation complexity significantly, but the accuracy of the battery degradation prediction may decrease as compared with a less-sparse or dense model. It will be a trade-off between the sparsity and the training accuracy. Compared to the NNBD model, the proposed SNNBD model contains only a percentage of NNBD's neurons which may reduce the computational burden significantly while maintaining accurate battery degradation prediction.

6.3.1 Training Strategies

This section outlines the training process for the proposed SNNBD model. We proposed two training schemes: (i) Warm Start that trains the SNNBD based on the pre-trained NNBD model, and (ii) Cold Start that trains the SNNBD model directly with random initial weights. Both models consist of 5 input neurons, 20 neurons in hidden layer 1, 10 neurons in hidden layer 2, and 1 neuron in the output layer. The hidden layers utilize the ReLU as the activation function for each neuron.

A. Warm Start

The training process for Warm Start is illustrated in the algorithm explained below. Initially, the weights derived from the trained neural network model are utilized as the initial weights for the SNNBD model. During the training of the SNNBD model, a pruning mask is generated based on a certain predetermined sparsity percentage value. This mask is then applied to prune the weights after each training epoch to achieve the desired sparsity. The pruning masks are binary matrices that indicate which neurons are pruned (set to zero) in order to achieve sparsity throughout the entire structure.

Training Algorithm: Sparse Neural Network

1. Obtain the weights matrices ω from the pre-trained NNBD model.
2. Set the sparse percentage ε.
3. Set the training epochs.
4. **For** $e\ in$ epochs,
5. | Set the Pruning masks matrices with the $\boldsymbol{\varepsilon}$
6. | Update weights matrices by $\boldsymbol{\omega} * \boldsymbol{\varepsilon}$
7. | Tune the weights matrices with gradient descent.
8. **end For**

B. Cold Start

Cold Start offers a simple approach compared to Warm Start. Instead of training the neural network based on the fine-tuned NNBD weights, Cold Start directly trains a sparse neural network using random initial weights. In essence, the key difference between Warm Start and Cold Start lies in the choice of initial weights. However, all other training techniques re-main consistent between the two options. The performance and efficiency of both Warm Start and Cold Start will be evaluated and compared the performance.

6.3.2 Pruning Method

Pruning is a technique employed in neural networks to reduce the size and complexity of a model by eliminating unnecessary connections or neurons [121]. The objective of pruning is to enhance the efficiency of the training model, minimize memory requirements, and potentially improve its generalization capabilities. During the pruning process, a pruning mask is applied to identify and eliminate neurons that contribute less to the overall network performance, as depicted in Fig. 1. The pruning masks are regenerated for each epoch which means each pruning mask are identical. It

also helps the robustness of the proposed SNNBD model. These pruning masks enable a compact representation of the sparse neural network. Instead of storing and computing all connection weights, only the active connections are considered, resulting in reduced memory usage and computational demands. By incorporating pruning masks, sparse neural networks strike a balance between model complexity and efficiency, making them a valuable approach for various applications, particularly in scenarios with limited computational resources or deployment constraints.

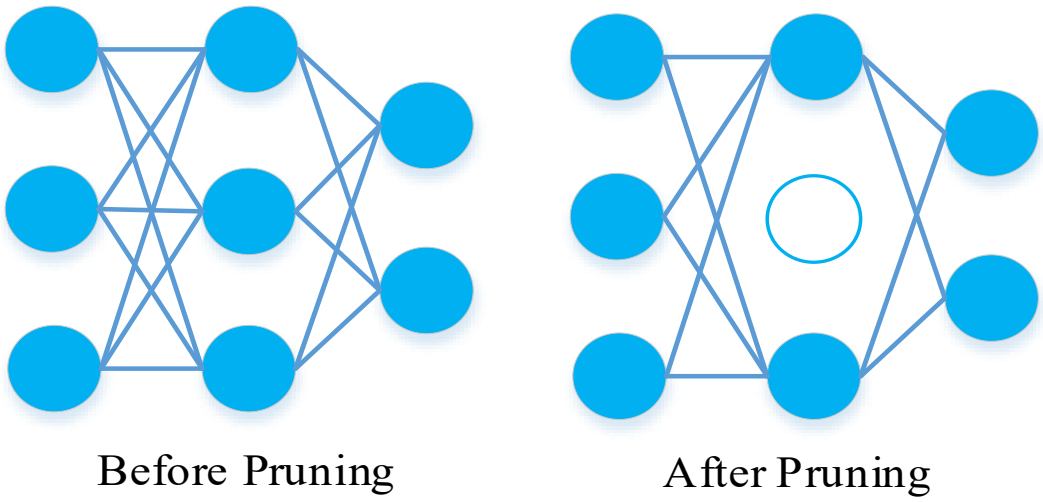

Fig. 6.8. Pruning of a sample neural network model.

6.3.3 Training Results

The analysis of training outcomes, as illustrated in Table 6.4, distinctly highlights the superiority of Warm Start over Cold Start concerning training accuracy. However, it's noteworthy that Cold Start requires fewer epochs to complete the training process. It is important to mention that the training epochs for Warm Start represent the combined training epochs required by the NNBD model and the SNNBD

model, while for Cold Start, it refers to the training epochs of the sparse neural network alone. Training the sparse neural network from random initial weights (Cold Start) proves to be notably challenging when it comes to achieve an equivalently level of accuracy as the Warm Start. In contrast, Warm Start is designed to take advantage of the pre- trained NNBD model, which serves as a stable starting point. The SNNBD model is then applied to further refine and sparse the structure of the already trained model. This suggests that the pre-trained NNBD model provides a beneficial foundation for the SNNBD model. The initial training with the NNBD model establishes a solid baseline, and the subsequent application of the SNNBD model enables fine-tuning with sparsity. By leveraging the existing knowledge encoded in the NNBD model, Warm Start demonstrates superior training accuracy compared to Cold Start.

Table 6.4 Results between Warm Start and Cold Start

Training Options	Accuracy	Epochs
Warm Start	94%	550
Cold Start	77%	300

All the results presented in Figure 6.9 are based on training Warm Start, as it outperforms the Cold Start. The training results of the proposed SNNBD model are depicted in Fig. 6.9 and Table 6.5. In Fig. 6.9, the 0% sparsity represents the original NNBD model without any sparsity applied. The subsequent markers—5%, 10%, and 15%—tinted in blue, red, and green, respectively, signify distinct error tolerance thresholds. Notably, the pattern that unfolds the interplay between sparsity and prediction accuracy. As sparsity percentage scales up, the precision of battery

degradation value predictions undergoes a gradual decrement across all tolerance thresholds. This trend continues until the 70% sparsity mark is attained. When comparing the 0% sparsity model (NNBD model) and the 50% sparsity model, the accuracy stands at 94.5% and 93.7% respectively, considering a 15% error tolerance. However, the 50% sparsity model significantly reduces the computational complexity compared to the original NNBD model since half of the neurons are pruned to be zero, thereby eliminating their connections. This reduction in computational complexity is exponential, as all connections associated with zero-valued neurons are discarded.

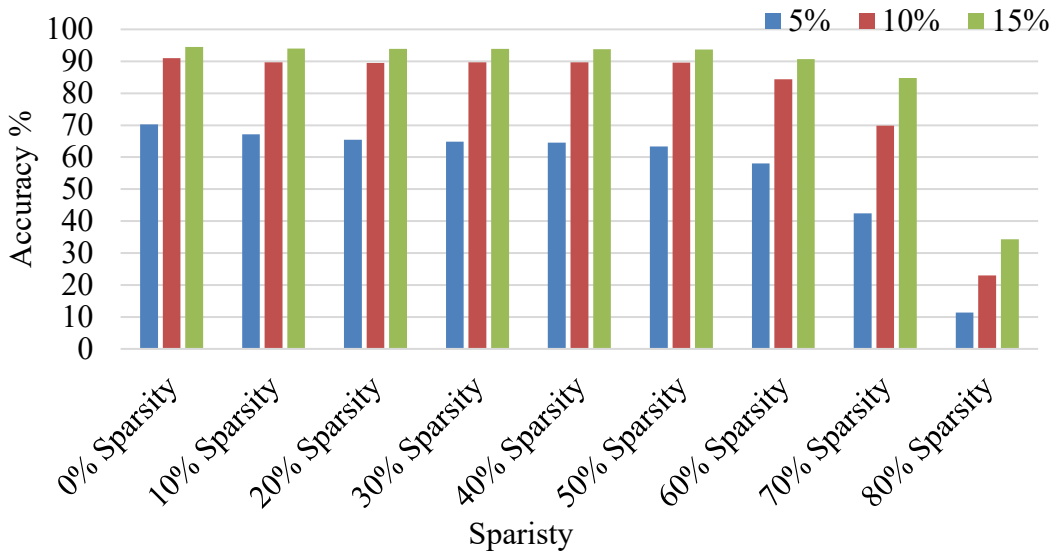

Fig. 6.9. Training results of SNNBD model at different sparsity levels.

Table 6.5 Training accuracies of proposed SNNBD model under different sparsity levels and error tolerances

Sparsity Percentage	Error Tolerances		
	5%	10%	15%
0%	70%	91%	95%
10%	67%	90%	94%
20%	66%	90%	94%
30%	65%	90%	94%
40%	65%	90%	94%
50%	63%	90%	94%
60%	58%	84%	91%
70%	42%	70%	85%
80%	11%	23%	34%

All of these models, including the original NNBD model and models with various sparsity levels, will be integrated into the day-ahead scheduling problem to evaluate their performance. This integration will provide further validation and enable the evaluation of their effectiveness in improving the overall optimization process in the day-ahead scheduling problem.

6.3.4 Microgrid Test Case

The SNNBD integrated day-ahead scheduling model is evaluated based on the same microgrid testbed in section 4. Table 6.6 presents the validation results for different sparsity levels of the SNNBD models in the microgrid day-ahead scheduling problem. The table provides insights into the performance of these models across various metrics. "Pseudo Total" represents the total cost with the SNNBD model, which serves as the objective of the day-ahead scheduling including the operating cost and degradation cost in optimization problem. "BD Cost" represents the equivalent battery degradation cost estimated using the SNNBD model. "Operation" shows the

microgrid operating cost, including the cost associated with generators and power trading. "OG BD Cost" indicates the battery degradation cost obtained from the original NNBD model, which does not incorporate sparsity. "Updated Total" represents the sum of the operation cost and the "OG BD Cost". "0% sparsity" is considered as the benchmark model, used to evaluate the performance of the other SNNBD models with different sparsity levels.

From the information in Table 6.6, it appears that the SNNBD model does not significantly reduce the solving time in the microgrid model. Furthermore, there is no substantial difference observed in the total cost and updated total cost among the various SNNBD models compared to the benchmark model. These findings suggest that the inclusion of sparsity in the SNNBD model does not significantly impact the overall cost in the microgrid day-ahead scheduling problem. Fig. 6.10 illustrates the output curves of the BESS under different battery degradation models. The figure shows that the BESS charge/discharge power profiles largely overlap across most time intervals. The only notable difference is observed in the 10% and 20% sparsity models, where the BESS charges at 20 kW during the 7-8 pm. Overall, these results demonstrate that the SNNBD model is capable of finding solutions for the day-ahead scheduling problem. Based on these findings, it can be concluded that the SNNBD model is reliable and able to identify optimal solutions compared to the non-sparse NNBD model in the microgrid day-ahead scheduling problem. However, it should be noted that the SNNBD model does not yield efficiency improvements, even with higher sparsity levels. One possible reason for this observation could be the small

scale of the microgrid case and the presence of only one BESS, which does not impose a heavy computational burden.

Table 6.6 Microgrid energy scheduling results

Sparsity	0%	10%	20%	30%	40%
Pseudo Total ($)	501.5	499.94	500.88	501.2	501.04
BD Cost ($)	7.27	7.93	8.85	7.4	8.22
Operation ($)	494.23	492.01	492.03	493.8	492.82
OG BD Cost ($)	7.27	11.25	11.2	8.09	9.27
Updated Total ($)	501.5	503.26	503.23	501.89	502.09
Solving time (s)	8.39	4.99	9	6.73	6.72

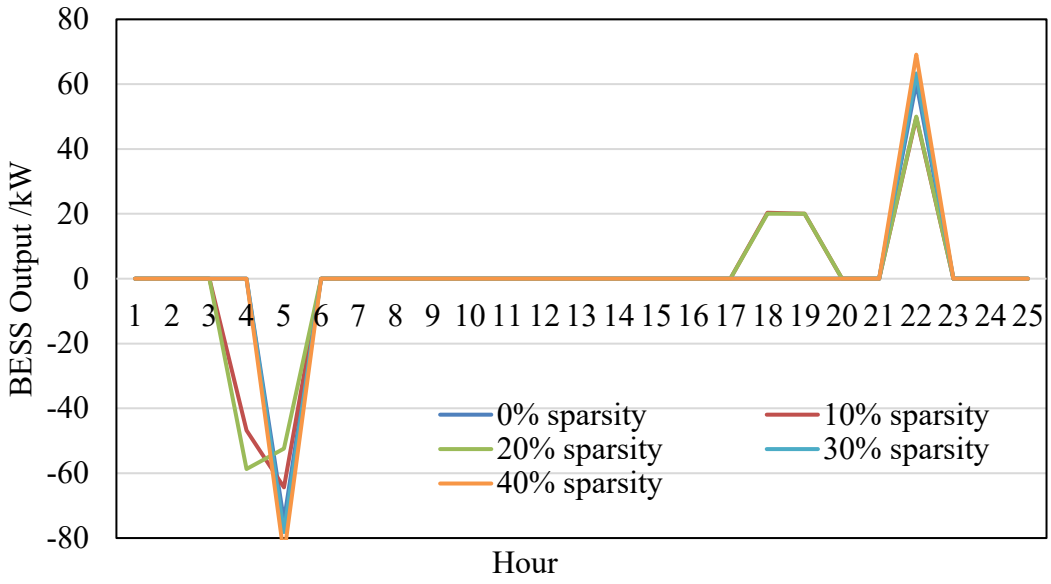

Fig. 6.10. BESS output in a microgrid system.

6.3.5 Bulk Power System Test Case

The SNNBD integrated day-ahead scheduling problem is evaluated at the bulk power grid model that has been tested in Chapter 5. A typical IEEE 24-bus system (Fig. 6.11) [99] is employed as a test bed. This system consists of 33 generators and serves as a representative model for large-scale power grids. In

addition to the existing infrastructure, the test bed incorporates several BESSs and wind farms to evaluate their impact on the day-ahead scheduling. Fig. 6.11 illustrates the layout of the IEEE 24-bus system, showcasing the interconnected buses and the corresponding transmission lines. The objective of this evaluation is to optimize the scheduling decisions considering the presence of the multiple BESS and wind farm within the larger power grid system.

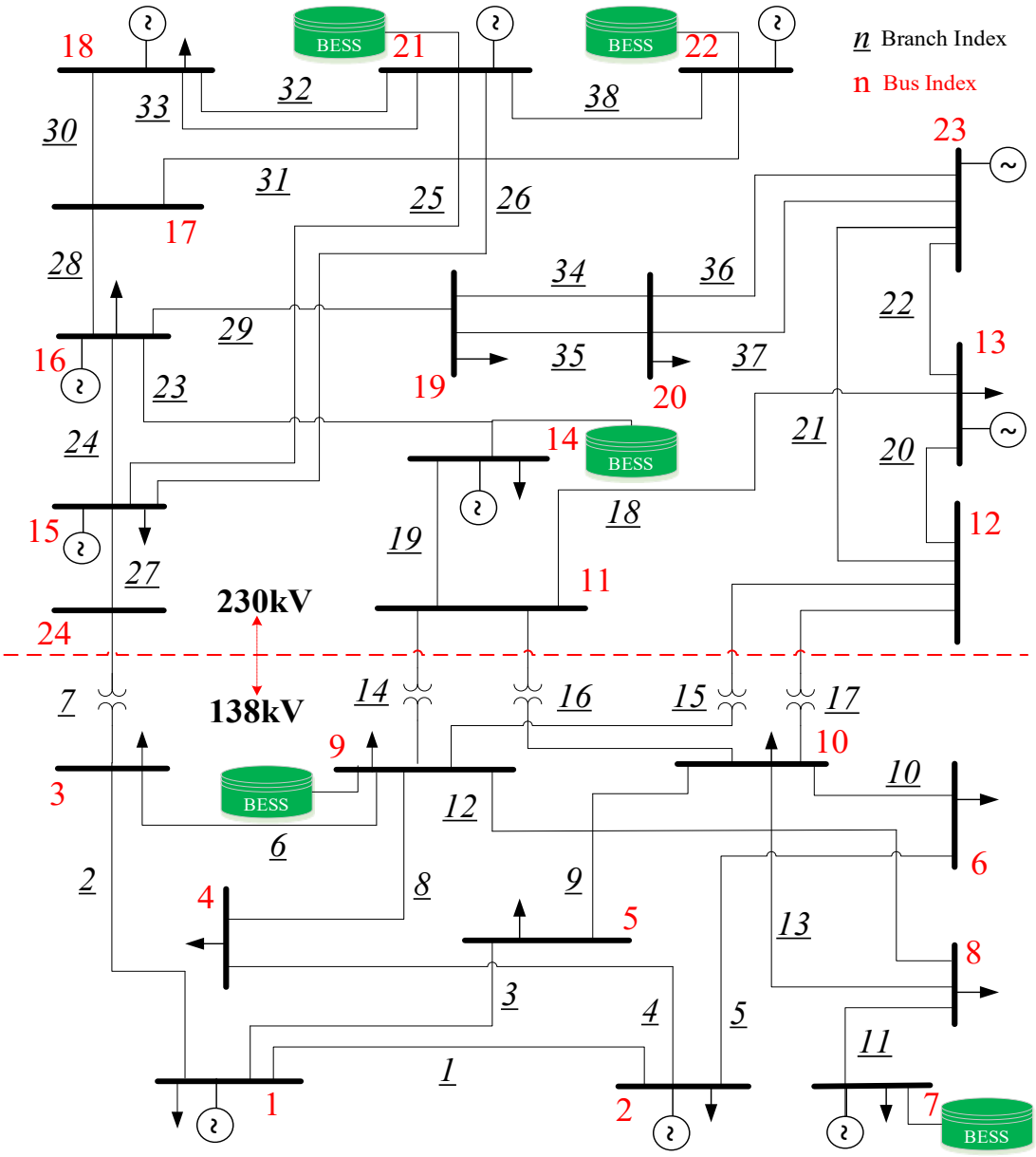

Fig. 6.11. Illustration of the modified IEEE 24-bus system [99].

The outcome for the IEEE 24-bus system with different sparsity levels of the SNNBD model are presented in Table 6.7. It is vital to recognize that all tabulated results are anchored on a relative MipGap of 0.001, which is a critical gauge of the optimality gap. The table clearly demonstrates that the solving time decreases

exponentially as the sparsity level of the SNNBD model. The results based on the 60% and 70% sparsity have not been included as the BESS output curve deviates significantly from the solutions based on lower sparsity level models. The 0% and 10% sparsity models results are not listed here since they cannot be solved within the given time frame, whereas the 50% sparsity model requires only 455 seconds for solution. Similarly, for the 20% sparsity model, the day-ahead scheduling problem cannot find the optimal solution within the span of 20 hours, resulting in a reported non-optimal benchmark result.

We also found that the 50% sparsity model lead to the minimum total cost. However, the total cost, does not change significantly despite the variation in solving time. This indicates that while the solving time is reduced to an acceptable number with high sparsity SNNBD models, the overall cost remains relatively stable. By analyzing these results, it becomes evident that increasing the sparsity level in the SNNBD model significantly reduces solving time without significantly impacting the overall cost. However, it is crucial to validate the BESS power output pattern when assessing the performance of the SNNBD model. Examining the BESS power output pattern ensures that the model captures the desired behavior and produces outputs consistent with expectations.

Figs. 6.12 and 6.13 display the SOC curves of BESS #4 and #5 under different sparsity levels of the proposed SNNBD model. These two BESS units are particularly active among the five units considered in the testbed. For benchmarking purposes, the SOC curve is also plotted when there is no battery degradation

considered in the day-ahead scheduling problem. The SOC curve provides insights into the utilization of the BESS, with more fluctuation indicating more active and flatter curves indicating less active. When degradation is not considered, the BESS units are utilized to their maximum capacity since there is no equivalent degradation cost factored into the optimization problem. We found that both BESS #4 and #5 are scheduled to discharge to 0% SOC twice when degradation is not considered. In Figure 6.12, the output curves of BESS #4 with SNNBD models significantly shrink compared to the case where degradation is not considered. However, the output patterns of BESS #4 with different sparsity levels of the SNNBD model exhibit a similar pattern and overlap for most time periods, which demonstrating the effectiveness of the proposed SNNBD model.

Table 6.7 IEEE 24 bus day-ahead scheduling results with different SNNBD models

Sparsity Percentage	Operation Cost ($)	Degradation Cost ($)	Updated Total ($)	Time (s)
20%	259,435	9,933	269,368	72,000
30%	259,848	10,447	270,295	4,383
40%	260,186	9,806	269,992	1,858
50%	259,472	6,789	266,261	455

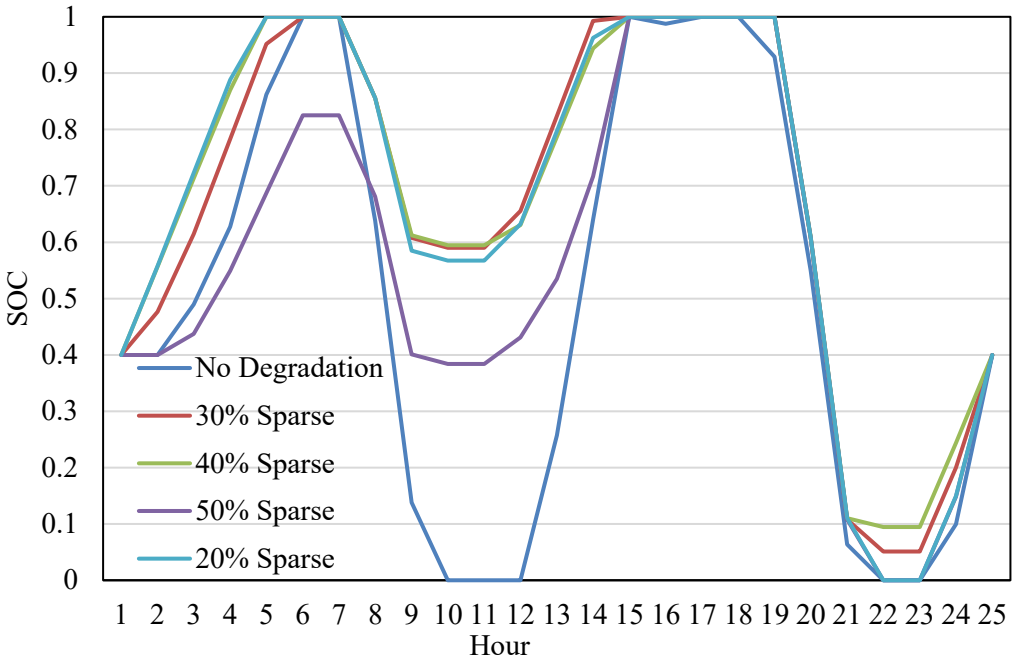

Fig. 6.12. SOC curves of BESS #4 in the 24-bus bulk power system.

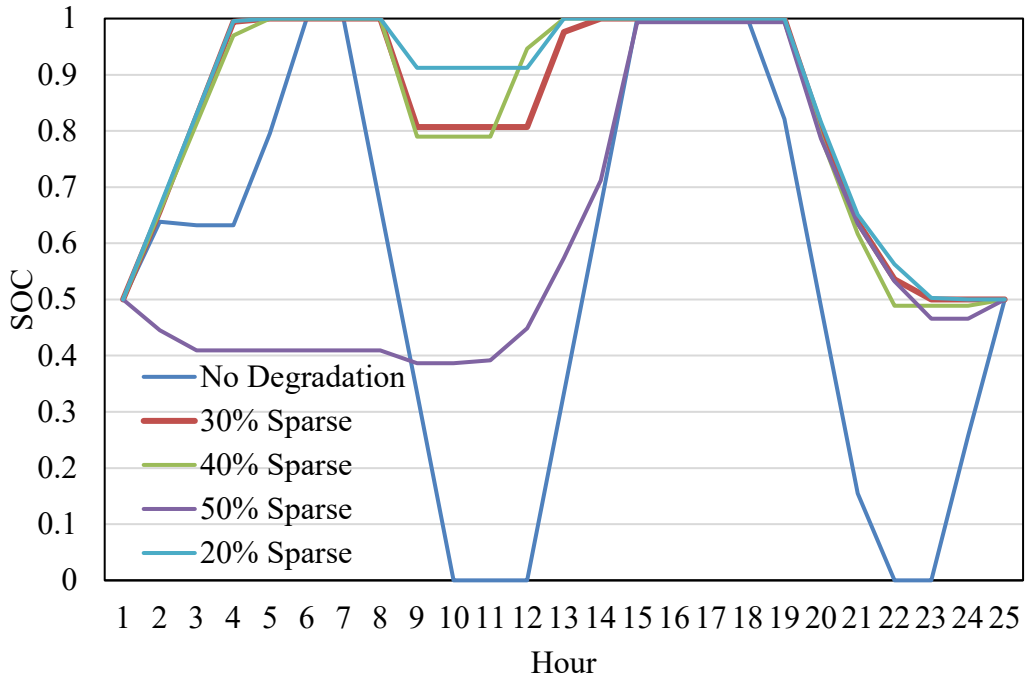

Fig. 6.13. SOC curves of BESS #5 in the 24-bus bulk power system.

6.3.6 Market Analysis

Fig. 6.14 presents sample results demonstrating the influence of locational marginal price (LMP) when integrating BESSs into the bulk power system. Our exploration encompassed 3 models including “no BESS model”, “BESS considered with degradation”, and “BESS considered without degradation”. A comparison was made with the "no BESS model" to assess the system's ability to reduce line congestion when a BESS is integrated. The LMP results in Fig. 7 specifically focus on bus 14, the location of the largest BESS unit, BESS #4. From the figure, it is evident that during most time periods, such as 1 am to 5 am and 12 pm to 6 pm, the LMP values are consistent across the different cases, indicating there is no line congestion at bus 14 during those periods. However, as the clock strikes 3 pm to 6 pm, a surge in LMP is evident, which suggests that the line is loaded higher than in the previous hours but is not yet congested. During the normal daily peak load periods of 7 am to 9 am and 7 pm to 8 pm, the LMP values differ among the proposed models. In comparison to the "no BESS model," the models with integrated BESS units can significantly reduce the LMP, indicating that the BESS can alleviate line congestion. Note that when battery degradation is not considered, the BESS exhibits a higher capability to mitigate line congestion, leading to the lowest LMP during those congested hours. This analysis of LMP with the integration of a BESS system provides valuable insights for both grid operators and BESS investors, as BESS installations play a crucial role in addressing line congestion within the grid.

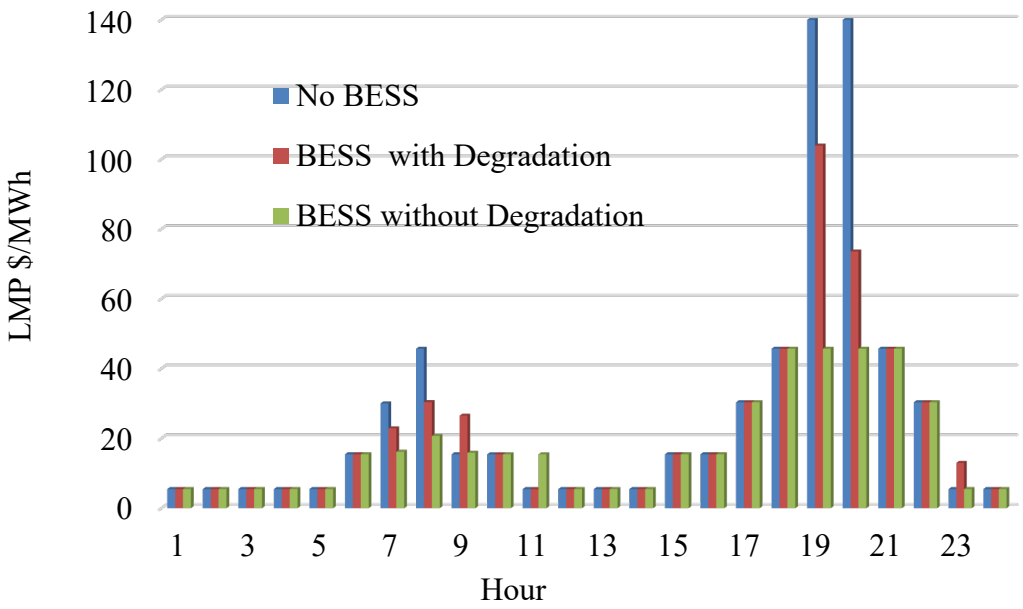

Fig. 6.14. LMP at bus 14 (BESS #4).

6.3.7 Sensitivity Analysis of Relative Optimization Gaps

A sensitivity test was conducted to examine the impact of different relative gaps. Fig. 6.15 displays SOC curves of BESS #4 based on the optimal solution obtained using different relative MipGap values. The results presented in Figure 8 are based on the 50% sparsity SNNBD model. The solving times for MipGap values of 0.01, 0.005, and 0.001 are 339 seconds, 380 seconds, and 450 seconds, respectively. The solving time increases as the MipGap value decreases because a more accurate optimal solution is sought. However, upon analyzing the SOC curve depicted in Figure 8, it becomes evident that the SOC curves mostly overlap, indicating minimal differences between the solutions obtained under different MipGap values. Consequently, for the 50% sparsity model, a higher MipGap value is preferred as it reduces the computation time while maintaining a comparable solution quality.

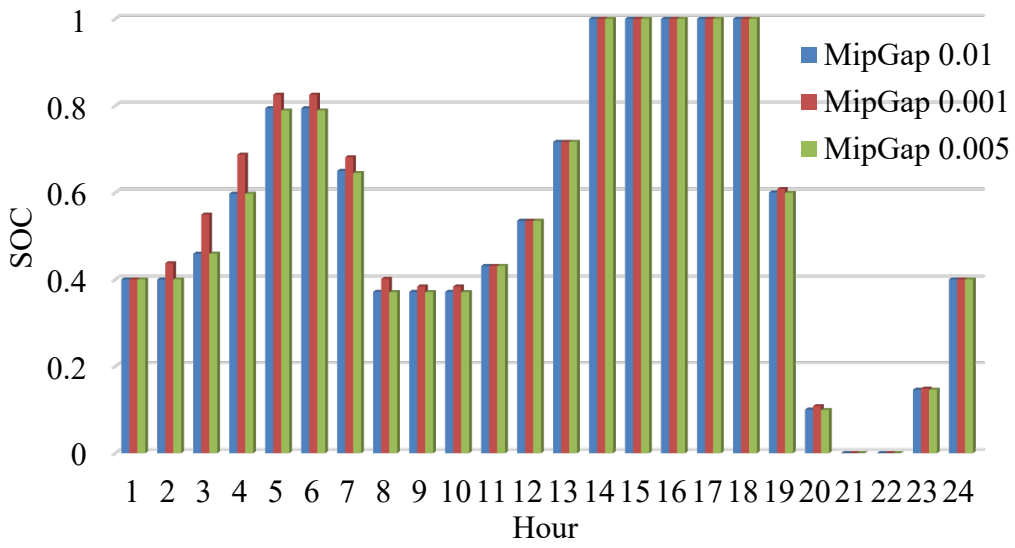

Fig. 6.15. Scheduled SOC levels of BESS #4 at bus 14.

6.4 Summary

This chapter proposes two choices to enhance the computational efficiency BDMDS model. The first choice investigated four innovative linearization models designed to tackle the challenges caused by the ReLU activation function in neural networks when integrated into optimization models where a subset of decision variables serve as the input features of the learning model. The inherent non-linearity of the ReLU function often makes such models complex and difficult to solve directly. Our results highlight that the choice of penalty terms is pivotal in obtaining optimal solutions for P-CTAR and PCAR models. While CTAR and PCAR may not deliver perfect performance in the NNBD-integrated microgrid testbed, they remain viable options for modeling and solving this class of problems. It's important to emphasize that when changes are made to the optimization model, the performance of the proposed linearization models should be re-evaluated.

Secondly, a novel sparse neural network-based battery degradation model that can accurately quantify battery degradation in BESS and largely address the computational challenges associated with traditional dense neural networks when being incorporated into optimization models. The results also show that our proposed SNNBD model can significantly reduce the computational burden, making neural network-integrated day-ahead energy scheduling directly solvable, even for complicated multi-BESS integrated systems. Furthermore, the results have been proven to be accurate and feasible with a high sparsity SNNBD model in both microgrid and bulk power system. Choosing different sparsity levels for the proposed SNNBD model provides flexibility for the grid operator, as it involves a tradeoff between accuracy and solving time. Overall, the SNNBD model opens up new possibilities for efficiently addressing battery degradation in day-ahead energy scheduling for multi-BESS systems.

7. CONCLUSION AND FUTURE WORK

This dissertation has delved into the realm of optimal energy management strategies for BESS-integrated microgrids, addressing both grid-connected and isolated microgrid settings. The overarching motivation behind this research lies in the escalating integration of renewable energy sources, characterized by their inherent variability, which poses significant challenges to maintaining grid stability. Additionally, the work extends its reach to tackle the formidable issue of battery degradation prediction, and its seamless integration into microgrid scheduling. This holistic approach contributes to enhancing the economic and operational feasibility of microgrid systems in an era of transition toward cleaner and more sustainable energy solutions.

7.1 Contributions

In Chapter 2, we have explored innovative strategies for grid-connected microgrids, effectively harnessing BESS to counteract renewable energy source fluctuations and fortify microgrids as grid-friendly entities. Furthermore, the research has laid the foundation for microgrids to serve as valuable contributors to the larger grid, offering flexible grid-microgrid power exchange and thereby bolstering grid support capabilities.

Shifting our focus to isolated microgrids, Chapter 3 introduces groundbreaking economic analysis of OHRES model that can power offshore platforms with zero carbon emissions. The incorporation of three resilience models, intertwined with BESS and/or HESS, results in heightened system reliability. The

development of a resilience index, known as the microgrid survivability rate (SR), offers a valuable metric to gauge system robustness. The innovative Resilient Operational Planning (ROP) algorithm further optimizes SR, particularly during extreme events.

Chapter 4 introduces a data-driven method for predicting battery degradation within scheduled battery operational profiles. The neural network-based battery degradation (NNBD) model provides a comprehensive framework for quantifying degradation based on key factors, which is then integrated into microgrid day-ahead scheduling, creating a battery degradation-based MDS (BDMDS) model. This enhancement ensures that the equivalent battery degradation cost is accurately considered in scheduling, leading to more economically viable microgrid operations. The hierarchical deep learning-based battery degradation quantification (HDL-BDQ) model furthers the precision of battery degradation predictions, elevating the quality of decision-making in microgrid management.

Recognizing the nonlinear complexities introduced by the NNBD model, Chapter 5 undertakes the challenging task of linearization. By converting nonlinear activation functions into linear constraints, the research presents the linearized BD-SCUC (L-BD-SCUC) model, transforming the battery degradation-based security-constrained unit commitment problem into a more tractable form. Case studies reveal that the L-BD-SCUC model can efficiently address multi-BESS power system day-ahead scheduling, optimizing total costs while accounting for equivalent degradation costs.

Finally, Chapter 6 highlights the importance of computational efficiency in addressing the NNBD-embedded optimization problem within microgrid day-ahead scheduling. Innovative solutions, including methods for linearizing rectified linear units (ReLU) and introducing sparse neural network structures, are presented to reduce computational complexity. These enhancements make microgrid scheduling not only more practical but also more cost-effective, thereby ensuring the real-world viability of the proposed solutions.

7.2 Future Work

Future work can focus on several key areas to enhance the research. First, exploring grid-integrated battery operational profile-based aging tests with an LSTM model to predict the grid size BESS degradation. Second, we will try to implement transfer learning techniques for different battery types, could improve predictive accuracy and reduce the data requirement for training and testing for different types of BESS. Our proposed NNBD model is feasible to different battery types as long as the battery data is available. Additionally, further research can delve into the impact of BESS on power energy markets, considering factors such as LMP, load payments, generator costs, revenues, congestion costs, and reserve costs. This would provide a comprehensive understanding of the economic implications and market dynamics associated with BESS integration into the power grid. Moreover, investigating the potential of applying similar approaches to Hydrogen Energy Storage Systems (HESS) could yield valuable insights into their performance and aging characteristics.

7.3 List of Publications

(1) Cunzhi Zhao and Xingpeng Li, "A Novel Real-Time Energy Management Strategy for Grid-Friendly Microgrid: Harnessing Internal Fluctuation Internally," *The 52nd North American Power Symposium (NAPS),* Tempe, AZ, USA, Apr, 2021.

(2) Cunzhi Zhao and Xingpeng Li, "A Novel Real-Time Energy Management Strategy for Grid-Supporting Microgrid: Enabling Flexible Trading Power," *IEEE PES General Meeting 2021*, Washington, DC, USA, Jul. 2021.

(3) Praveen Dhanasekar, Cunzhi Zhao and Xingpeng Li, "Quantitative Analysis of Demand Response Using Thermostatically Controlled Loads," *IEEE PES Innovative Smart Grid Technology*, New Orleans, LA, USA, Apr. 2022.

(4) Cunzhi Zhao and Xingpeng Li, "An Alternative Method for Solving Security-Constraint Unit Commitment with Neural Network Based Battery Degradation Model," *54th North American Power Symposium*, Salt Lake City, UT, USA, Oct. 2022.

(5) Cunzhi Zhao and Xingpeng Li, "A 100% Renewable Energy System: Enabling Zero CO2 Emission Offshore Platforms," *54th North American Power Symposium*, Salt Lake City, UT, USA, Oct. 2022.

(6) Cunzhi Zhao, Jesus Silva-Rodriguez and Xingpeng Li, "Resilient Operational Planning for Microgrids Against Extreme Events," *Hawaii International Conference on System Sciences*, Maui, Hawaii, USA, Jan. 2023.

(7) Cunzhi Zhao and Xingpeng Li, "Microgrid Optimal Energy Scheduling Considering Neural Network based Battery Degradation," *IEEE Transactions on Power Systems*, early access, Jan. 2023.

(8) Ali Siddique, Cunzhi Zhao, and Xingpeng Li, "Microgrid Optimal Energy Scheduling with Risk Analysis," *Texas Power and Energy Conference*, College Station, TX, USA, Feb. 2023.

(9) Cunzhi Zhao, Xingpeng Li, and Yan Yao, "Quality Analysis of Battery Degradation Models with Real Battery Aging Experiment Data," *Texas Power and Energy Conference*, College Station, TX, USA, Feb. 2023.

REFERENCES

[1] E. Denny and M. O'Malley, "Wind generation, power system operation, and emissions reduction," in *IEEE Transactions on Power Systems*, vol. 21, no. 1, pp. 341-347, Feb. 2006.

[2] Q. Jiang, M. Xue, and G. Geng, "Energy management of microgrid ingrid-connected and stand-alone modes," *IEEE Transactions on Power Systems*, vol. 28, pp. 3380–3389, August, 2013.

[3] X. Li, G. Geng, and Q. Jiang, "A hierarchical energy management strategy for grid-connected microgrid," *IEEE PES General Meeting,* National Harbor*, MD*, pp. 1–5, July, 2014.

[4] B. Li, T.Chen, X. Wang and G. Giannakis, "Real-Time Energy Management in Microgrids With Reduced Battery Capacity Requirements," *IEEE Trans. Smart Grid*, vol. 10, no. 2, pp. 1928–1938, Mar. 2019.

[5] White House, The Long-term Strategy of the UNITED STATES, 2021 [Online]. Available: www.whitehouse.gov.

[6] N. Nikmehr and S. N. Ravadanegh, "Optimal power dispatch of multimicrogrids at future smart distribution grids," *IEEE Transactions on Smart Grid*, vol. 6, pp. 1648–1657, July, 2015.

[7] M. T. Lawder, B. Suthar, P. W. C. Northrop, S. De, C. M. Hoff, O. Leitermann, M.L. Crow, S. Santhanagopalan and V. R. Subramanian, "Battery Energy Storage System (BESS) and Battery Management System (BMS) for Grid-Scale

Applications," in *Proceedings of the IEEE*, vol. 102, no. 6, pp. 1014-1030, June 2014.

[8] Z. Lyu, R. Gao, and L. Chen, "Li-Ion Battery State of Health Estimation and Remaining Useful Life Prediction Through a Model-Data-Fusion Method," *IEEE Transactions on Power Electronics*, vol. 36, no. 6, pp. 6228–6240, June. 2021.

[9] T. Mai, M. M. Hand, S. F. Baldwin, R. H. Wiser, G. L. Brinkman, P. Denholm, D. J. Arent, G. Porro, D. Sandor, D. J. Hostick, M. Milligan, E. A. DeMeo and M. Bazilian, "Renewable Electricity Futures for the United States," in *IEEE Transactions on Sustainable Energy*, vol. 5, no. 2, pp. 372-378, April 2014.

[10] Y. Ji, J. Wang, J. Xu, X. Fang, and H. Zhang, "Real-time energy management of a microgrid using deep reinforcement learning," *Energies*, vol. 12, pp. 2291–3212, June, 2019.

[11] N. Hatziargyriou, H. Asano, R. Iravani, and C. Marnay, "Microgrid," *IEEE Power and Energy Magazine*, vol. 5, pp. 78–94, July, 2007.

[12] B. Moran, "Microgrid load management and control strategies," *IEEE/PES Transmission and Distribution Conference and Exposition*, pp. 1– 4, May, 2016.

[13] J. Liu, H. Chen, W. Zhang, B. Yurkovich, and G. Rizzoni, "Energy management problems under uncertainties for grid-connected microgrids: a chance constrained programming approach," *IEEE Transactions on Smart Grid*, vol. 8, pp. 2585–2596, November, 2017.

[14] P. Zeng, H. Li, H. He, and S. Li, "Dynamic energy management of a microgrid using approximate dynamic programming and deep recurrent neural network learning," *IEEE Transactions on Smart Grid*, vol. 10, pp. 4435–4445, July, 2019.

[15] R. Palma-Behnke, C. Benavides, F. Lanas, B. Severino, L. Reyes, J. Llanos, and D. S´aez, "A microgrid energy management system based on the rolling horizon strategy," *IEEE Transactions on Smart Grid*, vol. 4, June, 2013.

[16] A. F. Penaranda, P. E. Mosquera and S. F. Contreras, "Planning Model of Microgrids for the Supply of Ancillary Services to the Utility Grid," in *IEEE Milan PowerTech*, Milan, Italy, Jun 2019.

[17] A. Majzoobi and A. Khodaei, "Application of Microgrids in Supporting Distribution Grid Flexibility," *IEEE Transactions on Power Systems*, vol. 32, no. 5, pp. 3660-3669, Sep 2017.

[18] H. Kanchev, D. Liu, F. Colas, V. Lazarov and B. Francois, "Energy Management and Operational Planning of a Microgrid With a PV-Based Active Generator for Smart Grid Applications," *IEEE Transactions on Industrial Electronics*, vol. 58, no. 10, pp. 4583-4592, 2011.

[19] M. T. Lawder, B. Suthar, P. W. Northrop, S. De, M. Hoff, O. Leitermann, M. L. Crow, S. Santhanagopalan and V. R. Subramanian, "Battery Energy Storage System (BESS) and Battery Management System (BMS) for Grid-Scale Applications," *Proceedings of the IEEE*, vol. 102, no. 6, pp. 1014-1030, Jun 2014.

[20] A. Parisio, E. Rikos and L. Glielmo, "A Model Predictive Control Approach to Microgrid Operation Optimization," *IEEE Transactions on Control System Technology*, vol. 22, no. 5, pp. 1813-1827, 2014.

[21] R. Palma-Behnke, C. Benavides, F. Lanas, B. Severino, L. Reyes, J. Llanos and D. Saez, "A Microgrid Energy Management System Based on the Rolling Horizon Strategy," *IEEE Transactions on Smart Grid*, vol. 4, no. 2, pp. 996-1006, June 2013.

[22] Dataport Resources, May, 2019. [online] Available: https://dataport.pecanstreet.org/academic.

[23] A. Sudhamshu, M. C. Pandey, N. Sunil, N. Satish and V. Mugundhan, "Numerical Study of effect of pitch angle onperformance characteristics of a HAWT," *Engineering Science and Technology, an International Journal,* vol. 19, no. 1, pp. 632-641, Aug, 2015.

[24] U.S. Energy Information Administration, "Gulf Of Mexico Fact Sheet," [Online]. Available at: https://www.eia.gov/special/gulf_of_mexico/

[25] BBC Future, Future Planet | Oceans, "The new use for abandoned oil rigs," [Online]. Available at: https://www.bbc.com/future/article/20210126-the-richest-human-made-marine-habitats-in-the-world

[26] GTM, "Oil and Gas Companies Can Power Offshore Platforms with Renewables," [Online]. Available at: https://www.greentechmedia.com/articles/read/oil-and-gas-companies-can-power-offshore-platforms-with-renewables

[27] Walt Musial, Donna Heimiller, Philipp Beiter, George Scott, and Caroline Draxl, National Renewable Energy Laboratory, “2016 Offshore Wind Energy Resource Assessment for the United States,” Technical Report NREL/TP-5000-66599, Sep. 2016.

[28] Y. Fu, Y. Liu, L. -l. Huang, F. Ying and F. Li, "Collection System Topology for Deep-Sea Offshore Wind Farms Considering Wind Characteristics," in *IEEE Transactions on Energy Conversion*, vol. 37, no. 1, pp. 631-642, March 2022.

[29] M. de Prada, L. Igualada, C. Corchero, O. Gomis-Bellmunt and A. Sumper, "Hybrid AC-DC Offshore Wind Power Plant Topology: Optimal Design," *IEEE Transactions on Power Systems*, vol. 30, no. 4, pp. 1868-1876, July 2015.

[30] Q. Wang, Z. Yu, R. Ye, Z. Lin and Y. Tang, "An Ordered Curtailment Strategy for Offshore Wind Power Under Extreme Weather Conditions Considering the Resilience of the Grid," in *IEEE Access*, vol. 7, pp. 54824-54833, 2019.

[31] He W, Jacobsen G, Anderson T, Olsen FG, Hanson TD, Korpås M, Toftevaag T, Eek J, Uhlen K, Johansson E. “The potential of integrating wind power with offshore oil and gas platforms,” *Wind Engineering*, vol. 34, pp. 125–137, 2010.

[32] US White House, “FACT SHEET: Biden Administration Jumpstarts Offshore Wind Energy Projects to Create Jobs,” [Online]. Available at: https://www.whitehouse.gov/briefing-room/statements-releases/2021/03/29/fact-sheet-biden-administration-jumpstarts-offshore-wind-energy-projects-to-create-jobs/

[33] D. Hu, X. Zhao, Xu Cai and Jianfeng Wang, “Impact of wind power on stability of offshore platform power systems,” *2008 Third International Conference on Electric Utility Deregulation and Restructuring and Power Technologies*, pp. 1688-1692, 2008.

[34] H. G. Svendsen, M. Hadiya, E. V. Øyslebø and K. Uhlen, “Integration of offshore wind farm with multiple oil and gas platforms,” *2011 IEEE Trondheim PowerTech*, pp. 1-3, 2011.

[35] M. Korpas, L. Warland, W. He, and J. Tande, "A Case-Study on Offshore Wind Power Supply to Oil and Gas Rigs," in *Energy Procedia*, vol 24, pp. 18-26, 2012.

[36] G. Shi, S. Peng, X. Cai, Z. Chen and W. He, “Grid integration of offshore wind farms and offshore oil/gas platforms,” *Proceedings of The 7th International Power Electronics and Motion Control Conference*, 2012, pp. 1301-1305.

[37] J. Zhang, X. Xie, J. Wang, C. Wei and G. Liu, "Modeling and analysis of independent offshore platforms micro-grid," *2011 4th International Conference on Electric Utility Deregulation and Restructuring and Power Technologies (DRPT)*, 2011, pp. 1479-1484.

[38] U.S. Energy Information Administration, “TODAY IN ENERGY - Most planned U.S. battery storage additions in next three years to be paired with solar,” [Online]. Available at: https://www.eia.gov/todayinenergy/detail.php?id=49756.

[39] European Commission, "Communication From The Commission To The European Parliament, The Council, The European Economic And Social Committee And The Committee Of The Regions - A Hydrogen Strategy For A Climate-Neutral Europe," Aug. 2020. [Online]. Available at: https://ec.europa.eu/info/index_en

[40] A. Zhang, H. Zhang, M. Qadrdan, and W. Yang, "Optimal Planning of Integrated Energy Systems for Offshore Oil Extraction and Processing Platforms," *Energies*, vol. 12, no. 4, p. 756, Feb. 2019.

[41] WINDY.App, "Gulf of mexico: weather statistics and wind history," Jul, 2022, [Online] Available at: https://windy.app/forecast2/spot/634466/Gulf+of+mexico.

[42] J. Silva-Rodriguez and X. Li, "Water-Energy Co-Optimization for Community-Scale Microgrids," *IEEE 53rd North American Power Symposium*, College Station, TX, USA, Nov. 2021.

[43] C. Zhao and X. Li, "A Novel Real-Time Energy Management Strategy for Grid-Supporting Microgrid: Enabling Flexible Trading Power," 2021 *IEEE Power & Energy Society General Meeting (PESGM)*, 2021, pp. 1-5.

[44] P. Dhanasekar, C. Zhao and X. Li, "Quantitative Analysis of Demand Response Using Thermostatically Controlled Loads," *IEEE PES Innovative Smart Grid Technology*, New Orleans, LA, USA, Apr. 2022.

[45] A. Hussain, V. Bui, H. Kim, "Microgrids as a resilience resource and strategies used by microgrids for enhancing resilience," *Applied Energy*, vol. 240, 2019, pp. 59-72.

[46] J. M. Fife, M. Scharf, S. G. Hummel and R. W. Morris, "Field reliability analysis methods for photovoltaic inverters," *2010 35th IEEE Photovoltaic Specialists Conference*, 2010, pp. 002767-002772.

[47] M. Sandelic, S. Peyghami, A. Sangwongwanich, F. Blaabjerg, "Reliability aspects in microgrid design and planning: Status and power electronics-induced challenges," *Renewable and Sustainable Energy Reviews*, vol. 159, 2022.

[48] S. Mishra, T. Kwasnik, K. Anderson, "Microgrid Resilience: A Holistic and Context-Aware Resilience Metric," *Energy Systems*, Mar. 2022.

[49] S. Mishra, K. Anderson, B. Miller, K. Boyer, A. Warren, "Microgrid resilience: A holistic approach for assessing threats, identifying vulnerabilities, and designing corresponding mitigation strategies," *Applied Energy*, vol. 264, 2020

[50] J. Nelson, N. G. Johnson, K. Fahy, T. A. Hansen, "Statistical development of microgrid resilience during islanding operations," *Applied Energy*, vol. 279, 2020.

[51] A. Hussain, V. Bui and H. Kim, "A Proactive and Survivability-Constrained Operation Strategy for Enhancing Resilience of Microgrids Using Energy Storage System," *IEEE Access*, vol. 6, pp. 75495-75507, 2018.

[52] W. Zhong, L. Wang, Z. Liu and S. Hou, "Reliability Evaluation and Improvement of Islanded Microgrid Considering Operation Failures of Power

Electronic Equipment," *Journal of Modern Power Systems and Clean Energy*, vol. 8, no. 1, pp. 111-123.

[53] L. Zhang, N. Gari, L. V. Hmurcik, "Energy management in a microgrid with distributed energy resources," *Energy Conversion and Management*, vol. 78, pp. 297-305, 2014.

[54] C. Zhao and X. Li, "A Novel Real-Time Energy Management Strategy for Grid-Friendly Microgrid: Harnessing Internal Fluctuation Internally," *52nd North American Power Symposium*, Tempe, AZ, USA, Apr, 2021.

[55] A. M. Abomazid, N. A. El-Taweel and H. E. Z. Farag, "Optimal Energy Management of Hydrogen Energy Facility Using Integrated Battery Energy Storage and Solar Photovoltaic Systems," in *IEEE Transactions on Sustainable Energy*, vol. 13, no. 3, pp. 1457-1468.

[56] X. Gong, R. Xiong and C. C. Mi, "Study of the Characteristics of Battery Packs in Electric Vehicles With Parallel-Connected Lithium-Ion Battery Cells," in *IEEE Transactions on Industry Applications*, vol. 51, no. 2, pp. 1872-1879, March-April 2015.

[57] B. Xu, A. Oudalov, A. Ulbig, G. Andersson and D. Kirschen, "Modeling of lithium-ion battery degradationfor cell life assessment," *2017 IEEE Power & Energy Society General Meeting*, 2017, pp. 1-1.

[58] X. Han, L. Lu, Y. Zheng, X. Feng, Z. Li, J. Li, M. Ouyang, "A review of the key issues of the lithium ion battery degradation among the whole life cycle," in *eTransportation*, vol 1, Jul. 2019.

[59] P. S. Kumar, R. P. S. Chandrasena, V. Ramu, G. N. Srinivas and K. V. S. M. Babu, "Energy Management System for Small Scale Hybrid Wind Solar Battery Based Microgrid," in *IEEE Access*, vol. 8, pp. 8336-8345, 2020.

[60] A. Merabet, K. Tawfique Ahmed, H. Ibrahim, R. Beguenane and A. M. Y. M. Ghias, "Energy Management and Control System for Laboratory Scale Microgrid Based Wind-PV-Battery," in *IEEE Transactions on Sustainable Energy*, vol. 8, no. 1, pp. 145-154, Jan. 2017.

[61] X. Xing, L. Xie, H. Meng, X. Guo, L. Yue and J. M. Guerrero, "Energy management strategy considering multi-time-scale operational modes of batteries for the grid-connected microgrids community," in *CSEE Journal of Power and Energy Systems*, vol. 6, no. 1, pp. 111-121, March 2020.

[62] K. Thirugnanam, S. K. Kerk, C. Yuen, N. Liu and M. Zhang, "Energy Management for Renewable Microgrid in Reducing Diesel Generators Usage With Multiple Types of Battery," in *IEEE Transactions on Industrial Electronics*, vol. 65, no. 8, pp. 6772-6786, Aug. 2018.

[63] Z. Miao, L. Xu, V. R. Disfani and L. Fan, "An SOC-Based Battery Management System for Microgrids," in *IEEE Transactions on Smart Grid*, vol. 5, no. 2, pp. 966-973, March 2014.

[64] B. Li, T. Chen, X. Wang and G. B. Giannakis, "Real-Time Energy Management in Microgrids With Reduced Battery Capacity Requirements," in *IEEE Transactions on Smart Grid*, vol. 10, no. 2, pp. 1928-1938, March 2019.

[65] C. Zhao and X. Li, "A Novel Real-Time Energy Management Strategy for Grid-Supporting Microgrid: Enabling Flexible Trading Power," *IEEE PES General Meeting*, (Virtually), Washington D.C., USA, Jul. 2021.

[66] C. Ju, P. Wang, L. Goel and Y. Xu, "A Two-Layer Energy Management System for Microgrids With Hybrid Energy Storage Considering Degradation Costs," in *IEEE Transactions on Smart Grid*, vol. 9, no. 6, pp. 6047-6057, Nov. 2018.

[67] B. Foggo and N. Yu, "Improved Battery Storage Valuation Through Degradation Reduction," in *IEEE Transactions on Smart Grid*, vol. 9, no. 6, pp. 5721-5732, Nov. 2018.

[68] L. Zhang, Y. Yu, B. Li, X. Qian, S. Zhang, X. Wang, X. Zhang and M. Chen, "Improved Cycle Aging Cost Model for Battery Energy Storage Systems Considering More Accurate Battery Life Degradation," in *IEEE Access*, vol. 10, pp. 297-307, 2022.

[69] M. Sandelic, A. Sangwongwanich and F. Blaabjerg, "Incremental Degradation Estimation Method for Online Assessment of Battery Operation Cost," in *IEEE Transactions on Power Electronics*, vol. 37, no. 10, pp. 11497-11501, Oct. 2022.

[70] Y. Shi B. Xu, Y. Tan and B. Zhang, "A Convex Cycle-based Degradation Model for Battery Energy Storage Planning and Operation," *2018 Annual American Control Conference (ACC)*, 2018.L.

[71] L. De Pascali, F. Biral and S. Onori, "Aging-Aware Optimal Energy Management Control for a Parallel Hybrid Vehicle Based on Electrochemical-

Degradation Dynamics," in *IEEE Transactions on Vehicular Technology*, vol. 69, no. 10, pp. 10868-10878, Oct. 2020.

[72] J. Cao, D. Harrold, Z. Fan, T. Morstyn, D. Healey and K. Li, "Deep Reinforcement Learning-Based Energy Storage Arbitrage With Accurate Lithium-Ion Battery Degradation Model," in *IEEE Transactions on Smart Grid*, vol. 11, no. 5, pp. 4513-4521, Sept. 2020.

[73] G. Abdelaal, M. I. Gilany, M. Elshahed, H. M. Sharaf and A. El'gharably, "Integration of Electric Vehicles in Home Energy Management Considering Urgent Charging and Battery Degradation," in *IEEE Access*, vol. 9, pp. 47713-47730, 2021.

[74] K. Abdulla, J. Hoog, V. Muenzel, F. Suits, K. Steer, A. Wirth and S. Halgamuge, "Optimal operation of energy storage systems considering forecasts and battery degradation," *2017 IEEE Power & Energy Society General Meeting*, 2017, pp. 1-1.

[75] K. Antoniadou-Plytaria, D. Steen, L. A. Tuan, O. Carlson and M. A. Fotouhi Ghazvini, "Market-Based Energy Management Model of a Building Microgrid Considering Battery Degradation," in *IEEE Transactions on Smart Grid*, vol. 12, no. 2, pp. 1794-1804, March 2021.

[76] J. -O. Lee, Y. -S. Kim, T. -H. Kim and S. -I. Moon, "Novel Droop Control of Battery Energy Storage Systems Based on Battery Degradation Cost in Islanded DC Microgrids," in *IEEE Access*, vol. 8, pp. 119337-119345, 2020.

[77] Cunzhi Zhao, Xingpeng Li, and Yan Yao, "Quality Analysis of Battery Degradation Models with Real Battery Aging Experiment Data," *Texas Power and Energy Conference 2023*, College Station, TX, USA, Feb. 2023.

[78] Z. Wei, Y. Li and L. Cai, "Electric Vehicle Charging Scheme for a Park-and-Charge System Considering Battery Degradation Costs," in *IEEE Transactions on Intelligent Vehicles*, vol. 3, no. 3, pp. 361-373, Sept. 2018.

[79] G. Saldaña, J. I. S. Martín, I. Zamora, F. J. Asensio, O. Oñederra and M. González, "Empirical Electrical and Degradation Model for Electric Vehicle Batteries," in *IEEE Access*, vol. 8, pp. 155576-155589, 2020.

[80] Y. Sun, H. Yue, J. Zhang and C. Booth, "Minimization of Residential Energy Cost Considering Energy Storage System and EV With Driving Usage Probabilities," in *IEEE Transactions on Sustainable Energy*, vol. 10, no. 4, pp. 1752-1763, Oct. 2019.

[81] H. Farzin, M. Fotuhi-Firuzabad and M. Moeini-Aghtaie, "A Practical Scheme to Involve Degradation Cost of Lithium-Ion Batteries in Vehicle-to-Grid Applications," in *IEEE Transactions on Sustainable Energy*, vol. 7, no. 4, pp. 1730-1738, Oct. 2016.

[82] S. Fang, B. Gou, Y. Wang, Y. Xu, C. Shang and H. Wang, "Optimal Hierarchical Management of Shipboard Multibattery Energy Storage System Using a Data-Driven Degradation Model," in *IEEE Transactions on Transportation Electrification*, vol. 5, no. 4, pp. 1306-1318, Dec. 2019.

[83] P. Attia, M. Deetjen, and J. Witmer. “Accelerating battery development by early prediction of cell lifetime,” (2018).

[84] P. Attia, A. Grover, N. Jin, K. A. Severson, T. M. Markov, Y. Liao, M. H. Chen, B. Cheong, N. Perkins, Z. Yang, P. K. Herring, M. Aykol, S. J. Harris, R. D. Braatz, S. Ermon and W. C. Chueh, “Closed-loop optimization of fast-charging protocols for batteries with machine learning,” in *Nature,* vol. 578**,** pp. 397–402, 2020.

[85] K. Severson, P. Attia, N. Jin, N. Perkins, B. Jiang, Z. Yang, M. H. Chen, M. Aykol, P. K. Herring, D. Fraggedakis, M. Z. Bazant, S. J. Harris, W. C. Chueh and R. D. Braatz, “Data-driven prediction of battery cycle life before capacity degradation,” in *Nature Energy*, vol. 4, pp 383–391, 2019.

[86] C. Zhao and Xingpeng Li, “A 100% Renewable Energy System: Enabling Zero CO2 Emission Offshore Platforms,” *54th North American Power Symposium*, Salt Lake City, UT, USA, Oct. 2022.

[87] C. Zhao, J. Silva-Rodriguez and Xingpeng Li, “Resilient Operational Planning for Microgrids Against Extreme Events,” *Hawaii International Conference on System Sciences*, Maui, Hawaii, USA, Jan. 2023.

[88] Gang Shi, Simin Peng, Xu Cai, Z. Chen and Wei He, “Grid integration of offshore wind farms and offshore oil/gas platforms,” *Proceedings of The 7th International Power Electronics and Motion Control Conference*, 2012, pp. 1301-1305.

[89] B. Xu, A. Oudalov, A. Ulbig, G. Andersson and D. S. Kirschen, "Modeling of Lithium-Ion Battery Degradation for Cell Life Assessment," in *IEEE Transactions on Smart Grid*, vol. 9, no. 2, pp. 1131-1140, March 2018.

[90] "Battery Archive," [Online]. Available at: https://www.batteryarchive.org/

[91] Omar N., M. A. Monem, Y. Firouz, J. Salminen, J. Smekens, O. Hegazy, H. Gaulous, G. Mulder, P. Van den Bossche, T. Coosemans, and J. Van Mierlo. "Lithium iron phosphate based battery — Assessment of the aging parameters and development of cycle life model," *Applied Energy*, Vol. 113, January 2014, pp. 1575–1585.

[92] S. Saxena, C. Floth, J. MacDonald. S. Moura, "Quantifying EV battery end-of-life through analysis of travel needs with vehicle powertrain models," in *Journal of Power Sources*, vol. 282, pp. 265-276. Jan. 2015.

[93] S. Loffe, C.Szegedy, "Batch Normalization: Accelerating Deep Network Training by Reducing Internal Covariate Shift," in *Proceedings of the 32nd International Conference on Machine Learning*, vol. 37, pp. 448-456, Mar. 2015.

[94] "NN-SVG," http://alexlenail.me/NN-SVG/index.html.

[95] "ERCOT, Electric Reliability Council of Texas," [Online]. Available: http://www.ercot.com/.

[96] 'Pyomo, Python Software packages," Available: [Online]. Available: http://www.pyomo.org/ .

"Gurobi Optimization, Linear Programming Solver," [Online]. Available: https://www.gurobi.com/.

[97] C. Zhao and X. Li, "Microgrid Optimal Energy Scheduling Considering Neural Network based Battery Degradation," *IEEE Transactions on Power Systems*, early access, Jan. 2023.

[98] X. Li, A. S. Korad, and P. Balasubramanian, "Sensitivity Factors based Transmission Network Topology Control for Violation Relief," *IET Generation, Transmission & Distribution*, vol. 14, no. 17, pp. 3539-3547, Sep. 2020.

[99] W. Liao, B. Bak-Jensen, J. R. Pillai, Y. Wang and Y. Wang, "A Review of Graph Neural Networks and Their Applications in Power Systems," in *Journal of Modern Power Systems and Clean Energy*, vol. 10, no. 2, pp. 345-360, March 2022.

[100] A. S. Bretas and A. G. Phadke, "Artificial neural networks in power system restoration," in *IEEE Transactions on Power Delivery*, vol. 18, no. 4, pp. 1181-1186, Oct. 2003.

[101] T. Yalcinoz and M. J. Short, "Neural networks approach for solving economic dispatch problem with transmission capacity constraints," in *IEEE Transactions on Power Systems*, vol. 13, no. 2, pp. 307-313, May 1998.

[102] A. A. Shah, K. Ahmed, X. Han and A. Saleem, "A Novel Prediction Error-Based Power Forecasting Scheme for Real PV System Using PVUSA Model: A

Grey Box-Based Neural Network Approach," in *IEEE Access*, vol. 9, pp. 87196-87206, 2021.

[103] T. Pham and X. Li, "Reduced Optimal Power Flow Using Graph Neural Network," *2022 North American Power Symposium (NAPS)*, Salt Lake City, UT, USA, 2022, pp. 1-6.

[104] J. B. Hansen, S. N. Anfinsen and F. M. Bianchi, "Power Flow Balancing With Decentralized Graph Neural Networks," in *IEEE Transactions on Power Systems*, vol. 38, no. 3, pp. 2423-2433, May 2023.

[105] M. Tuo and X. Li, "Convolutional Neural Network-based RoCoF-Constrained Unit Commitment," *arXiv*, Aug. 2023.

[106] J. Gracia, A. J. Mazon and I. Zamora, "Best ANN structures for fault location in single-and double-circuit transmission lines," in *IEEE Transactions on Power Delivery*, vol. 20, no. 4, pp. 2389-2395, Oct. 2005.

[107] V. Sridharan, M. Tuo and X. Li, "Wholesale Electricity Price Forecasting using Integrated Long-term Recurrent Convolutional Network Model," *Energies*, 15(20), 7606, Oct. 2022.

[108] D. Ageng, C. -Y. Huang and R. -G. Cheng, "A Short-Term Household Load Forecasting Framework Using LSTM and Data Preparation," in *IEEE Access*, vol. 9, pp. 167911-167919, 2021.

[109] Y. Yu, J. Cao and J. Zhu, "An LSTM Short-Term Solar Irradiance Forecasting Under Complicated Weather Conditions," in *IEEE Access*, vol. 7, pp. 145651-145666, 2019.

[110] V. Suresh, F. Aksan, P. Janik, T. Sikorski and B. S. Revathi, “Probabilistic LSTM-Autoencoder Based Hour-Ahead Solar Power Forecasting Model for Intra-Day Electricity Market Participation: A Polish Case Study,” in *IEEE Access*, vol. 10, pp. 110628-110638, 2022.

[111] S. Dittmer, E. J. King and P. Maass, “Singular Values for ReLU Layers,” in *IEEE Transactions on Neural Networks and Learning Systems*, vol. 31, no. 9, pp. 3594-3605, Sept. 2020.

[112] G. Wang, G. B. Giannakis and J. Chen, “Learning ReLU Networks on Linearly Separable Data: Algorithm, Optimality, and Generalization,” in *IEEE Transactions on Signal Processing*, vol. 67, no. 9, pp. 2357-2370, 1 May1, 2019.

[113] S. Han and J. Ha, “A Low-complexity Neural BP Decoder with Network Pruning,” *2020 International Conference on Information and Communication Technology Convergence (ICTC)*, Jeju, Korea (South), 2020, pp. 1098-1100.

[114] M. Gong, J. Liu, H. Li, Q. Cai and L. Su, “A Multiobjective Sparse Feature Learning Model for Deep Neural Networks,” in *IEEE Transactions on Neural Networks and Learning Systems*, vol. 26, no. 12, pp. 3263-3277, Dec. 2015.

[115] B. -C. Lai, J. -W. Pan and C. -Y. Lin, “Enhancing Utilization of SIMD-Like Accelerator for Sparse Convolutional Neural Networks,” in *IEEE Transactions on Very Large Scale Integration (VLSI) Systems*, vol. 27, no. 5, pp. 1218-1222, May 2019.

[116] Z. Liu, X. Hu, L. Xu, W. Wang and F. M. Ghannouchi, “Low Computational Complexity Digital Predistortion Based on Convolutional Neural Network for Wideband Power Amplifiers,” in *IEEE Transactions on Circuits and Systems II: Express Briefs*, vol. 69, no. 3, pp. 1702-1706, March 2022.

[117] A. Ashiquzzaman, L. V. Ma, S. Kim, D. Lee, T. -W. Um and J. Kim, “Compacting Deep Neural Networks for Light Weight IoT & SCADA Based Applications with Node Pruning,” *2019 International Conference on Artificial Intelligence in Information and Communication (ICAIIC)*, Okinawa, Japan, 2019, pp. 082-085.

[118] J. Li, X. Rao, S. Xiao, B. Zhao and D. Liu, “Pruner to Predictor: An Efficient Pruning Method for Neural Networks Compression,” *2022 14th International Conference on Advanced Computational Intelligence (ICACI)*, Wuhan, China, 2022, pp. 9-14.

[119] W. Luo, “Improving Neural Network With Uniform Sparse Connectivity,” in *IEEE Access*, vol. 8, pp. 215705-215715, 2020.

[120] K. Wu, Y. Guo and C. Zhang, “Compressing Deep Neural Networks With Sparse Matrix Factorization,” in *IEEE Transactions on Neural Networks and Learning Systems*, vol. 31, no. 10, pp. 3828-3838, Oct. 2020.